

**Determination of fundamental magnetic anisotropy
parameters in rock-forming minerals and their
contributions to the magnetic fabric of rocks**

A dissertation submitted to the
SWISS FEDERAL INSTITUTE OF TECHNOLOGY ZURICH

For the degree of
Doctor of Natural Sciences

Presented by

Fátima Martín Hernández
Lic. Physics, Universidad Complutense de Madrid, Spain
Born June 15th, 1974
Citizen of Spain

Accepted on the recommendation of:

Dr. A.M. Hirt	examiner
Prof. Dr. W. Lowrie	co-examiner
Dr. K. Kunze	co-examiner
Dr. C.M. Lüneburg	co-examiner

Acknowledgments

It is difficult to elaborate a list with all the persons that have contributed to the end of this thesis, and probably I will forget some that undoubtedly have also to be here.

I would like to thank my supervisor Dr. A.M. Hirt, who helped me from the beginning in scientific and not so scientific problems and difficulties found along this period. All my geological knowledge is certainly her merit. She focussed the problems into a point that I would not have been able to find. I would also like to thank her for her infinite patient correcting my manuscripts. Thanks for a fruitful field work in Spain and for using blue pen and pencil.

Prof. Dr. W. Lowrie has improved my work with his experience and comments. Thanks to him I have extended all the mathematical methods into more complete, clear and elegant developments.

Dr. K. Kunze has guided me in the texture goniometry. He was available for questions about technical problems and fundamental principles of new techniques. Thanks for the suggestions that certainly completed the parts concerning to goniometry analysis and his interest on the rest of the thesis, methodology and even fieldwork.

For the fieldwork in Spain I relied on the help of Prof. M. Julivert. All that I have learnt about the area is thank to him. Gracias Manuel.

I would also like to thank Prof. M.L. Osete, who introduced me into this world, gave me an opportunity after my degree and supplied my samples from the Betic Cordillera.

Most of the phyllosilicate single crystals from Switzerland were provided by Dr. P. Brack, Institut fuer Mineralogie und Petrographie, ETH-Zurich.

Then I would like to thank all the people that I have met during this period. In the texture goniometry lab I would like to mention Martin Schmocker and the priceless help of David Martínez for hours of discussion, crystallography and description of thin sections.

Dr. M. Jackson, Dr. Jim Marvin and Peat Solheid for their help and asistence during my visit to the IRM at the University of Minnesota.

And now the list of people of the paleomagnetic lab: Giovanni Muttoni, Maurizio Sartori, Robi Zergeny, Paola Gialanella, Jack Hannam, Maya Haag, thanks Luca

Lanci for a special course "Matlab for dummies". I would like also to mention Francesca Cifelli.

And two students that in their words have "strengthened my character" and with whom I have shared work, office, hopes, good and bad moments....Danke "lieber alemano-Simo Spassov" for lending an ear, discussing, sharing worries....., it has been very funny. Grazie anche al mio "caro pignolone Ramon Egli", non ho parole per ringraziare tutto, un pezzettino da la tesi e' tuo. Thanks both for becoming my friends in the cold Switzerland.

I want to mention people from the Institute of Geophysics, the O9 group: Remco, Mark, Federica..., Francesca Funicello for a nice "meeting" in San Francisco.

My swiss adventure could probably not have been the same without a very special friend. Gracias Ana, por los secretos a la luz de una vela en Martastrasse 99 e anche a Cleofe, "mit" per un giorno.

A mis padres y hermano, que me han ayudado en la distancia y me dieron el empujón hacia las tierras Helveticas.

Y por último, a la persona que ha hecho posible esta tesis, a Senén.

Table of contents

Abstract	iv
Kurzfassung	vi
Symbols and abbreviations	ix
1. Introduction	1
2. Theoretical background	7
2.1 Theoretical introduction.....	9
2.2 Types of magnetic materials	9
2.2.1 Diamagnetism.....	9
2.2.2 Paramagnetism	11
2.2.3 Ferromagnetism.....	13
2.2.4 Ferromagnetic minerals.....	16
2.3 Magnetic anisotropy.....	17
2.3.1 Types of magnetic anisotropy	18
2.3.2 Magnetic anisotropy parameters	24
2.4 Magnetic methodology.....	27
2.4.1 Identification of ferromagnetic phases.....	27
2.4.2 Measurements of magnetic anisotropy.....	30
3. Separation of ferrimagnetic and paramagnetic anisotropies using a high- field torsion magnetometer	35
3.1 Introduction.....	37
3.2 Theory of the magnetic torque	38
3.3 Separation of the ferrimagnetic and paramagnetic components of the magnetic anisotropy.....	39
3.4 Experimental method	42
3.4.1 Error estimation.....	43
3.5 Application to three different rock types from the Betic Cordillera.....	45
3.5.1 Magnetic mineralogy.....	46

3.5.2	Anisotropy of magnetic susceptibility.....	48
3.6	Discussion	55
4.	Magnetic properties of phyllosilicates.....	57
4.1	Introduction	59
4.2	Crystallographic description of phyllosilicates.....	61
4.3	Samples description	64
4.4	Measurement procedure.....	65
4.4.1	Mössbauer spectrometry	66
4.5	Biotite.....	68
4.5.1	Rock magnetic properties of biotite	68
4.5.2	Magnetic anisotropy of biotites.....	74
4.6	Muscovite.....	77
4.6.1	Rock magnetic properties of muscovite.....	77
4.6.2	Magnetic anisotropy of muscovite mica	79
4.7	Chlorites.....	83
4.7.1	Rock magnetic properties of chlorite	83
4.7.2	Magnetic anisotropy of chlorite	84
4.8	Discussion	89
4.9	Conclusions.....	92
5.	Fabric analysis.....	93
5.1	Introduction.....	95
5.2	Methods.....	96
5.2.1	Texture goniometer	96
5.2.2	X-ray diffraction scan.....	99
5.2.3	The Scanning Electron Microscope	100
5.2.4	Texture analysis.....	101
5.3	Results.....	103
5.3.1	Studied area	103
5.3.2	Composition analysis of slates	106

5.3.3	Slaty cleavage.....	113
5.3.4	Stretching lineation	118
5.3.5	Crenulation.....	123
5.3.6	Kink bands.....	125
5.4	Discussion and conclusions	129
6.	Mathematical simulation of the AMS	133
6.1	Introduction.....	135
6.2	Calculation of polycrystal properties	136
6.3	Synthetic tests	138
6.4	Input parameters.....	142
6.5	Simulation applied to slates of the Navia-Alto Sil slate belt	143
6.5.1	Slaty cleavage.....	143
6.5.2	Stretching lineation	145
6.5.3	Crenulation cleavage.....	146
6.5.4	Kink bands.....	147
6.6	Bulk susceptibility.....	149
6.7	Discussion and conclusions	150
7.	Summary and conclusions.....	153
7.1	Separation of the paramagnetic and ferromagnetic components to the anisotropy of magnetic susceptibility	155
7.2	Results of the anisotropy of magnetic susceptibility in biotite, muscovite and chlorite	156
7.3	Analysis of fabric in natural samples.....	158
7.4	Mathematical simulation of the AMS.....	159
7.5	Outlook.....	159
	Appendix	161
	REFERENCES.....	169
	CURRICULUM VITAE.....	183

Abstract

The aim of the project was to acquire more knowledge about the mechanisms that lead to the anisotropy of magnetic anisotropy (AMS) in rocks. Special attention was given to rocks whose susceptibility is carried by paramagnetic minerals. Mathematical simulation of the AMS was carried out in samples rich in phyllosilicates to examine how the anisotropy of individual minerals contribute to the total anisotropy. A good mathematical model of the AMS requires three pieces of information. Firstly reliable values for the magnetic anisotropy of single crystals of the main minerals forming the rock are necessary. Secondly, the distribution of these minerals, i.e., the mineral or textural fabric, must be known. And thirdly, the actual magnetic fabric must be measured.

A method to separate of the components of magnetic anisotropy has been developed, using measurements with a high-field torque magnetometer. The separation is based on the linear dependence of the paramagnetic torque signal on the square of the applied field. The torque signal of ferrimagnetic minerals is constant above their magnetic saturation. This difference in the torque signal of the two mineral types is used to split the anisotropy of magnetic susceptibility of the two types of magnetic materials. Measurements in three perpendicular planes lead to the determination of the deviatoric susceptibility ellipsoid for these three examples. An estimation of the relative sizes of the paramagnetic and ferrimagnetic fractions of anisotropic minerals is also obtained. The method was successfully tested in three types (granites, peridotites and serpentinites) from highly deformed samples from the Betic Cordillera, southern Spain. Granites do not show a significant ferrimagnetic contribution to the AMS; therefore, a very good agreement has been found between low-field and paramagnetic susceptibilities. In peridotites the low-field susceptibility is almost coincident with the principal directions of the ferrimagnetic fraction, although the AMS is carried by both types of magnetic minerals. The ferrimagnetic minerals dominate the low-field magnetic susceptibility of serpentinite. A good agreement is found between the minimum axes of susceptibility, while the maximum and intermediate axes are distribute along the foliation plane, measured in the field.

The anisotropy of magnetic susceptibility of phyllosilicate single crystals, i.e., biotite, muscovite and chlorite, has been determined from high-field torque

magnetometry. The combination of the paramagnetic deviatoric susceptibility with paramagnetic bulk susceptibility, obtained from hysteresis measurements, permits a complete evaluation of the AMS ellipsoid. With this method the anisotropy values of the crystals themselves can be defined. The anisotropy due to ferrimagnetic inclusions was also evaluated in order to understand the effects that they may cause on the low-field susceptibility measurements.

Mössbauer spectra were made on the biotite samples to determine Fe(II)/Fe(III) of the crystals. A good correlation is found between the iron ratio and degree of anisotropy which has important implications on the correlation of AMS with finite strain.

The mineral fabric, determined with X-ray texture goniometry, and the magnetic fabric of natural samples were the second object of interest in this project. Ordovician slates from the Luarca formation in northwestern Spain were chosen, because their anisotropy is due largely to phyllosilicate minerals in the rock. A good agreement has been found between the minimum direction of magnetic susceptibility and the maximum direction of the mineral fabric ellipsoid in most of the samples.

Measurements were done on samples displaying slaty cleavage, crenulation cleavage and kinks with different wavelengths. Differences between the mineral fabric and magnetic ellipsoids arise from differences in the dimensions evaluated by the two techniques. The texture goniometer examines an area with a radius of some millimeters, whereas the measured AMS averages grain anisotropies over the size of a cylindrical sample with 2.54 cm diameter and 2.2 cm length. Geological interpretation of the results supports the idea that the Asturian Arc could not be formed by oroclinal bending.

If caution is taken in considering the differences in the scale of measurements, a mathematical model of the AMS, based on the mineral fabrics of the individual phases contributing to the magnetic susceptibility, can be successfully made. The synthetic ellipsoid of the AMS shows a good agreement in shape, degree of anisotropy and orientation with the actual measurements.

Kurzfassung

Das Ziel der vorliegenden Arbeit war es, mehr Wissen über den Mechanismus, der zur Anisotropie der magnetischen Suszeptibilität (AMS) in Gesteinen führt, zu erwerben. Das Augenmerk lag bei Gesteinen, deren Suszeptibilität durch paramagnetische Minerale getragen wird. Die mathematische Simulation der AMS wurde an Proben durchgeführt die reich an Schichtsilikaten sind, um zu untersuchen, wie die einzelnen Minerale zur Gesamtsuszeptibilität beitragen. Ein gutes mathematisches Modell erfordert drei Informationen. Erstens sind verlässliche Werte der magnetischen Anisotropie der Einkristalle der gesteinsbildenden Mineralien notwendig. Zweitens muss die räumliche Verteilung dieser Mineralien, d.h. texturale Gefüge, bekannt sein. Drittens muss das magnetische Gefüge gemessen werden.

Es wurde eine Methode entwickelt, die Komponenten der magnetischen Anisotropie unter Benutzung von Messungen einer Hochfeld-Drehmomentwaage zu separieren. Die Separation beruht auf der linearen Abhängigkeit des paramagnetischen Drehmomentes vom Quadrat des angelegten Magnetfeldes. Dagegen ist das Drehmoment ferrimagnetischer Mineralien oberhalb deren Sättigungsmagnetisierung konstant. Der Unterschied der Drehmomentsignale beider Mineralarten wurde benutzt, um die Anisotropie der Suszeptibilität beider magnetischer Materialien aufzuspalten. Messungen in drei senkrecht zu einander stehenden Ebenen führen zur Bestimmung des deviatorischen Suszeptibilitätstensors für diese zwei Mineralklassen. Eine Bestimmung des relativen Verhältnisses von paramagnetischen zu ferrimagnetischen anisotropen Mineralien erfolgte ebenfalls. Die Methode wurde erfolgreich getestet an drei Gesteinsarten (Granit, Peridotit und Serpentin), die einen hohen Deformationsgrad aufwiesen. Die Gesteine stammen aus der Betic Cordillera in Südspanien. In den Graniten ist der ferrimagnetische Beitrag zur AMS nicht besonders hoch, weshalb gute Übereinstimmung zwischen Niedrigfeld- und paramagnetischer Suszeptibilität herrscht. In den Peridotiten stimmt die Niedrigfeld-Suszeptibilität mit der Hauptrichtung der ferrimagnetischen Fraktion überein, obwohl die AMS von beiden (paramagnetischen und ferrimagnetischen) Mineralien getragen wird. Ferrimagnetische Mineralien dominieren die Niedrigfeld-Suszeptibilität der Serpentine. Gute Übereinstimmung herrscht auch zwischen den Minimumsachsen der Suszeptibilität, im Gegensatz dazu sind die Hauptachse mit

maximale und intermediärer Suszeptibilität über die im Feld gemessene Schieferungsebene verteilt.

Die Anisotropie der magnetischen Suszeptibilität der Schichtsilikat-Einkristalle (Biotit, Muskowit und Chlorit) wurde durch Messungen mit einer Hochfeld-Drehmomentwaage bestimmt. Die Kombination des paramagnetischen deviatorischen Suszeptibilitätstensors und der paramagnetischen Gesamtsuszeptibilität (aus Hysterese-messungen) erlaubt eine vollständige Berechnung des AMS-Ellipsoids. Mit dieser Methode konnten die Anisotropiewerte der Kristalle selbst definiert werden. Die Anisotropie ferrimagnetischer Kristalleinschlüsse wurde ebenfalls berechnet, um deren eventuelle Einflüsse auf Niedrigfeld-Suszeptibilitätsmessungen verstehen zu können.

Mössbauer-Spektroskopie wurde an Biotit-Proben durchgeführt, um das Fe(II)/Fe(III)-Verhältnis dieser Kristalle zu bestimmen. Es ergab sich eine gute Korrelation zwischen dem Eisenverhältnis und dem Grad der Anisotropie, was bedeutende Auswirkungen auf die Korrelation zwischen AMS und finiter Verformung hat.

Das Mineralgefüge, bestimmt durch Röntgen-Textur-Goniometrie, und das magnetische Gefüge natürlicher Proben war ein zweiter Schwerpunkt der vorliegenden Promotionsarbeit. Ordovizische Schiefer der Luarca-Formation im Nordwesten Spaniens wurden wegen ihrer grösstenteils von Schichtsilikaten verursachten Anisotropie dafür ausgewählt. Bei den meisten Proben konnte eine gute Übereinstimmung zwischen der Minimumsrichtung der magnetischen Suszeptibilität und der Maximumsrichtung des Mineralgefügeellipsoids beobachtet werden.

Die Messungen wurden an Proben durchgeführt, die Schieferungen, Mikrofältelungen und Knichfalten unterschiedlicher Wellenlänge aufwiesen. Die Unterschiede zwischen Mineralgefüge und magnetischem Ellipsoid beruhen auf den bei beiden Techniken benutzten unterschiedlichen Bezugsdimensionen. Bei der Röntgen-Textur-Goniometrie wird eine Fläche mit einem Radius von wenigen Millimetern analysiert, wohingegen sich die AMS in zylindrischen Proben von 2.2 cm Länge und 2.54 cm Durchmesser gemessen werden. Die geologische Interpretation der Ergebnisse unterstützt die Hypothese, dass der Asturische Bogen nicht durch "oroclinal bending" entstehen konnte.

Unter Berücksichtigung der Skalenunterschiede beider Messtechniken wissend, kann ein mathematisches Modell der AMS, basierend auf Mineralgefügen der

einzelnen zur Suszeptibilität beitragenden Phasen, erstellt werden. Das synthetische Ellipsoid der AMS weist eine gute Übereinstimmung in Form, Grad der Anisotropie sowie Orientierung mit den tatsächlichen Messungen auf.

Symbols and abbreviations

κ	Magnetic susceptibility
μ_0	Magnetic permeability of free space ($= 4\pi \times 10^{-7} \text{ N A}^{-2}$)
AARM	Anisotropy of the Anhyseretic R emanent M agnetization
AF	Alternating Field
AMS	Anisotropy of M agnetic S usceptibility
ARM	Anhyseretic R emanent M agnetization
B	Magnetic induction [T]
BSE	B ack S catter E lectrons
EDS	E nergy D ispersive X -ray S pectroscopy
H	Magnetic field [Am^{-1}]
H_c	Coercivity field [Am^{-1}]
HF	H igh- F ield
IRM	Isothermal R emanent M agnetization
k_B	Boltzman constant ($= 1.384 \times 10^{-7} \text{ J K}^{-1}$)
LF	L ow- f ield property
LPO	L attice P referred O rientation
m	Magnetic moment [Am^2]
M	Magnetization [Am^{-1}]
M_s	Saturation magnetization [Am^{-1}]
ODF	O rientation D istribution F unction
$P(\theta, \varphi)$	Probability density of a direction or pole on the sphere (pole figure)

P_j	Ellipsoid anisotropy degree parameter
SE	Secondary Electrons
SEM	Scanning Electron Microscope
S_1	Cleavage plane
S_2	Crenulation plane
SIRM	Saturated Isothermal Remanent Magnetization
T	Ellipsoid shape parameter
T	Magnetic torque [J]
t	Magnetic torque per unit volume [Jm^{-3}]
TH	Thermal treatment
VSM	Vibration Sample Magnetometer

1. Introduction



*An illustration showing how hot iron, when beaten, can be made magnetic, from Gilbert's book *De Magnete*, (1600).*

Seite Leer /
Blank leaf

Since the publication of Graham's (1954) seminal work, the analysis of the anisotropy of magnetic susceptibility has been demonstrated to be useful in application to problems in many areas of geophysics and geology. The earliest works were focused on the correlation between the main structural features of the rocks and magnetic anisotropy parameters in sediments (Rees, 1961), sedimentary rocks (Graham, 1966) or igneous rocks (Stacey, 1960). The deflection of the remanence in deformed rocks was also examined (Hargraves and Fischer, 1959; Fuller, 1960). Mathematical theories to explain the origin of the AMS and reviews of the measuring and analysis procedure were given by Stacey (1963), Uyeda et al. (1963) and Bhathal (1971).

The magnetic anisotropy is caused by two factors: firstly, the anisotropy of the single crystals that form the sample (Sato et al., 1964; Porath and Raleigh, 1967; Hrouda, 1986; Borradaile et al., 1987; Ozdemir and Dunlop, 1999) and secondly their anisotropic preferred orientation (Housen and van der Pluijm, 1990; Stephenson, 1994).

Early studies assumed ferrimagnetic phases were largely responsible for the observed magnetic anisotropy, due to their higher susceptibilities with respect to the susceptibility of the matrix, usually paramagnetic or diamagnetic (Hargraves and Fischer, 1959; Fuller, 1960; Rees, 1961). However it has been found that in many cases the magnetic anisotropy is carried by the paramagnetic minerals (Hounslow, 1985; Borradaile et al., 1985/86; Lüneburg et al., 1999; Hirt et al., 2000). Therefore there is an increased interest in the mechanisms that cause magnetic anisotropy, based on paramagnetic phases.

The aim of this thesis is to establish a mathematical model, which simulates the measurement of AMS in samples where the anisotropy of magnetic susceptibility has been proven to be carried only by paramagnetic minerals. The area selected for this purpose was the Ordovician slate belt in northern Spain, the Lluçanès Slate Belt. A previous study in the area demonstrated the paramagnetic origin of the magnetic anisotropy in these slates (Hirt et al., 2000). Along the belt it is possible to select sites with different deformational states, with perfectly developed slaty cleavage, kink bands and crenulation cleavage overprinting the slaty cleavage (Julivert and Soldevila, 1998). These different deformation structures are useful in understanding the mechanism that governs the acquisition of magnetic anisotropy in these rocks over a broad range of deformational stages.

In order to model the AMS in these slates, it is first necessary to know the magnetic anisotropy of single crystals and their preferred orientation in the samples. These values are then used to model AMS, using the mathematical models proposed by Owens (1974).

Two types of phyllosilicates, mica and chlorite, were the main paramagnetic phases in the analyzed samples. Available information on the magnetic anisotropy of these rock-forming minerals is not well constrained. Some values in the literature were evaluated with low-field methods, which do not exclude that ferromagnetic inclusions may be contributing to the AMS of the crystal (Borradaile et al., 1987; Zapletal, 1990). Borradaile and Werner (1994) used a high-field method to separate the ferromagnetic from the paramagnetic anisotropy to avoid this problem. Their data were not always consistent with the values expected from the crystallographic structure of phyllosilicates. For example, the c-axis was found to be sub-parallel to the basal plane in some samples.

Chapter 2 presents an introduction about the different types of magnetic materials and their characteristics. A brief summary about the main physical laws that govern the behavior of these minerals is shown. The chapter describes the instruments used for the analysis of magnetic properties used as well as the experiments performed.

High-field methods have been used in this study to measure the paramagnetic susceptibility of single crystals by means of high-field torque magnetometry. A mathematical method has been developed in order to separate the contribution of magnetic anisotropy of paramagnetic from ferromagnetic fabrics in the torque signal. This is the content of Chapter 3 (Martín-Hernández and Hirt, 2001). The method has been successfully tested in three highly deformed rock-types from the Betic Cordillera, Southern Spain.

The anisotropy parameters of biotite, muscovite and chlorite have been reevaluated and results are presented in Chapter 4. The anisotropies of samples from the three minerals are well constrained and consistent with the structure of the phyllosilicates.

Chapter 5 examines the mineral and magnetic fabrics in the Luarca Slate Belt. Texture goniometry has been used to determine the preferred orientation of phyllosilicates. Several studies have shown good correlation between preferred orientation of phyllosilicates and the principal directions of magnetic anisotropy (Siegesmund et al., 1995; Lüneburg et al., 1999; Siegesmund and Becker, 2000;

Ullemeyer et al., 2000). A detailed analysis of texture and magnetic fabric has been made in order to show how magnetic anisotropy develops in slates.

The proposed simulation of the AMS has been tested in samples that show different deformation structures. The model expands on the previous models presented by Hrouda and Schulmann (1990) and Siegesmund et al. (1995). In Chapter 6 the model is used to provide information on both the principal directions of the AMS and the shape and degree of anisotropy of the ellipsoid.

On the basis of the different structures analyzed, it has been possible to establish a limit for the minimum wavelength of the kinks that can be modeled. The range of possible degree of anisotropy and shape of the magnetic ellipsoid, which can be described by this model, is also proposed in Chapter 6.

The last chapter presents a summary and discussion of the results in their entirety and an outlook for further investigations.

Seite Leer,
Blank leaf

2. Theoretical background

The analysis of the anisotropy of magnetic susceptibility has been used as a petrofabric indicator since the early 1950s. It was related with tectonic deformation and many models have been developed which correlate the anisotropy of magnetic susceptibility with deformation, strain, paleocurrents, flow directions, etc. But a correct interpretation of the results requires a good understanding of the causes that give rise to an anisotropic configuration of the magnetic parameters in the rocks. The following chapter provides a summary of the physical origin of magnetism in rocks, classification of the magnetic materials and the different types of anisotropy in rocks.

Seite Leer /
Blank leaf

2.1 Theoretical introduction

The following section provides a short summary of the theory that governs the magnetization of rocks and the origin of magnetic anisotropy. A more complete discussion of the physical theory of rock magnetism is given in Nagata (1961), Chikazumi (1964), O'Reilly (1984) and Dunlop and Özdemir (1997).

Magnetism arises from the movement of charged particles. In natural materials the magnetism stems from: 1) motion of electrons in their orbitals around the nucleus and 2) the intrinsic electron spin. A brief summary of the theory that governs the magnetic properties of materials can be found in Jiles (1991).

When a magnetic field (\mathbf{H}) is applied to a material the electrons motion is modified, resulting in an induced magnetization (\mathbf{M}). The relationship between \mathbf{M} and \mathbf{H} is:

$$\mathbf{M} = \kappa \mathbf{H} \quad (2.1)$$

where κ is the tensor of *magnetic susceptibility*.

2.2 Types of magnetic materials

The criterion that is used to differentiate magnetic materials is how they respond to an external magnetic field. Materials can be divided into three major groups: diamagnetic, paramagnetic and ferromagnetic.

2.2.1 Diamagnetism

In diamagnetic materials all electrons are paired so that the magnetic moments associated with the electronic spins are compensated and a net magnetic moment only arises from the orbital moment. When an external magnetic field is applied to a diamagnetic material, the angular momentum vector associated with the orbit precesses around the direction of the applied field with an angular velocity proportional to the applied field that is predicted by Larmor. The magnetic moment associated with the precession is induced in a direction opposite to the applied field.

2.2.2 Paramagnetism

Paramagnetism exists in materials with atoms having unpaired electron spins. The magnetic moment per atom has a non-zero value and a resultant moment arises in the material when a magnetic field is applied. This net magnetization is in the field direction and persists until the applied field is removed (Figure 2.2).

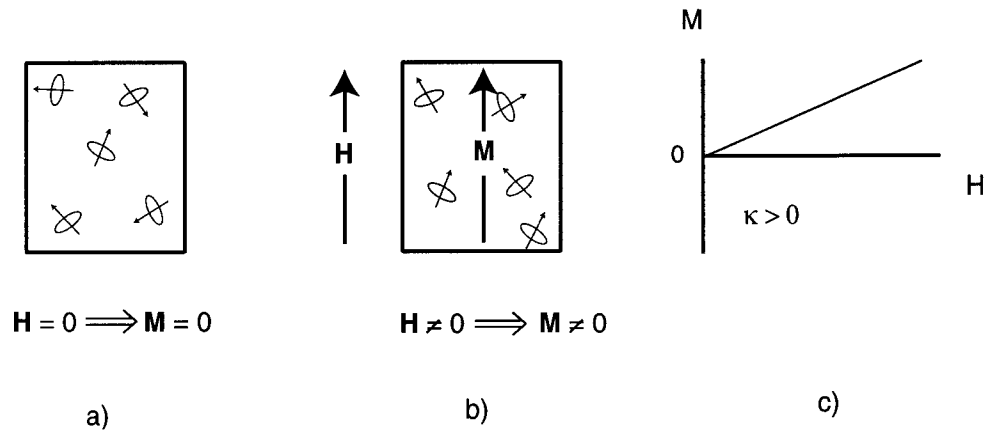


Figure 2.2: Behavior of paramagnetic material a) in the absence of a magnetic field and b) when a magnetic field is applied; c) the variation of magnetization as a function of the applied field strength. Modified from Lowrie (1997).

The magnetization of paramagnetic materials is dependent on alignment energy and thermal energy, which is described by the Langevin theory. In the presence of a magnetic field (\mathbf{H}), the magnetic moments of the atoms in a material have the alignment energy:

$$E_m = -\mu_0 \mathbf{m} \cdot \mathbf{H} = -\mu_0 m H \cos \theta \quad (2.3)$$

where \mathbf{m} is the atomic magnetic moment and θ is the angle between the atomic moment and the applied field.

The probability of \mathbf{m} being aligned is perturbed by the thermal energy of the moments. The Boltzmann probability of the moments being aligned in one direction is:

$$P(\theta) = \exp\left(\frac{\mu_0 m H \cos \theta}{k_B T}\right) \quad (2.4)$$

where k_B is the Boltzmann constant and T is the temperature. The net magnetization is the result of the integration over the entire angular range of θ .

$$M(H, T) = N m L(\alpha) = N m \left(\coth \alpha - \frac{1}{\alpha} \right) \quad (2.5)$$

where $L(\alpha)$ is the Langevin function for $\alpha = \frac{\mu_0 m H}{k_B T}$ and N the number of magnetic moments per unit volume.

In a first approximation, when the magnetic energy ($\mu_0 m H$) is small compared to the thermal energy ($k_B T$), the Langevin function can be approximated as $L(\alpha) \approx \alpha/3$. The magnetization simplifies to:

$$M = \frac{1}{3} \frac{N m^2 H \mu_0}{k_B T} \quad (2.6)$$

The paramagnetic susceptibility can be expressed as:

$$\kappa_{para} = M/H \quad (2.7)$$

$$\kappa_{para} = \frac{1}{3} \frac{N m^2 \mu_0}{k_B T} = \frac{C}{T} \quad (2.8)$$

which is the most common definition of the Curie law. The paramagnetic susceptibility is inversely proportional to the absolute temperature. The proportionality constant or Curie constant (C) is characteristic of the material.

Paramagnetic materials have a temperature where the thermal energy exceeds the alignment energy, the paramagnetic Curie temperature θ . Below this temperature the initial approximation of the Langevin function is not valid. The paramagnetic susceptibility follows the Curie-Weiss law for $T > \theta$.

$$\kappa_{para} = \frac{C'}{T - \theta} \quad (2.9)$$

where C' is the paramagnetic Curie constant.

Many clay minerals, olivine, amphibole and pyroxene have paramagnetic susceptibilities at room temperature. In general, paramagnetic susceptibilities are 10-100 times higher than diamagnetic susceptibilities and therefore the paramagnetic signal generally masks the diamagnetic susceptibility.

2.2.3 Ferromagnetism

Ferromagnetic materials have uncompensated spins similar to paramagnetic materials. Adjacent atomic moments interact, which produces a magnetization without applying an external field. If the distance between neighbor atoms is small enough, the atomic orbitals overlap. In the simplest case of two electrons, the energy of the system is not the sum of energy of the individual electrons but also contains a term, the *exchange energy* of quantum mechanical nature. This term is a result of the interaction between magnetic moments and is minimized by alignment of atomic moments. A spontaneous magnetization in the absence of an external magnetic field.

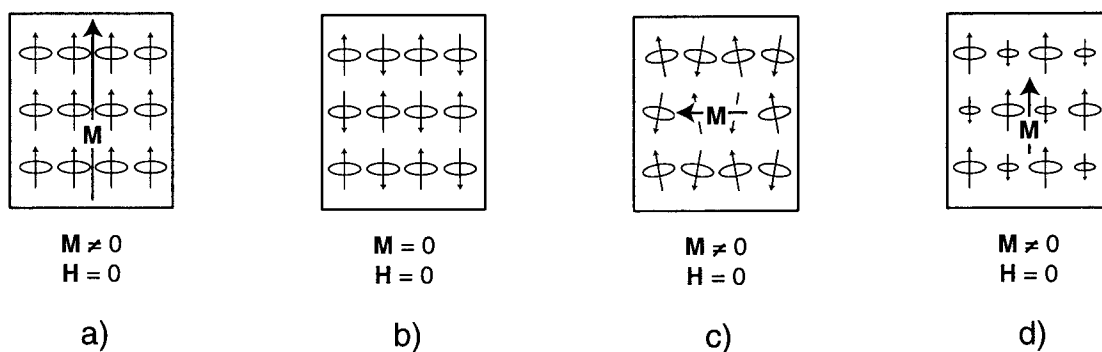


Figure 2.3: Schematic depiction of the net magnetization in ferromagnetic materials. a) ferromagnetism, b) antiferromagnetism, c) parasitic ferromagnetism or spin-canted antiferromagnetism and d) ferrimagnetism. Modified from Lowrie (1997).

Only metals have a true quantum exchange behavior. In the case of oxide components, the oxygen ions provide a link between nearest-neighbor cations, which are otherwise too far apart for a direct exchange. As a result of the overlap of the

cation of transition metals and the oxygen ion, the resultant spin vectors of the cations are coupled, sometimes parallel to each other and other times antiparallel. Ferromagnetic minerals can be divided in four different types depending on how the interaction occurs (Figure 2.3).

2.2.3.1 Ferromagnetism

Ferromagnetism (s.s.) is a magnetic property of some metals. The metal cations display an exchange interaction which results in a spontaneous magnetization in the absence of an external magnetic field (Figure 2.3a). All magnetic moments are aligned parallel and in the same direction. The most important metals, which have a ferromagnetic behavior, are iron, nickel, manganese and cobalt. In the presence of an external applied field, the relationship between the field and the acquired magnetization is not linear, but shows hysteresis (section 2.2.3.5).

2.2.3.2 Antiferromagnetism

In antiferromagnets the exchange interaction occurs between sublattices within a crystal. In either sublattice the magnitude of magnetization is constant and opposite in direction to the adjacent sublattice (Figure 2.3b). This configuration yields a zero net magnetization. The temperature at which the exchange is destroyed and the material reverts to paramagnetic behavior is the *Néel temperature* (T_N) and is analogous to the Curie temperature for ferromagnets. Ilmenite and some forms of pyrrhotite exhibit antiferromagnetism, whereas pyrrhotite, hematite and goethite are minerals with imperfect antiferromagnetic behavior. When an external magnetic field is applied, this type of material has an induced magnetization. The relationship between the applied field and induced magnetization is linear and positive. The behavior is similar to paramagnetic minerals although the magnetic susceptibility of antiferromagnets is slightly smaller.

2.2.3.3 *Parasitic ferromagnetism*

Parasitic ferromagnetism is the result of either imperfections in the lattice of an antiferromagnetic crystal or of canting of the atomic moments. The presence of impurities or vacancies in the lattice leads to an uncompensated magnetization in the direction perpendicular to the lattice average direction of atomic moments (Figure 2.3c). This type of mineral shows magnetic hysteresis as well as a characteristic Néel temperature. Goethite, hematite and some forms of pyrrhotite are common minerals that should be antiferromagnetic but which show parasitic ferromagnetism and retain a net magnetization with no applied field.

2.2.3.4 *Ferrimagnetism*

In ferrimagnetic materials, the magnetization of each sublattice has different intensities with antiparallel directions (Figure 2.3d). There is a remanent magnetization in the absence of an external magnetic field below the *Curie temperature*. The magnetic interaction disappears above the Curie temperature and the material behaves as a paramagnet. Ferrites display magnetic hysteresis (section 2.2.3.5). The most important ferrimagnetic mineral is magnetite.

2.2.3.5 *Magnetic hysteresis*

Magnetic hysteresis is the loop described by the magnetization as a function of the applied field in ferromagnetic, ferrimagnetic and parasitic ferromagnetic materials (Figure 2.4).

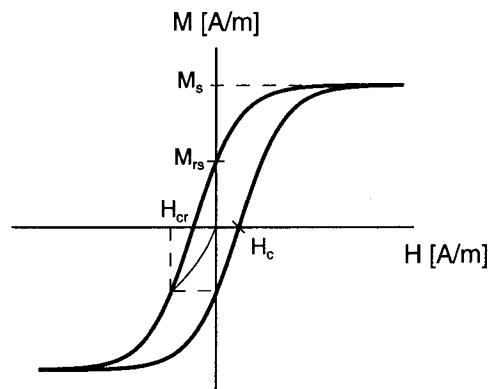


Figure 2.4: Idealized hysteresis loop of a ferromagnetic material showing the most important parameters that define the loop.

The field is applied to the material in one direction until the magnetization saturates (M_s). Then the field is subsequently reduced to zero, where the magnetization is not zero but retains a remanent magnetization (M_{rs}). The field is then applied progressively in the opposite direction until the saturation is reached. The field that is required to induce a magnetization equal and opposite to M_{rs} so that the total magnetization is zero, is the coercive force or coercivity (H_c). The remanent coercivity (H_{cr}) is the reverse field required to remove any net remanent magnetization. The shape and parameters of the hysteresis loop are dependent on the type of ferromagnetic grains and the average grain size and shape.

2.2.4 Ferromagnetic minerals

The main property that characterizes ferromagnetic minerals is its remanent magnetization. The remanent magnetization (M_r) is a balance between the magnetic alignment energy and thermal activation. The effect of time on the magnetization has been described by Néel (1949) as:

$$M_r = M_o e^{-\frac{t}{\tau}} \quad (2.10)$$

where M_o is the initial remanent magnetization, t the time and τ the characteristic relaxation time. The relaxation time is given by:

$$\tau = \tau_0 e^{\left(\frac{\mu_0 V M_s H_c}{2k_B T}\right)} \quad (2.11)$$

where τ_0 is a constant with a value of $\sim 10^{-9}$ s (Néel, 1949), V is the volume of the magnetic grain, and H_c is the coercive force.

The blocking temperature (T_b) of a grain is the temperature below which it can retain its magnetization over geologic time. Similarly, a grain is said to have a blocking volume (V_c) or critical size (d_c). This is the minimum dimension of the grain required to retain a magnetization over long time scales. Superparamagnetism refers to ferromagnetic grains that are beyond the temperature or volume threshold and have a relaxation time < 100 s (Bean and Livingston, 1959). The magnetization of the entire

grain remains coherent, spin alignment being dictated by the internal molecular field, but the entire magnetic moment is free to rotate in an external applied field and the material behaves like a paramagnetic mineral.

The most common ferromagnetic minerals are the iron oxides magnetite, maghemite and hematite; the iron hydroxide goethite and the iron sulphides pyrrhotite and greigite. A summary of the magnetic properties of these minerals can be found in Lowrie (1990) or Dunlop and Özdemir (1997), and in the table below.

Table 2.1: Characteristic magnetic properties of the most common rock-forming ferromagnetic minerals. References: (1) Banerjee and Moskowitz (1985), (2) Özdemir and Banerjee (1984), (3) Dunlop (1971), (4) Dekkers (1988a) and (5) Dekkers (1988b).

ferromagnetic phase	chemical composition	Curie/Néel temperature (°C)	maximum coercivity (T)	reference number
magnetite	Fe ₃ O ₄	578	0.3	(1)
maghemite	γ-Fe ₂ O ₃	~ 645	0.3	(2)
hematite	α-Fe ₂ O ₃	675	1.5-5	(3)
goethite	α-FeOOH	80-120	>5	(4)
pyrrhotite	FeS _{1+x} (0 < x < 0.14)	320	0.5-1	(5)

2.3 Magnetic anisotropy

Magnetic anisotropy is the directional variability of a specific magnetic property, e.g. magnetic susceptibility, anhysteretic remanence magnetization or saturation of remanent magnetization (e.g., Tarling and Hrouda (1993) and Borradaile and Henry (1997)). The susceptibility can be described mathematically as a symmetric second rank tensor, and be can represented physically as an ellipsoid with three principal axes. For the anisotropy of the magnetic susceptibility the eigenvalues corresponding the principal axes are given as $\kappa_3 \leq \kappa_2 \leq \kappa_1$.

In a given direction i , the relationship between magnetization and applied field is not a scalar but a second-rank tensor. The magnetization can be written as:

$$\begin{pmatrix} M_x \\ M_y \\ M_z \end{pmatrix} = \begin{pmatrix} \kappa_{11} & \kappa_{12} & \kappa_{13} \\ \kappa_{21} & \kappa_{22} & \kappa_{23} \\ \kappa_{31} & \kappa_{32} & \kappa_{33} \end{pmatrix} \begin{pmatrix} H_x \\ H_y \\ H_z \end{pmatrix} \quad (2.12)$$

This matrix is symmetric and can be also expressed in the following tensorial notation:

$$M_i = \kappa_{ij} H_j \quad (i, j = 1, 2, 3) \quad (2.13)$$

The anisotropy of remanent magnetization can be similarly defined. Reviews of magnetic anisotropy can be found in Hrouda (1982), Borradaile (1988), Lowrie (1989), Rochette et al. (1992) and Tarling and Hrouda (1993).

2.3.1 Types of magnetic anisotropy

Magnetic anisotropy has historically been analyzed by means of the anisotropy of susceptibility and the anisotropy of an artificial remanent magnetization. Both types are due to a non-isotropic distribution of mineral grains.

Six mechanisms have been proposed to explain magnetic anisotropy in rocks, whereby shape anisotropy and crystalline anisotropy are the most important ones. Excellent discussions about the mechanisms can be found in Bhathal (1971), Hrouda (1982) and Tarling and Hrouda (1993).

2.3.1.1 Shape anisotropy

When a ferromagnetic grain is placed in an external magnetic field its effective magnetization is reduced due to a demagnetization field (H^{dem}). The applied field causes surface magnetic charges, which produce an internal field in the opposite direction of the external field (Figure 2.5). If a field is applied along the i -axis ($i = x, y, z$), the effective field (H^{eff}) is:

$$H^{eff} = H^{ext} - H^{dem} \quad (2.14)$$

2. Theoretical background

The demagnetization field is proportional to the grain magnetization, the constant of proportionality being the *demagnetization factor* (N_i). Therefore the effective field can be written as:

$$H^{eff} = H^{ext} - N_x M = H^{ext} - N_x \kappa H^{eff} \quad (2.15)$$

where N_x is the demagnetization factor along the x-axis and M is the magnetization of the grain. The relationship between the effective field and the external field considering isotropic susceptibility is:

$$H^{eff} = \frac{1}{1 + N_x \kappa} H^{ext} \quad (2.16)$$

Consider a single grain of ellipsoidal shape with H^{ext} applied along the x-axis. The magnetization is:

$$M_x = \kappa H_x^{eff} = \kappa \frac{1}{1 + N_x \kappa} H^{ext} \quad (2.17)$$

In non-equidimensional grains there is a directional dependence of the demagnetization factor, which is known as *shape anisotropy*.

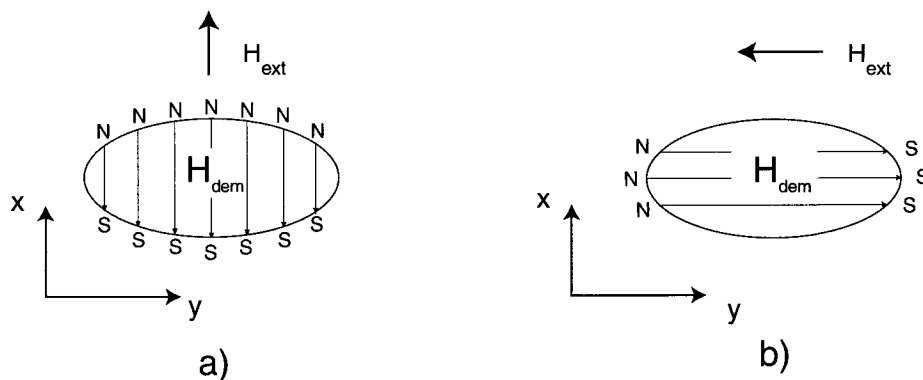


Figure 2.5: Shape anisotropy of ellipsoidal magnetic grains.

In the example presented in Figure 2.5, the H^{dem} is higher when H^{ext} is applied parallel to the x-axis as compared to the y-axis, because $N_x > N_y$, therefore $M_x < M_y$.

Differences in the magnetization in two perpendicular directions are related to differences in the demagnetization factor:

$$M_x - M_y = \kappa H_x^{eff} - \kappa H_y^{eff} = \kappa H^{ext} \left(\frac{1}{1 + \kappa N_x} - \frac{1}{1 + \kappa N_y} \right) \quad (2.18)$$

Since H^{ext} is constant, the differences can be viewed as differences in the proportionality factor between magnetization and field, that is between the susceptibility:

$$\kappa_{xx} - \kappa_{yy} = \kappa \left(\frac{1}{1 + \kappa N_x} - \frac{1}{1 + \kappa N_y} \right) \quad (2.19)$$

Analogously, it is possible to define differences between the other cartesian directions x, y and z.

In a more realistic grain, not only the demagnetization factor, but also the magnetic susceptibility are tensors. Therefore Eq. (2.15) is rewritten as:

$$H_i^{eff} = H_i^{ext} - N_{ij} \kappa_{jl} H_l^{eff} \quad (2.20)$$

Magnetite is an example of a mineral strongly affected by shape anisotropy when grains are not equidimensional.

2.3.1.2 Anisotropy of domain alignment

When a magnetic grain grows in size, the magnetic energy and the magnetic charges also grow. At a critical size, magnetic domains are formed in order to decrease the magnetostatic energy. Each magnetic domain is a region of the grain where the magnetization has a constant direction (b). The region in which the magnetization changes its orientation from one domain to another is called a *domain wall* or *Bloch Wall* (c).

Magnetic susceptibility values depend on the direction of the applied field with respect to the domains of the magnetic grain. When an external field is applied

parallel to the domain walls the obtained susceptibility (κ_{\parallel}) is a measure of the ease with which the 180° walls may move. The susceptibility perpendicular to the domain walls (κ_{\perp}) is due to the rotation of the spontaneous magnetization against the forces of magnetocrystalline anisotropy.

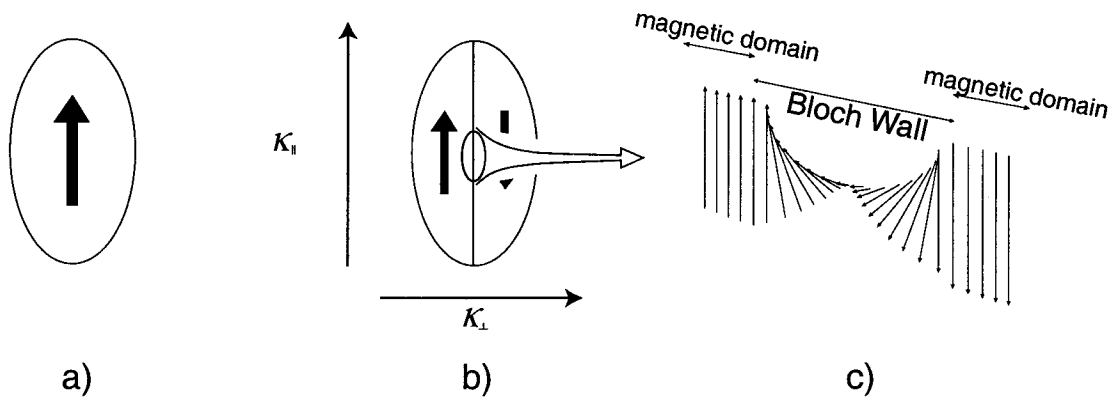


Figure 2.6: Formation of two-domain grain decreases the magnetostatic energy. a) single-domain grain, b) grain with two domains, in which the magnetic susceptibility has a different value parallel (κ_{\parallel}) or perpendicular (κ_{\perp}) to the domain wall and c) simplified model of a domain wall. Modified from O'Reilly (1984).

2.3.1.3 Crystalline anisotropy

In crystals, cations are located in a lattice structure, which affects the exchange process (section 2.2.3). The direction of magnetization is affected by this exchange. A *magnetocrystalline anisotropy* is produced.

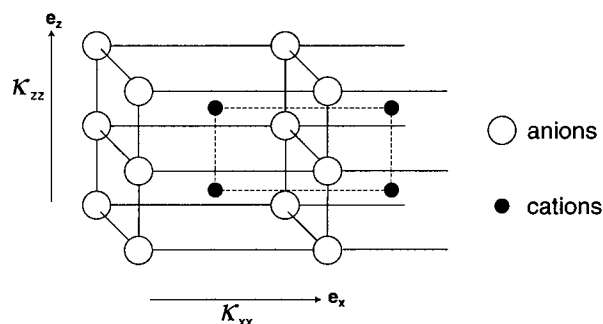


Figure 2.7: Simplified scheme of a crystal with crystalline anisotropy. Arrows show two perpendicular directions in which the magnetic susceptibility has different values.

The spatial configuration of the iron cations and the oxygen anions in the crystal is responsible for crystalline anisotropy in common ferromagnetic minerals. The superexchange phenomenon (section 2.2.3) is more effective in a certain direction than in others and therefore the magnetization prefers to lie along specific crystallographic directions. This behavior gives rise to an easy magnetization axis and a hard axis of magnetization within the crystal. Hematite is a ferromagnetic mineral that shows a strong crystalline magnetic anisotropy. The magnetization lies only in the basal plane at room temperature and therefore the mineral has a magnetic susceptibility 100 times larger parallel than normal to the basal plane.

The magnetic anisotropy of paramagnetic minerals is due to crystalline anisotropy. The spatial distribution of the cations in the lattice causes interactions that give rise to spatial dependence of the magnetic susceptibility when an external magnetic field is applied. Many rock-forming minerals show this type of magnetic anisotropy, e.g. micas, chlorites, hornblende, siderite or tourmaline. These minerals can also contribute to the magnetic anisotropy of the rocks since they are important components of a rock's matrix.

This type of anisotropy will be the main focus of this thesis.

2.3.1.4 Textural anisotropy

This is the term given to the magnetic anisotropy that results from the stringing together of magnetic grains in lines or planes. The stronger susceptibility lies parallel to the string of grains.

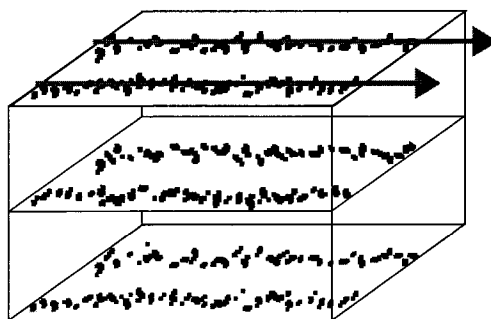


Figure 2.8: Schematic diagram illustrating textural anisotropy. The arrow shows the direction of maximum magnetic susceptibility.

In natural rocks the distribution of grains is generally related with structures in the samples, e.g., fractures or cracks, natural veins, minerals cleavage or ooid (e.g, Kligfield et al. (1982)).

2.3.1.5 Exchange anisotropy

This term was originally used to describe a magnetic interaction between an antiferromagnetic material and a ferromagnetic material and has been later extended to include the interaction between ferromagnetic and ferrimagnetic materials (Meiklejohn, 1962). The simplest model assumes a single domain of antiferromagnetic material and a ferromagnetic material with an interface plane separating them (Figure 2.9).

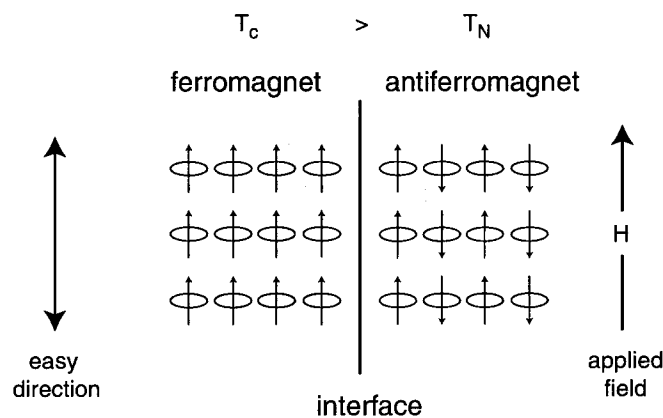


Figure 2.9: Simple model of exchange anisotropy. T_c is the Curie temperature of the ferromagnetic phase and T_N is the Néel temperature of the antiferromagnetic phase. Modified from Bhathal (1971).

When a large magnetic field is applied along the easy direction of magnetization with $T_N < T < T_C$, the ferromagnetic moments orient parallel to the applied field. If the specimen is then cooled through the Néel temperature T_N of the antiferromagnet, the spins of the lattice closest to the ferromagnet will align in the same direction as the ferromagnet. Subsequent spin planes will orient antiparallel to each other. These alternating antiparallel planes are highly anisotropic and hold the magnetization of the ferromagnetic material in the direction of the applied field.

Exchange anisotropy has been found in titanomagnetite (Banerjee and O'Reilly, 1965) or the intergrowth maghemite with hematite (Banerjee, 1966). Exchange

anisotropy has been invoked to explain self-reversals in the direction of magnetization of natural rocks (Nagata and Uyeda, 1959). There has been an increase of interest in the last decade about this magnetic phenomenon because of its application in magnetic thin layers (Sano et al., 1998).

2.3.1.6 Stress induced anisotropy

The change in the magnetization as the result of the application of stress is known as *magnetostriction*. Since the magnetization depends on the distances between different magnetic particles (section 2.2.3), a change in the distances may cause a change in the magnetization. This type of anisotropy is of interest, since it may lead to a possible deflection of the magnetization of rocks as a result of a tectonic stress.

2.3.2 Magnetic anisotropy parameters

Mathematically, the anisotropy of magnetic susceptibility is described as a symmetric second rank tensor. The terms in the diagonal, when the tensor is expressed in its principal coordinate system are termed principal values or *eigenvalues*. They define an ellipsoid, the *magnetic susceptibility ellipsoid*, and their orientations are the principal directions or *eigenvectors*. The geometric representation of the susceptibility is this ellipsoid that can be described in terms of its shape and anisotropy degree. The shape of the ellipsoid is described qualitatively as *oblate*, or disk shaped (Figure 2.10a), and *prolate*, or cigar shaped (Figure 2.10b).

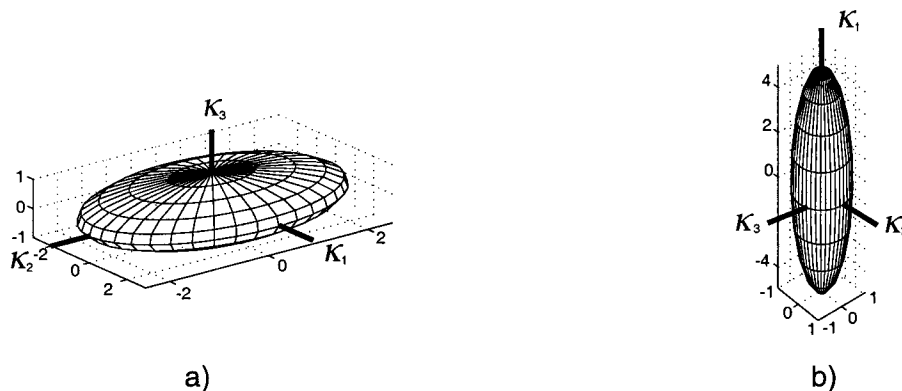


Figure 2.10: Shape of the magnetic anisotropy susceptibility; a) oblate and b) prolate.

The standard normalization criteria implies that the trace of the susceptibility tensor is equal of 3:

$$\kappa^{total} = \kappa_{bulk} \cdot \begin{bmatrix} \bar{\kappa}_1 & 0 & 0 \\ 0 & \bar{\kappa}_2 & 0 \\ 0 & 0 & \bar{\kappa}_3 \end{bmatrix} \quad \text{with } \bar{\kappa}_1 + \bar{\kappa}_2 + \bar{\kappa}_3 = 3 \quad (2.21)$$

Different parameters have been proposed to quantify the shape and degree of anisotropy of the magnetic susceptibility ellipsoid. These can be represented graphically in the plots described below.

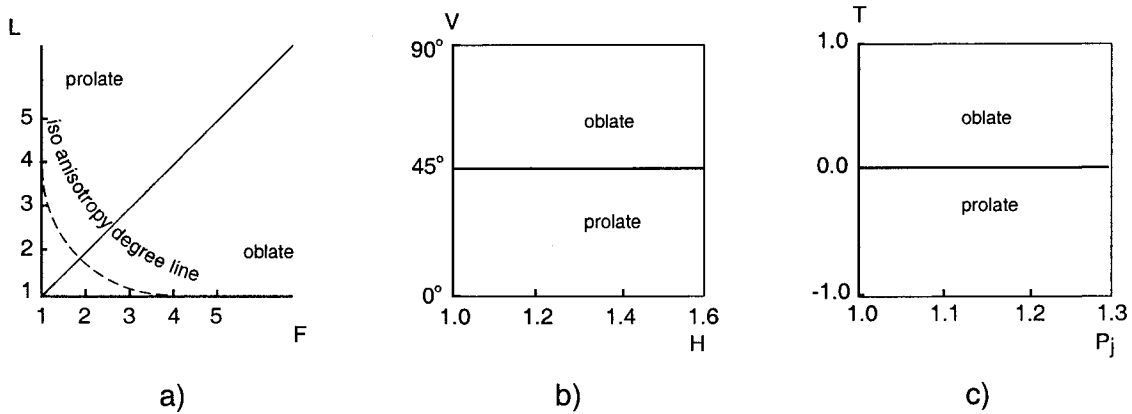


Figure 2.11: Three representations of the shape of the magnetic susceptibility ellipsoid and degree of anisotropy. a) Magnetic Flinn diagram, b) Graham plot and c) Jelinek plot.

- *Flinn diagram*

This diagram uses magnetic lineation and foliation, similar to the Flinn diagram that represents the strain ellipsoid in structural geology. Neutral ellipsoids lie on the diagonal of the graph, which also differentiates the shape of the ellipsoid (Figure 2.11a). The magnetic lineation (L), magnetic foliation (F) and anisotropy degree (P) are defined as:

$$\begin{aligned}
 L &= \frac{\kappa_1}{\kappa_2} && \text{magnetic lineation } (1 \leq L \leq \infty) \\
 F &= \frac{\kappa_2}{\kappa_3} && \text{magnetic foliation } (1 \leq F \leq \infty) \\
 P &= \frac{\kappa_1}{\kappa_3} && \text{anisotropy degree } (1 \leq P \leq \infty)
 \end{aligned}
 \tag{2.22}$$

- *Graham plot*

This graphical representation uses the shape parameter (V) defined by Graham (1966). The shape parameter gives the angle between the two circular cross-sections. The fabric is oblate when $V > 45^\circ$ and prolate when $V < 45^\circ$.

$$\begin{aligned}
 V &= \arcsin \sqrt{\frac{\kappa_2 - \kappa_3}{\kappa_1 - \kappa_3}} && \text{Graham's shape parameter } (0^\circ \leq V \leq 90^\circ) \\
 H &= \frac{\kappa_1 - \kappa_3}{\kappa_{mean}} && \text{Total anisotropy } (0 \leq H \leq 3)
 \end{aligned}
 \tag{2.23}$$

where κ_{mean} is the arithmetic mean of the three principal susceptibility values.

- *Jelinek plot*

This representation combines lineation and foliation parameters to provide a single shape parameter to quantify both properties (Jelinek, 1981). Neutral ellipsoids are defined by a shape parameter $T = 0$. It is the most commonly used representation of the magnetic anisotropy in the literature. The shape parameter is defined as:

$$T = \frac{2\eta_2 - \eta_1 - \eta_3}{\eta_1 - \eta_3} \quad (-1 \leq T \leq 1) \tag{2.24}$$

where $\eta_1 = \ln \kappa_1$; $\eta_2 = \ln \kappa_2$; $\eta_3 = \ln \kappa_3$; $\eta_{mean} = (\eta_1 + \eta_2 + \eta_3) / 3$

Jelinek defined also the *corrected anisotropy degree* (P_j) as:

$$P_j = e^{\sqrt{2[(\eta_1 - \eta_{mean})^2 + (\eta_2 - \eta_{mean})^2 + (\eta_3 - \eta_{mean})^2]}} \quad (1 \leq P_j \leq \infty) \tag{2.25}$$

The Jelinek plot shows T plotted against P_j (Figure 2.11c).

2.4 Magnetic methodology

2.4.1 Identification of ferromagnetic phases

It is useful to identify the ferromagnetic phases present in the samples so that one can understand the origin of the magnetic anisotropy in a rock or mineral. Microscopic methods are often not useful in identifying ferromagnetic minerals due to the fine grain sizes of the minerals most responsible for the magnetic behavior. Different techniques have been developed therefore (Butler, 1992).

2.4.1.1 Alternating field demagnetization (AF)

In alternating field demagnetization the magnetic moments of an assemblage of grains are remagnetized so that a sample's net magnetization is removed. This can be accomplished by randomizing the magnetization in a specified coercivity range, either by tumbling the sample during AF demagnetization or by canceling the magnetization with an antipodal magnetization along three mutually perpendicular directions in the sample. The specimen is placed in a zero ambient field and subjected to an alternating magnetic field. All grains with a coercivity spectrum smaller than the maximum peak field will be randomized and the corresponding part of the magnetization of the sample will be cancelled. By repeating the process in ever-increasing fields, the remanent magnetization can be progressively demagnetized. The method is limited to magnetic grains with coercivities lower than the maximum peak field that can be produced. Therefore the method is not practical when high coercivity minerals, e.g., hematite or goethite, are present in a sample.

2.4.1.2 Anhysteretic remanent magnetization (ARM)

Anhysteretic remanent magnetization (ARM) is acquired by a sample when it is subjected to an alternating field (AC) in the presence of a small direct current magnetic field (DC). The magnetic grains with coercivity up to maximum amplitude

of the alternating magnetic field will be magnetized in the bias DC field. Depending on the alternating field used, when the DC field is applied, specific grain sized fractions can be magnetized (Jackson et al., 1988). The remanence intensity depends on the DC and AC fields.

2.4.1.3 Acquisition of Isothermal Remanent Magnetization (IRM)

A remanent magnetization acquired in a DC field at constant temperature conditions is called *Isothermal Remanent Magnetization (IRM)*. The intensity of the magnetization increases with the strength of the applied field until a maximum magnetization is reached, the saturation isothermal magnetization (SIRM). The shape of the acquisition curve and intensity of the IRM are dependent on the concentration and type of magnetic mineral in a material. The maximum coercivities of the common ferromagnetic (s.l.) minerals are well known and can be identified (c.f., Dunlop and Özdemir (1997)).

Thermal demagnetization of IRM allows both thermal and coercivity properties of minerals to be explored (Lowrie, 1990). Three different fields can be applied along the three axes of a sample. Thermal demagnetization of the multicomponent IRM allows for the discrimination of which coercivity component is being unblocked in a specific temperature range.

2.4.1.4 Thermal demagnetization of the magnetization (TD)

In thermal demagnetization, a sample is heated step-wise in zero-field. Those magnetic grains with a blocking temperature below the reached temperature lose their magnetization. Upon cooling in zero-field the grains that have been demagnetized do not acquire magnetization. The heating and cooling cycles are repeated increasing the temperature each cycle. The Curie temperature of ferromagnetic minerals is well known and the temperature at which the magnetization of the magnetic phase is lost is indicative of the ferromagnetic minerals in the rock. Problems can arise from chemical changes in the samples during heating, which can lead to creation of new ferromagnetic minerals or transformation of existing ones. Thermal demagnetization

in this work was done with a Schonsted thermal demagnetizer with a maximum rest field of 5nT.

2.4.1.5 Magnetic hysteresis measurements

Hysteresis measurements provide complete information about the magnetization in the sample (section 2.2.3.5). In ferromagnetic samples with an important paramagnetic component, hysteresis measurements provide information on the paramagnetic characteristics of the samples. The slope of the curve above the saturation of the ferromagnetic phases is the paramagnetic susceptibility (Figure 2.12).

Magnetic hysteresis measurements have been performed with a vibrating sample magnetometer (Micromag VSM) manufactured by Princeton Measurements Corporation with a maximum field of 1T. Some samples were measured on a similar instrument at the Institute for Rock Magnetism, University of Minnesota, that had a maximum field of 1.8T and also a cryostat in which measurements could be made between 5K and 300K. Saturation of the ferromagnetic phases was typically found above 70% of the maximum applied field. This range was used to evaluate the paramagnetic susceptibility.

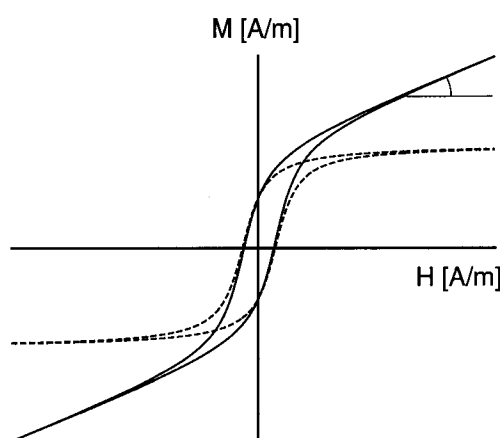


Figure 2.12: Idealized hysteresis loop of a sample formed by a mixture of ferromagnetic and paramagnetic minerals. The solid curve shows the direct measurement, the dotted curve shows the hysteresis loop of the ferromagnetic fraction after removing the paramagnetic component.

2.4.2 *Measurements of magnetic anisotropy*

2.4.2.1 *Low-field Anisotropy of Magnetic Susceptibility (AMS)*

Low-field susceptibility was measured with an AGICO KLY-2 Kappabridge susceptibility meter, in which the strength of the applied field is 300 A/m (Tarling and Hrouda, 1993). The susceptibility bridge has a sensitivity of 4×10^{-8} [S.I.]. Fifteen independent measurement positions are used to define the 6 independent components of the susceptibility tensor (Jelinek, 1978).

With the same equipment it is possible to measure the anisotropy of low-field magnetic susceptibility at 77 K, using the method outlined by Lüneburg et al. (1999). The paramagnetic susceptibility, which follows the Curie-Weiss law (Eq. (2.9)), will increase at low temperatures. This method allows an approximate estimation of the paramagnetic contribution to the magnetic anisotropy of samples.

2.4.2.2 *High-field Anisotropy of Magnetic Susceptibility (HFA)*

One method to analyze high-field magnetic susceptibility is with a high-field torque magnetometer. Applying magnetic fields high enough to saturate the ferrimagnetic contribution allows the mathematical separation between paramagnetic/antiferromagnetic/diamagnetic and ferrimagnetic components of the magnetic susceptibility. The physical model relates the magnetic torque that an anisotropic sample experiences in an applied field with the magnetic susceptibility tensor (Collinson et al., 1967; Bhathal, 1971; Owens and Bamford, 1976; Jelinek, 1981; Tarling and Hrouda, 1993). The general expression for the torque that a specimen experiences in the presence of a magnetic field is different depending on the type of magnetic minerals it contains.

For paramagnetic minerals the torque depends on the square of the applied field and the differences of paramagnetic susceptibility. For a magnetic induction B applied in the plane containing axes x_1 and x_2 , the torque given by:

$$\begin{aligned}
 T_1 &= \frac{1}{2\mu_o} V B^2 [\kappa_{23}(1 - \cos 2\theta) + \kappa_{13} \sin 2\theta] \\
 T_2 &= -\frac{1}{2\mu_o} V B^2 [\kappa_{13}(1 + \cos 2\theta) + \kappa_{23} \sin 2\theta] \\
 T_3 &= -\frac{1}{2\mu_o} V B^2 [(\kappa_{22} - \kappa_{11}) \sin 2\theta + 2\kappa_{12} \cos 2\theta]
 \end{aligned} \tag{2.26}$$

where V is the volume of the sample, B the modulus of the applied field, κ_{ij} ($i, j=1, 2, 3$) are the components of the paramagnetic susceptibility tensor, θ is the angle of orientation of the applied field (Figure 2.13) and μ_o the magnetic permeability of vacuum.

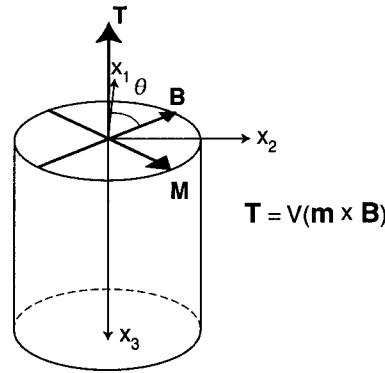


Figure 2.13: Simplified scheme of the torque (t) experienced by an anisotropic sample in the presence of an applied magnetic induction B . The torque is perpendicular to the plane which contains the applied field and the magnetization direction (M).

For a ferromagnetic sample, whose magnetization is saturated, the torque is field independent and is related to the difference between the appropriate component of the ferromagnetic demagnetization factors:

$$\begin{aligned}
 T_1 &= \frac{1}{2} \mu_o V_E M_s^2 [N_{23}(1 - \cos 2\theta) + N_{13} \sin 2\theta] \\
 T_2 &= -\frac{1}{2} \mu_o V_E M_s^2 [N_{13}(1 + \cos 2\theta) + N_{23} \sin 2\theta] \\
 T_3 &= -\frac{1}{2} \mu_o V_E M_s^2 [(N_{22} - N_{11}) \sin 2\theta + 2N_{12} \cos 2\theta]
 \end{aligned} \tag{2.27}$$

where here M_s is the magnetization of saturation and N_{ij} are components of the demagnetization tensor.

Samples are measured by stepwise rotating the specimen 360° in three perpendicular planes. The magnetic torque experienced by the sample is recorded as a function of orientation angle θ . The measured torque can be fitted by a trigonometric function in which each of its terms has a different physical meaning related to the magnetic anisotropy of the sample. The offset or zero term of the fitted series is the term independent of angle. This term corresponds to the work done due to irreversible magnetization processes when the sample is rotated 360° in a magnetic field (Day et al., 1970). The method has been shown to be a non-destructive technique for identification of ferromagnetic phases (Day et al., 1970; Cowan and O'Reilly, 1972; Nishio et al., 1997; Bottoni et al., 1999; Sagnotti and Winkler, 1999). The first term of the series ($\sin\theta$) is related to inhomogeneous distributions of the material or exchange anisotropy (Collinson et al., 1967; Bhathal, 1971). In low-field torque curves this term is related to the remanence of the sample. The $\sin 2\theta$ term arises from the paramagnetic susceptibility anisotropy (Eq. (2.26)), shape anisotropy (Eq. (2.27)) or stress anisotropy (Stacey, 1963). Crystalline alignment of cubic minerals gives rise to a dominant $\sin 4\theta$ term in the torque curve (Stacey, 1960). The presence of this term also indicates texture anisotropy (Banerjee and Stacey, 1967).

The analysis of the amplitude of the torque signal reveals the presence of anisotropy of domain alignment. The torque curves have different amplitude as well as different initial phase depending on the reference direction in the sample with respect to the direction of the magnetic domains (Bhathal and Stacey, 1969).

Different instruments have been described in the literature based on different principles of operation. One type of instrument is based on a modified galvanometer, which reacts to the torque of a suspended sample with a compensation system (Banerjee and Stacey, 1967). Further modifications of this type of instrument allow for measuring at different temperatures (Fletcher et al., 1969). Improvement of the electronics that control the voltage to compensate for the torque has been made (Owens and Bamford, 1976; Ellwood, 1978; Parma, 1988). The magnetometer used in this work is an automated high-field torque magnetometer with a compensation system and a range of applied fields between 0.45 and 1.85 T (Bergmüller et al.,

1994). This high range enables the saturation of many of the ferrimagnetic minerals present in natural samples.

The magnetometer has two essential parts in its design, the torque head and the suspension of the sample holder. The torque head of the magnetometer consists of two blocks (Figure 2.14), in which one is fixed and connected to a mobile block with a pair of hinges. Movement of this second block is due to the torque experienced by the sample in the presence of a magnetic field.

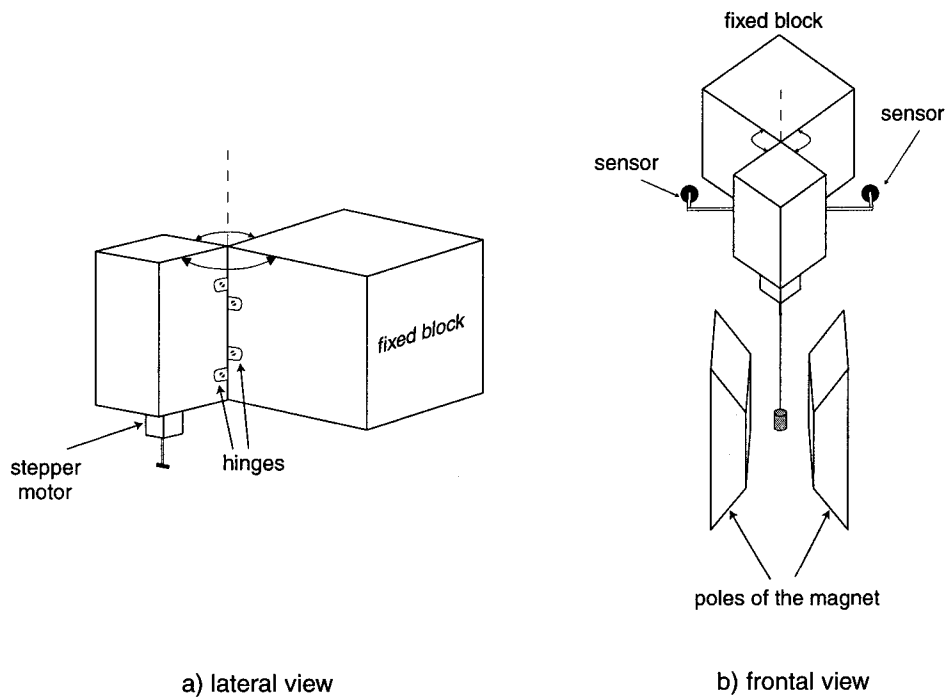


Figure 2.14: Schematic drawing of the head of the torque magnetometer. a) Lateral view of the two main blocks forming the head and the hinges that connect them. b) Frontal view in which the position of the sensors and the position of the sample between the magnet poles is shown.

The removable part of the holder where the sample is located is a quartz glass construction in which the specimen is located. The head is a specially designed non-magnetic metal piece that is connected with the fixed part by a hook (Figure 2.15). This hook allows the sample to move in two perpendicular directions in the horizontal plane. Thus only the torque in the z-direction related to the sample anisotropy is transmitted by the electronic sensor and compensated by a counter-force controller with an applied voltage.

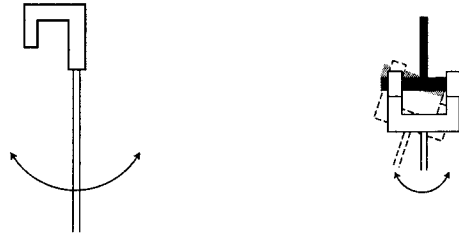


Figure 2.15: Sample holder of the torque magnetometer. The special design allows the sample holder to move in two perpendicular horizontal directions.

2.4.2.3 Anisotropy of the Anhysteretic Remanent Magnetization (AARM)

McCabe et al. (1985) suggested a method for defining the anisotropy of ARM, using 9 different positions to define the anhysteretic susceptibility tensor. In this study a maximum static field of 100 mT was used with a 0.1 mT bias DC field. Samples were demagnetized before applying the first ARM. The resulting remanence was measured on a three-axis, 2G cryogenic magnetometer. The magnetization was then removed by AF demagnetization. The two consecutive processes are repeated for the remaining 8 positions and the remanence is fitted with an ellipsoid. As only ferromagnetic minerals carry a magnetization, the ellipsoid calculated with this method is due to the ferromagnetic contribution in the coercivity range < 100 mT to the anisotropy.

3. Separation of ferrimagnetic and paramagnetic anisotropies using a high-field torsion magnetometer

The analysis of magnetic fabric in magnetic fields that are strong enough to saturate ferrimagnetic phases permits the separation of paramagnetic and ferrimagnetic fabrics. Anisotropy measurements in two different fields are necessary to separate the components, but are insufficient to define them precisely. A method of analysis using several high fields has been developed and applied to three different lithologies from the Betic Cordillera in Southern Spain, in which the anisotropies are controlled by different mineral fractions. The magnetic anisotropy of granites was found to be dominated by paramagnetic minerals. Peridotites possessed a mixed magnetic fabric in which the measured anisotropy is due to both magnetic fractions. The magnetic anisotropy of serpentinites was dominated by the ferrimagnetic minerals.

Seite Leer /
Blank leaf

3.1 Introduction

Anisotropy of magnetic susceptibility (AMS) is determined from the directional variability of the induced magnetization (M_i) in an applied field (B_j), where $M_i = \kappa_{ij} B_j$ ($i, j = 1, 2, 3$). The susceptibility (κ_{ij}) of a rock can be described by a symmetric second-order tensor. It is represented geometrically by an ellipsoid, whose principal axes are $\kappa_1 \geq \kappa_2 \geq \kappa_3$. Numerous studies have shown that the AMS can be related to mineral and tectonic fabrics (e.g., Tarling and Hrouda, (1993); Borradaile and Henry, (1997)).

In commercial susceptibility bridges, the AMS is generally measured in weak applied fields (10-500 μT), and all minerals contribute to the measured low field susceptibility (κ_{LF}). In order to separate the ferrimagnetic contribution to the AMS, it is necessary to measure the high field susceptibility (κ_{HF}) above the saturation magnetization of the ferrimagnetic fraction. This requires fields above 300 mT for magnetite and maghemite, 600 mT for pyrrhotite and fields greater than 1.5 T for hematite. Henry and Daly (1983) proposed a mathematical reduction method that assumes that ferrimagnetic and paramagnetic fabrics are distinct under the same strain conditions. McCabe et al. (1985) discriminated between the two possible magnetic fabrics by comparing the AMS with the susceptibility of anhysteretic remanence due to the ferrimagnetic fraction. Rochette and Fillion (1988) used a cryogenic magnetometer to determine the susceptibility anisotropy of both ferrimagnetic and paramagnetic fractions in rocks by exploiting the field and temperature dependencies of the two magnetization types. Based on hysteresis loops, Borradaile and Werner (1994) employed an alternating gradient magnetometer to isolate the paramagnetic susceptibility of ferrimagnetic contaminants in oriented phyllosilicate minerals. Richter and van der Pluijm (1994) used measurements at room temperature and low temperature to decompose the full susceptibility tensor.

Another way to separate ferrimagnetic from paramagnetic components of the AMS is to use a high-field torque magnetometer (Banerjee and Stacey, 1967; Owens and Bamford, 1976; Ellwood, 1978; Parma, 1988; Lowrie, 1989; Bergmüller et al., 1994). Hrouda and Jelinek (1990) presented a mathematical method for separating the components by measuring in two fields above the saturation magnetization of the ferrimagnetic fraction. In this paper we present a new mathematical method, which utilizes measurements in several high fields, for separating the ferrimagnetic and

paramagnetic components of the magnetic fabric. The effectiveness of the separation method was tested on three different lithologies from the Betic Cordillera in Southern Spain, in which the magnetic anisotropy is controlled by different mineral fractions.

3.2 Theory of the magnetic torque

The magnetic torque (T) that acts on a sample when a magnetic field is applied is:

$$T = -\frac{dE}{d\theta} \quad (3.1)$$

where E is the energy of magnetization and θ is the angle between the direction of magnetization and the applied field (B). The torque is dependent on the magnetic properties of the minerals present in the sample. For example, the torque is proportional to B^2 for paramagnetic and diamagnetic minerals; it is constant above the saturating field of a ferrimagnetic mineral. When a paramagnetic specimen is rotated in the x_1 - x_2 plane the magnetic torque is perpendicular to the plane, in the x_3 direction:

$$T_3 = \frac{1}{2\mu_0} V B^2 [(\kappa_{22} - \kappa_{11}) \sin 2\theta + 2\kappa_{12} \cos 2\theta] \quad (3.2)$$

where V is the volume of the sample and μ_0 is the magnetic permeability of vacuum. The torque per unit volume can be written:

$$t_3 = \frac{T_3}{V} = \frac{B^2}{2\mu_0} (b_3^{para} \sin 2\theta + a_3^{para} \cos 2\theta) \quad (3.3)$$

where

$$b_3^{para} = (\kappa_{22} - \kappa_{11}) \quad \text{and} \quad a_3^{para} = 2\kappa_{12} \quad (3.4)$$

When ferrimagnetic minerals whose magnetic moments are saturated in the applied field carry the magnetic anisotropy, differences in the demagnetization energy control the torque, which is given by:

$$T_3 = \frac{1}{2} \mu_0 V_E M_S^2 [(N_{22} - N_{11}) \sin 2\theta + 2N_{12} \cos 2\theta] \quad (3.5)$$

where M_S is the saturation magnetization of the ferrimagnetic mineral, V_E is the total volume of saturated ferrimagnetic grains and N_{ij} are the components of the demagnetization tensor. If the anisotropy is controlled by the ferrimagnetic fraction alone, the torque per unit volume can again be written in the form:

$$t_3 = \frac{T_3}{V_E} = \frac{1}{2\mu_0} (b_3^{ferro} \sin 2\theta + a_3^{ferro} \cos 2\theta) \quad (3.6)$$

where

$$b_3^{ferro} = \mu_0^2 M_S^2 (N_{22} - N_{11}) \quad \text{and} \quad a_3^{ferro} = 2\mu_0^2 M_S^2 N_{12} \quad (3.7)$$

3.3 Separation of the ferrimagnetic and paramagnetic components of the magnetic anisotropy

For natural rock samples, torque is determined by a combination of diamagnetic, paramagnetic and/or ferrimagnetic effects. Consider a sample with a paramagnetic matrix in which there are ferrimagnetic inclusions. The torque is the sum of both contributions:

$$t_i^{total} = t_i^{ferro} + t_i^{para} = \frac{1}{2\mu_0} b_i^{total} \sin 2\theta + \frac{1}{2\mu_0} a_i^{total} \cos 2\theta \quad (3.8)$$

The a and b coefficients each contain paramagnetic and ferrimagnetic contributions. The ferrimagnetic contribution is field independent above the saturation

field, whereas the paramagnetic contribution depends on B^2 . For example, the coefficient, a_i^{total} , is composed of:

$$a_i^{total} = a_i^{ferro} + a_i^{para} = m_i^{ferro} + n_i^{para} \cdot B^2 \quad (3.9)$$

The coefficients of the total torque (Eq. (3.8)) are linearly related to B^2 . For the determination of the slope (n) and intercept (m) of the straight line used in Eq. (3.9) a standard least squares fitting subroutine was used (Squires, 1991). The slope n is the paramagnetic coefficient and the intersect m is the ferrimagnetic coefficient.

When the torque is measured in three mutually perpendicular planes in a dextral orthogonal coordinate system, it is possible to calculate the paramagnetic susceptibility tensor from the paramagnetic coefficients and the demagnetization tensor from the ferrimagnetic coefficients. The paramagnetic coefficients from the torque measurements in the three planes are as follows:

$$\begin{aligned} a_1^{para} &= 2\kappa_{23}; & b_1^{para} &= (\kappa_{22} - \kappa_{33}) \\ a_2^{para} &= 2\kappa_{13}; & b_2^{para} &= (\kappa_{33} - \kappa_{11}) \\ a_3^{para} &= 2\kappa_{12}; & b_3^{para} &= (\kappa_{11} - \kappa_{22}) \end{aligned} \quad (3.10)$$

The non-diagonal terms for the paramagnetic tensor are given by:

$$\kappa_{jk} = \frac{1}{2} a_i^{para} \quad ; i, j, k \in [1, 2, 3] \text{ with } j \neq k \neq i \quad (3.11)$$

The relationship between the diagonal terms of the susceptibility tensor and the paramagnetic coefficients of the torque signal is given by the following expression:

$$\begin{bmatrix} b_1^{para} \\ b_2^{para} \\ b_3^{para} \end{bmatrix} = \begin{bmatrix} 0 & -1 & 1 \\ 1 & 0 & -1 \\ -1 & 1 & 0 \end{bmatrix} \begin{bmatrix} \kappa_{11} \\ \kappa_{22} \\ \kappa_{33} \end{bmatrix} \quad (3.12)$$

This system of equations has a solution with the boundary condition $b_1^{para} + b_2^{para} + b_3^{para} = 0$. The complete susceptibility tensor cannot be evaluated, and only the deviatoric part is calculated. The diagonal components of the deviatoric tensor can be expressed in terms of the paramagnetic coefficients as:

$$\begin{aligned} \kappa_{11}^{dev} &= \frac{1}{3}(b_2^{para} - b_3^{para}) \\ \kappa_{22}^{dev} &= \frac{1}{3}(b_3^{para} - b_1^{para}) \\ \kappa_{33}^{dev} &= \frac{1}{3}(b_1^{para} - b_2^{para}) \end{aligned} \quad (3.13)$$

The ferrimagnetic coefficients from the torque measurements are:

$$\begin{aligned} a_1^{ferro} &= 2\mu_0^2 M_S^2 N_{23}; & b_1^{ferro} &= \mu_0^2 M_S^2 (N_{22} - N_{33}) \\ a_2^{ferro} &= 2\mu_0^2 M_S^2 N_{13}; & b_2^{ferro} &= \mu_0^2 M_S^2 (N_{33} - N_{11}) \\ a_3^{ferro} &= 2\mu_0^2 M_S^2 N_{12}; & b_3^{ferro} &= \mu_0^2 M_S^2 (N_{11} - N_{22}) \end{aligned} \quad (3.14)$$

The non-diagonal and diagonal terms of the ferrimagnetic demagnetization tensor can be solved in the same way as above:

$$\begin{aligned} \mu_0^2 M_S^2 N_{12} &= \frac{1}{2} a_3^{ferro} & \mu_0^2 M_S^2 N_{11}^{dev} &= \frac{1}{3}(b_2^{ferro} - b_3^{ferro}) \\ \mu_0^2 M_S^2 N_{13} &= \frac{1}{2} a_2^{ferro} & \mu_0^2 M_S^2 N_{22}^{dev} &= \frac{1}{3}(b_3^{ferro} - b_1^{ferro}) \\ \mu_0^2 M_S^2 N_{23} &= \frac{1}{2} a_1^{ferro} & \mu_0^2 M_S^2 N_{33}^{dev} &= \frac{1}{3}(b_1^{ferro} - b_2^{ferro}) \end{aligned} \quad (3.15)$$

In order to calculate the ferrimagnetic contribution, the theory assumes that, once the ferrimagnetic magnetization is saturated, the torque does not increase with a further increase in field. If this condition is not met, the separation is not valid, because the behavior of the 2θ coefficient is not linear with B^2 . In this case the paramagnetic contribution will be overestimated.

3.4 Experimental method

Samples 2.54 cm in diameter were drilled in the field with a portable gasoline drill, and subsequently cut into specimens 2.2 cm in length. The paleomagnetic results have been published by Osete et al. (1998). Low-field susceptibility was measured with an AGICO KLY-2 Kappabridge susceptibility meter, in which the strength of the alternating field is 300 A/m. Fifteen independent measurement positions are used to define the susceptibility tensor (Jelinek, 1978). The susceptibility bridge has a sensitivity of 4×10^{-8} [S.I.]. The anisotropy of low-field magnetic susceptibility was also measured at 77 K, using the method outlined in Lüneburg et al. (1999).

Samples were subsequently measured with a high field torque magnetometer (Bergmüller et al., 1994). Each sample was measured during a full rotation about each of three orthogonal axes at angular increments of 20° . Four measurement fields between 1200 and 1800 mT were used, which are strong enough to saturate the magnetization of magnetite, maghemite and pyrrhotite. The sample holder is made out of quartz glass and has a weak diamagnetic anisotropy. The holder was measured three times and an average holder signal was calculated and subtracted from each measurement.

The torque is represented as a function of angle with respect to the coordinate system by Eq. (3.3). The data are fitted with a trigonometric series:

$$t_i(\theta) = \sum_{n=0}^6 A_i^n \cos n\theta + \sum_{n=0}^6 B_i^n \sin n\theta \quad (3.16)$$

Instead of a full Fourier analysis a Fast Fourier Transform (FFT) was used to calculate the coefficients of this series up to the sixth order. The 2θ term was used to evaluate the coefficients of the paramagnetic and ferrimagnetic tensor. It is also possible to determine the proportion of anisotropy due to the ferrimagnetic and paramagnetic fractions. Analogous to the standard deviatoric energy density (Jelinek, 1985; Jelinek, 1988), the relative proportions of the ferrimagnetic (*FSD*) and paramagnetic (*PSD*) anisotropy fractions can be calculated using Eqs. (3.11), (3.13) and (3.15), where the final result is expressed as percentages. With the obtained paramagnetic deviatoric ellipsoid (p_{ij}) and ferrimagnetic deviatoric ellipsoid (f_{ij}) the fractions are defined by:

$$FSD = \sqrt{\frac{\sum_{i=1}^3 f_{ii}^2 + \sum_{i=1}^3 \sum_{j>i}^3 2f_{ij}^2}{3}} \quad PSD = \sqrt{\frac{\sum_{i=1}^3 p_{ii}^2 + \sum_{i=1}^3 \sum_{j>i}^3 2p_{ij}^2}{3}}$$

$$FSD + PSD = total \quad (3.17)$$

$$Ferri_fraction = \frac{FSD \times 100}{total} \quad Para_fraction = \frac{PSD \times 100}{total}$$

3.4.1 Error estimation

The measurements of high-field magnetic anisotropy are quite time-consuming, so it is important to decide an optimum number of measurement fields. In order to evaluate the precision in determining the slope and intercept, the torque of a test sample was measured in 13 fields, seven of which are above the saturation field. The 2θ -term is represented in Figure 3.1 as a function of B^2 . The ferrimagnetic minerals reach saturation above 200 mT. Above this field the seven coefficients can be fitted with a straight line.

Table 3.1: Estimation of the standard error in percentage for the slope (Δn) and the intercept (Δm) depending on the number of applied fields used in the analysis for a peridotite sample. Ferrimagnetic fraction reaches saturation above 200 mT where the points can be fitted by straight line. The second column contains the time estimation for a complete measurement in the three perpendicular planes with the different number of applied field.

applied fields [T]	Measurement time	Δn	Δm
1.6, 1.8	3.0 h	-	-
1.4, 1.6, 1.8	4.5 h	6 %	3 %
1.0, 1.4, 1.6, 1.8	6.0 h	3 %	2 %
0.8, 1.0, 1.4, 1.6, 1.8	7.5 h	3 %	1 %
0.6, 0.8, 1.0, 1.4, 1.6, 1.8	9.0 h	2 %	2 %
0.4, 0.6, 0.8, 1.0, 1.4, 1.6, 1.8	10.5 h	2 %	1 %

In order to test the dependence on the number of measurement fields used, an initial linear fit was made by using the three highest fields only, and subsequent fits were made by successively incorporating the measurements in the next lower applied field (Table 3.1). The standard error for each of m and n depends on the number of

points used for the linear fit. For example, if the number of points is increased from three to four, a significant improvement in the precision of the fit ensues; the standard error of each variable decreases by a factor of about 2.0. Increasing the number of points from four to five reduces the standard errors by a further factor of 1.2.

The significances of the paramagnetic and ferrimagnetic anisotropies depend on whether the slope and intercept of the line, respectively, differ statistically from zero. These are illustrated by the fiducial limits of the straight line (Figure 3.1) and can be computed with the aid of the Student t-statistic (Cheeney, 1983). These tests are important because the mathematical analyses will usually return values, and it is necessary to know if they are credible.

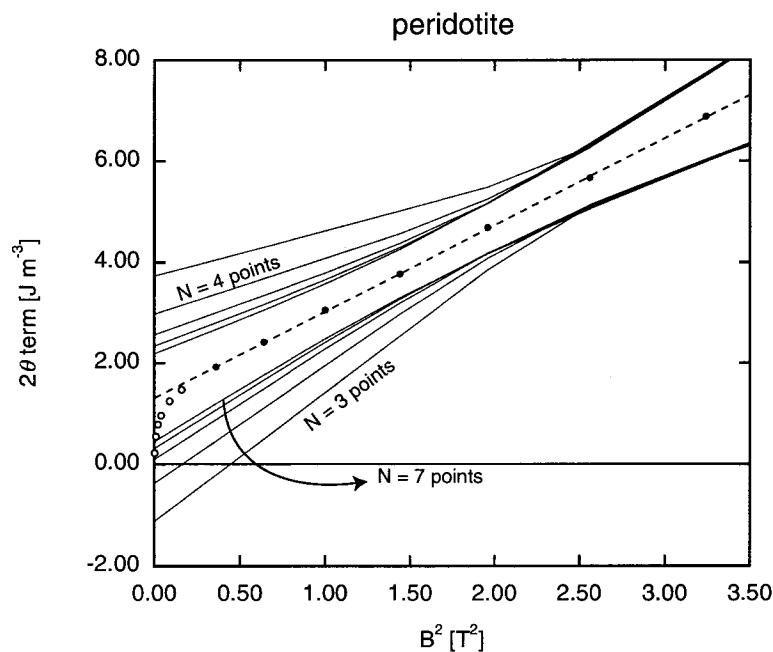


Figure 3.1: Error estimation of the linear fitting of the 2θ -term for a peridotite sample. The sample has been measured in up to thirteen applied fields. Open symbols represent the measurements below the saturation of the ferrimagnetic component and black symbols represent the measurements above the ferrimagnetic saturation. The dashed line is the best fitting straight line, which contains the seven points above the ferrimagnetic saturation. The fiducial limits increase their values as the number of points decreases.

It is also important to take into account the time needed to make a complete measurement. Table 3.1 shows the different times needed to measure a single sample in three perpendicular planes, when using three to seven fields above the field needed to saturate the ferrimagnetic fraction. In the present study, we chose to use four fields

as a compromise between the precision achieved in defining the parameters of the line and the measurement time that this required.

3.5 Application to three different rock types from the Betic Cordillera

The method of separating the components of the magnetic anisotropy was applied to three different rock types from a deformed area in the Betic Cordillera, Southern Spain. The Betic Cordillera forms the western edge of the alpine chain with the Rif and Tell in Northwestern Africa. Three different rock types were sampled from the Betic area (Osete et al., 1998) in order to investigate how different mineral fractions affect the observed magnetic fabric. The rock types include granites (it1) from a tectonic breccia close to the village of Istan, peridotites (oj2) from the Ojén Nappe in the Nevado-Filábride complex and serpentinites (ca3) from the Alpujarride complex (Figure 3.2). A total of ten samples were analyzed from each different rock type.

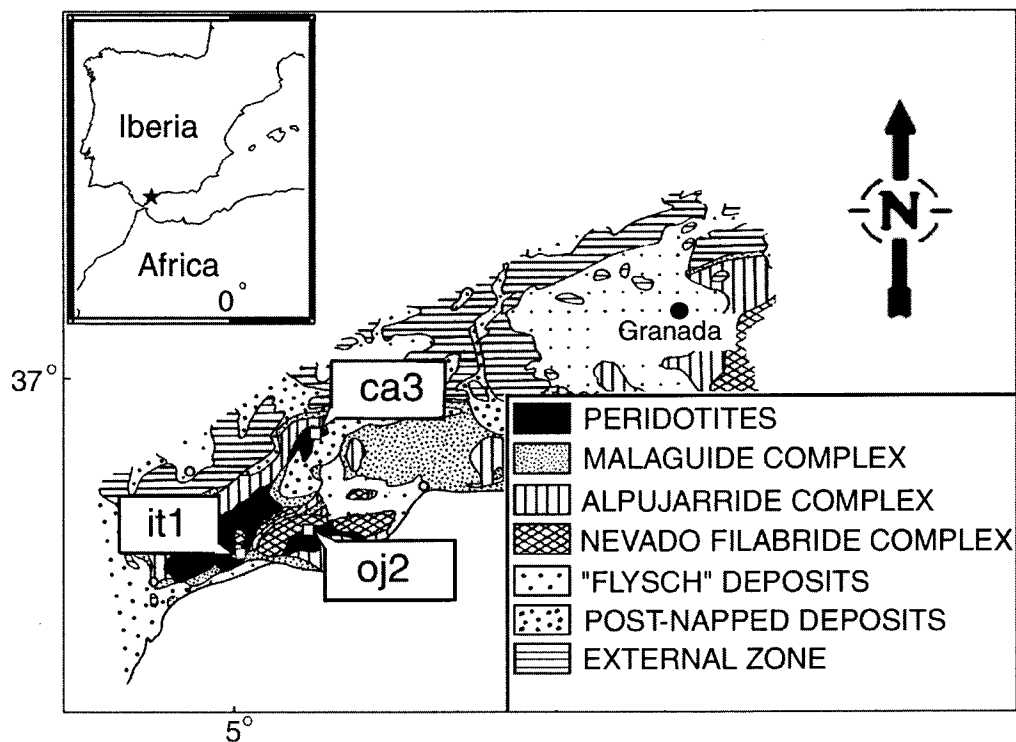


Figure 3.2: Geological sketch map of the Betic Cordillera in Southern Spain.

3.5.1 *Magnetic mineralogy*

Acquisition of Isothermal Remanent Magnetization (IRM) was used to identify the ferrimagnetic mineralogy of the granites, peridotites and serpentinites (Figure 3.3). The samples were exposed progressively to fields up to 1 T, using an electromagnet. A multi-component IRM was then applied to the samples, using the method described by Lowrie (1990), before they were thermally demagnetized. Because the strong magnetization of a serpentinite sample overloaded the magnetometer, a small chip of the sample was used for IRM acquisition. Because the chip was so small, it was not possible to orient it accurately enough to apply cross-component magnetizations before subsequent thermal demagnetization. The samples were heated in a Schonstedt oven and the magnetization was measured on the three-axis, 2G-cryogenic magnetometer.

The granite sample acquires an IRM that is nearly saturated by 1 T (Figure 3.3a). There is an inflexion in the curve at 200 mT, which suggests that two mineral phases are present, one with a low coercivity and another with a higher coercivity. The multiple-component IRM shows that the granites are dominated by minerals whose coercivities are below 600 mT, with a very small harder component (Figure 3.3b). An initial component of magnetization in both coercivity ranges is removed by 80°C (Figure 3.3b). This low unblocking temperature, coupled with the low coercivity components, suggest that a viscous ferrimagnetic component is responsible for the decrease below 80°C. There is a second decrease between 300°C and 350°C, which is diagnostic for pyrrhotite (Dekkers, 1988). The lowest coercivity component is totally unblocked around 575°C, which indicates the presence of magnetite. A small magnetization still remains above 600°C. Since saturation is not reached at 1 T in the IRM acquisition curve, this component is most likely hematite.

The acquisition of IRM for the peridotites shows that a low coercivity mineral that saturates between 200 mT and 300 mT is dominant (Figure 3.3c). The demagnetization curve of three perpendicular components of IRM shows a soft component that is removed by 575°C (Figure 3.3d); this suggests that magnetite dominates the magnetic characteristics. The medium and hard components behave erratically during thermal demagnetization. These components are believed to be artifacts of the measurement procedure, reflecting misalignment of the sample during IRM acquisition and during measurement, which had to be made without a sample

holder. Although the hard component is nearly zero, a small magnetization persists above 575°C, which indicates that a high coercivity phase, e.g. hematite, is present.

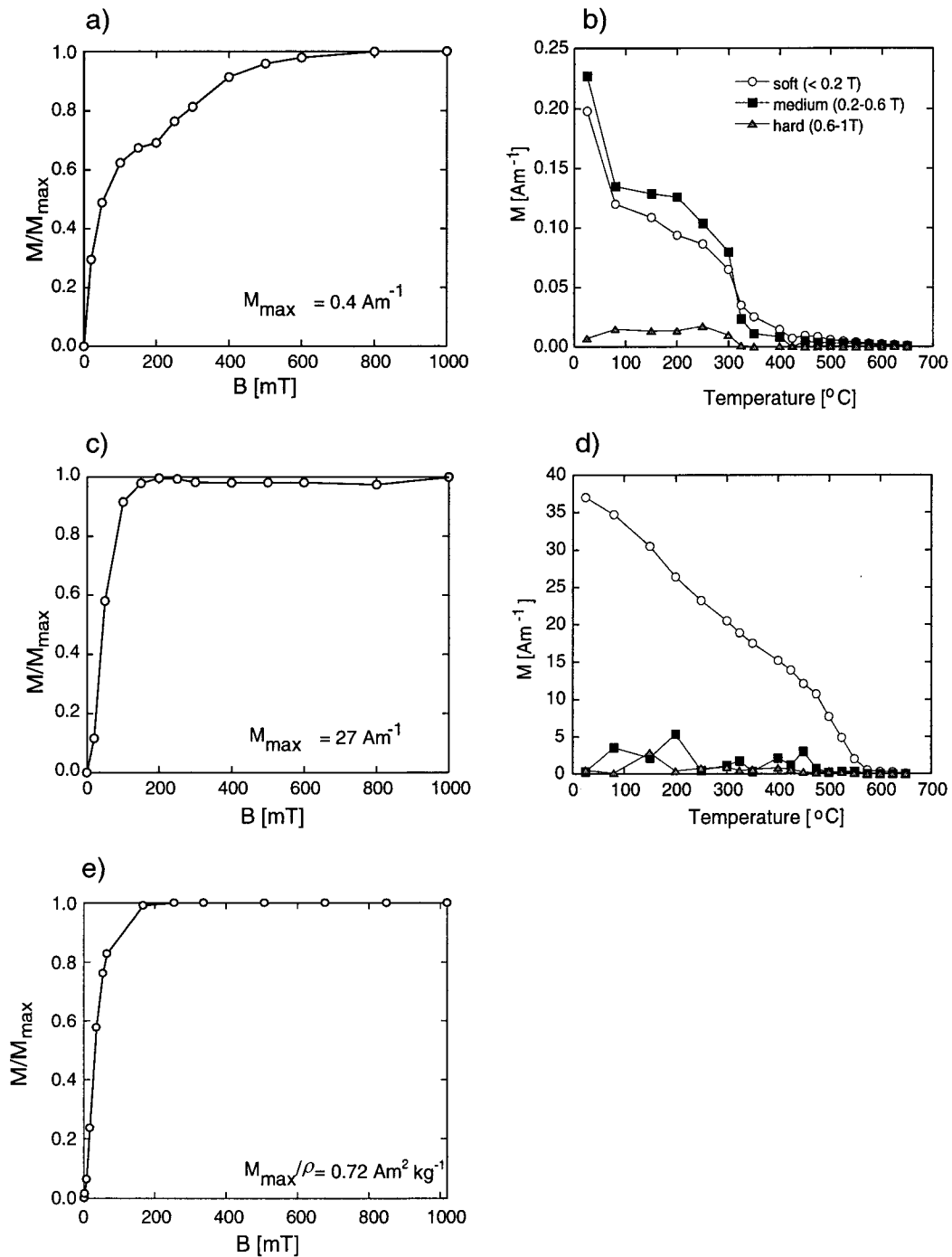


Figure 3.3: IRM acquisition curves and thermal demagnetization of a three orthogonal IRM in (a, b) granites, (c, d) peridotites. (e) IRM acquisition curve of a serpentinite sample; the value of the maximum acquired magnetization is normalized by the mass rather than volume because of the irregular shape of the sample.

The serpentinites contain a ferrimagnetic mineral that is completely saturated around 200 mT (Figure 3.3e). Magnetite appears to be the sole ferrimagnetic mineral in this case.

3.5.2 Anisotropy of magnetic susceptibility

3.5.2.1 Granites (it1)

The granites are weakly magnetic with a mean bulk susceptibility of 5.4×10^{-5} [S.I.] at room temperature (Table 3.2). The magnetic low-field AMS fabric is well defined and the principal axes of the susceptibility are well-grouped in geographic coordinates. The shapes of the susceptibility magnitude ellipsoid are generally oblate but three samples are slightly prolate (Figure 3.4). The prolate ellipsoids tend to have a higher degree of anisotropy. The low-field AMS was also measured at 77 K for several samples. Each of the principal axes of the ellipsoid has been correlated with its correspondent at the two different temperatures. For each individual axis a linear regression has been calculated by a least squares. The results are shown in Figure 3.5. An increase by a factor of about 3.8 would be expected if only paramagnetic minerals dominate the susceptibility. In fact the observed increases for the granites average about 4.5. This suggests that a diamagnetic phase may also contribute to the low-field susceptibility. The orientation of the principal axes does not change significantly at 77 K.

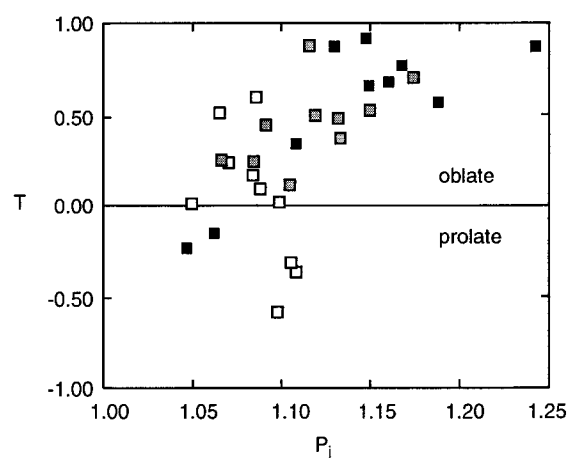


Figure 3.4: Shape parameter T as a function of the anisotropy degree P_j for the three different rock types analyzed. Open symbols represent granites, gray symbols represent peridotites and black symbols represent serpentinites

Figure 3.6a shows the high-field torque per unit volume of the first measurement position as a function of the angular position. The torque is dominated by a 2θ signal and its maximum value increases with the applied field. This behavior indicates that paramagnetic minerals control the anisotropy in the sample. After applying the FFT, the amplitude of the 2θ terms is shown as a function of B^2 in Figure 3.6b. The coefficients lie on a straight line that passes through the origin, which is also indicative of an anisotropy due to the paramagnetic fraction. The average proportion of the paramagnetic anisotropic component obtained by Eq. (3.17) is $94\% \pm 13\%$, and that of the ferrimagnetic component is $6\% \pm 7\%$ (Table 3.3). The directions of the paramagnetic susceptibility ellipsoid calculated from the high-field data show a very good agreement with the directions of the low-field AMS, confirming that the magnetic anisotropy is due to the paramagnetic minerals (Figure 3.7a).

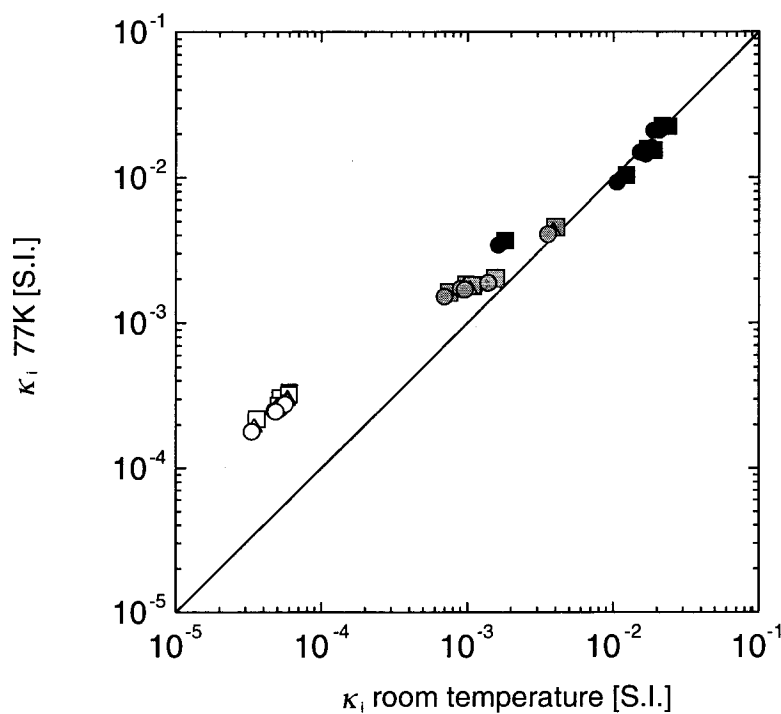


Figure 3.5: Comparison between the magnitudes of the susceptibility ellipsoid axes at room temperature and 77K. Squares represent the maximum susceptibility ellipsoid axes, triangles represent the intermediate axes and circles represent the minimum axes. Measurements for serpentinites are indicated by black symbols, peridotites by gray symbols and granites by open symbols.

3. Separation of ferrimagnetic and paramagnetic anisotropies...

Table 3.2: Mean low field magnetic susceptibility, the values of the normalized low field susceptibility axes with $\kappa_1 \geq \kappa_2 \geq \kappa_3$ and the normalization criteria $\beta = (\kappa_1 + \kappa_2 + \kappa_3)$, Jelinek's T-Parameter and P_j for the studied samples at room temperature.

Sample name		K_{LF} [S.I.]	κ_1	κ_2	κ_3	T	P_j
granite	it101a	6.1×10^{-5}	1.058	0.987	0.956	-0.36	1.11
	it102b	5.3×10^{-5}	1.030	1.015	0.953	0.60	1.09
	it103a	5.8×10^{-5}	1.040	1.002	0.957	0.09	1.09
	it105a	7.2×10^{-5}	1.053	0.982	0.964	-0.58	1.10
	it105b	5.0×10^{-5}	1.048	1.000	0.954	0.02	1.10
	it106a	0.3×10^{-5}	1.038	1.003	0.959	0.17	1.08
	it107a	5.8×10^{-5}	1.031	1.005	0.964	0.24	1.07
	it108a	4.9×10^{-5}	1.025	1.010	0.965	0.51	1.06
	it109a	6.2×10^{-5}	1.055	0.989	0.956	-0.31	1.11
	it110b	4.9×10^{-5}	1.022	1.000	0.976	0.01	1.05
peridotite	oj202a	0.9×10^{-3}	1.037	1.006	0.957	0.24	1.08
	oj203b	0.6×10^{-3}	1.034	1.028	0.938	0.88	1.12
	oj206a	1.2×10^{-3}	1.042	1.000	0.950	0.12	1.10
	oj207b	1.5×10^{-3}	1.047	1.020	0.939	0.50	1.12
	oj208a	3.8×10^{-3}	1.050	1.018	0.934	0.48	1.13
	oj209a	3.0×10^{-3}	1.037	1.013	0.953	0.45	1.09
	oj210b	0.7×10^{-3}	1.029	1.004	0.965	0.25	1.07
	oj211d	0.9×10^{-3}	1.056	1.033	0.911	0.70	1.17
	oj212b	0.8×10^{-3}	1.055	1.022	0.923	0.52	1.15
	oj213b	1.0×10^{-3}	1.049	1.010	0.932	0.37	1.13
serpentinite	ca302a	2.0×10^{-2}	1.049	1.029	0.922	0.66	1.15
	ca303a	2.3×10^{-2}	1.048	1.035	0.912	0.77	1.17
	ca304a	2.3×10^{-2}	1.064	1.050	0.876	0.87	1.24
	ca305a	0.2×10^{-2}	1.023	0.995	0.981	-0.23	1.05
	ca305c	0.2×10^{-2}	1.040	1.006	0.942	0.34	1.11
	ca306a	0.4×10^{-2}	1.034	1.000	0.974	-0.15	1.06
	ca307a	0.1×10^{-2}	1.067	1.029	0.906	0.57	1.19
	ca308b	1.1×10^{-2}	1.052	1.026	0.914	0.68	1.16
	ca310a	1.6×10^{-2}	1.037	1.030	0.933	0.88	1.13
	ca310b	1.8×10^{-2}	1.038	1.033	0.918	0.92	1.15

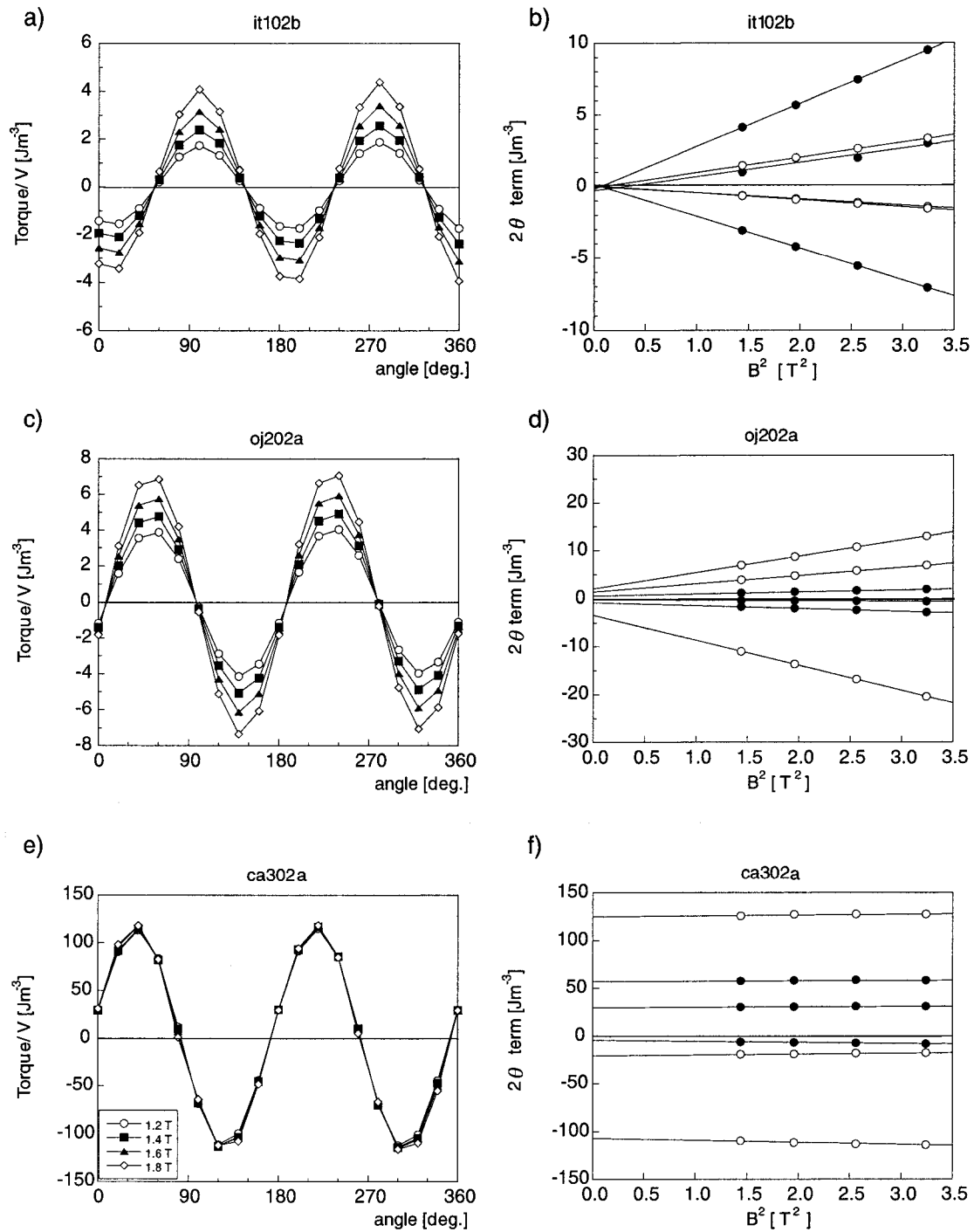


Figure 3.6: Torque per unit volume as a function of angle in four different fields (left), and the amplitude of the 2θ -term as a function of B^2 for the three orthogonal measurement planes (right), where black symbols represent the coefficients of the cosine term and open symbols the sine term in (a, b) granites, (c, d) peridotites and (e, f) serpentinites.

3.5.2.2 *Peridotites (oj2)*

The mean bulk susceptibility is 1.4×10^{-3} [S.I] in the peridotites. This is larger than in the granites, which suggests a larger ferrimagnetic component (Table 3.2). The AMS measurements, however, reveal a more homogeneously shaped oblate ellipsoid, and a total anisotropy higher than in the granites (Figure 3.4). The low-field AMS, measured at 77 K, is similar to room temperature measurements in direction and only slightly larger in intensity (Figure 3.5). These results suggest that the low-field susceptibility is dominated by a ferrimagnetic fraction but that a small paramagnetic contribution is also present.

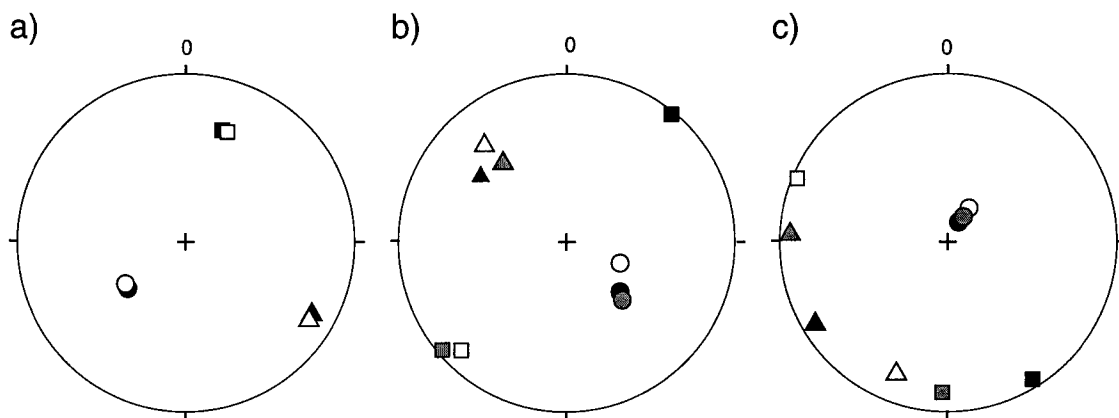


Figure 3.7: Orientation of the principal axes of the magnetic anisotropy in sample coordinates in (a) granite (it106a), (b) peridotite (oj209a) and (c) serpentinite (ca302a). Principal axes are plotted on equal-area, lower hemisphere projections and symbols are described in Figure 3.5. Low-field AMS directions are shown by black symbols, open symbols represent the principal directions of the paramagnetic susceptibility tensor and gray symbols the principal directions of the ferrimagnetic demagnetization tensor.

Figure 3.6c shows the torque per unit volume for a peridotite sample. The amplitude of the torque-signal is greater than in the granites. Figure 3.6d illustrates that, although the 2θ terms of the Fourier analysis can be fitted with a straight line, the line has a non-zero intercept on the y-axis. The anisotropy in these peridotites is due not only to the paramagnetic fraction but also to a ferrimagnetic fraction (Table 3.2). The analysis suggests that on average $46\% \pm 8\%$ of the anisotropy is controlled by paramagnetic minerals and $54\% \pm 7\%$ by ferrimagnetic minerals.

The principal directions of the ferrimagnetic demagnetization tensor and the paramagnetic susceptibility tensor show good agreement with the directions of anisotropy measured at low field. The sample shown in Figure 3.6b contains a large ferrimagnetic anisotropic fraction (Table 3.3) and therefore the susceptibility measured at low field agrees better with the directions of the ferrimagnetic demagnetization tensor, although the directions of the paramagnetic susceptibility tensor are similar to the measured AMS.

3.5.2.3 *Serpentinites (ca3)*

Very high susceptibility values were measured for serpentinites, for which the mean value of the bulk susceptibility is 1.3×10^{-2} [S.I.] (Table 3.2). The magnetic fabric is well defined (Figure 3.7c) with the minimum axes well grouped in geographical coordinates and maximum and intermediate axes forming a girdle that corresponds to the foliation plane, measured in the field. The susceptibility magnitude ellipsoid shows an oblate shape except in two samples (Figure 3.4), and the total anisotropy is large with values up to 14%. The bulk susceptibility does not change significantly at low temperature with respect to room temperature (Figure 3.5).

For the high-field measurements, the amplitude of the torque signal is larger than for the other two rock types and shows almost no dependence on the applied field (Figure 3.6e). This behavior indicates that the anisotropic paramagnetic contribution to the torque is almost zero. Figure 3.6f shows the 2θ terms for serpentinites. The fitted straight line is nearly horizontal and has a positive y-intercept, a further indication that the anisotropy is due mainly to ferrimagnetic minerals. The evaluation of the torque signal attributes $95\% \pm 2\%$ to ferrimagnetic minerals and $5\% \pm 1\%$ to paramagnetic minerals (Table 3.3). The ferrimagnetic minerals in the samples are mainly responsible for the observed AMS. There is a good agreement in the orientation of the K_3 axes. Although the K_1 and K_2 axes of the three tensors are not coaxial, they lie in the foliation plane (Figure 3.7c). Although the paramagnetic contribution to the anisotropy is almost negligible, the minimum axis of the paramagnetic susceptibility ellipsoid separated with the torque analysis is similar in direction to the minimum axes of the ferrimagnetic and AMS ellipsoids.

3. Separation of ferrimagnetic and paramagnetic anisotropies...

Table 3.3: Principal directions of the susceptibility ellipsoids of the low-field AMS, paramagnetic tensor and ferrimagnetic tensor and the contribution of the paramagnetic and ferrimagnetic fractions to the total anisotropy and estimation of the ferrimagnetic and paramagnetic anisotropic materials for samples measured with the high field torque magnetometer.

Sample		D_{max}	I_{max}	D_{int}	I_{int}	D_{min}	I_{min}	%	
granite	it102b	AMS	338.2	47.0	100.5	26.4	207.9	31.1	
		Para.	346.5	50.2	108.9	24.0	213.5	29.6	94±1
		Ferro.	212.5	30.6	109.0	21.5	349.7	51.1	6±5
	it103a	AMS	22.3	44.3	133.1	20.0	240.2	38.9	
		Para.	11.3	36.4	120.6	24.2	236.2	43.8	93±7
		Ferro.	234.6	45.1	91.9	38.4	345.5	19.5	7±6
	it106a	AMS	18.3	31.1	118.2	16.0	231.8	54.2	
		Para.	20.4	31.0	120.2	15.8	233.5	54.3	94±25
		Ferro.	224.6	54.3	109.5	16.9	9.3	30.4	6±10
	it110b	AMS	7.3	38.2	110.7	16.5	219.3	47.1	
		Para.	9.4	38.9	111.5	14.5	217.9	47.9	94±18
		Ferro.	205.9	50.2	102.2	11.1	3.4	37.6	6±7
peridotite	oj202a	AMS	93.6	20.8	235.0	64.1	357.9	14.8	
		Para.	90.9	6.9	234.4	81.4	0.3	5.0	59±5
		Ferro.	93.4	12.2	230.4	73.5	1.0	10.9	41±5
	oj207b	AMS	196.8	62.3	296.9	5.2	29.5	27.1	
		Para.	186.8	23.4	79.5	34.4	303.8	46.3	39±2
		Ferro.	218.6	7.3	122.0	41.9	316.6	47.2	61±2
	oj208a	AMS	208.7	68.7	311.5	4.9	43.3	20.6	
		Para.	235.9	65.0	124.1	9.7	30.0	22.7	12±1
		Ferro.	226.6	67.5	126.1	4.3	34.4	22.0	88±1
	oj209a	AMS	39.4	2.0	308.0	35.7	132.3	54.3	
		Para.	224.5	12.0	320.2	25.0	111.0	61.9	44±1
		Ferro.	229.4	3.2	322.0	39.1	135.5	50.7	56±2
	oj210b	AMS	260.3	42.6	33.6	36.5	144.4	25.6	
		Para.	2.4	67.5	240.0	12.5	145.8	18.4	88±5
		Ferro.	266.2	49.8	26.1	22.8	130.7	31.1	12±4
	oj213b	AMS	64.8	60.5	219.5	27.1	315.1	10.8	
		Para.	99.7	39.1	303.3	48.4	199.5	11.9	37±2
		Ferro.	64.8	55.8	223.4	32.3	319.8	10.0	63±2
serpentinite	ca302a	AMS	148.2	5.4	239.1	9.3	28.7	79.2	
		Para.	292.7	3.2	201.6	19.0	32.1	70.7	1.6±0.6
		Ferro.	181.9	12.4	273.4	7.0	31.9	75.8	97.4±0.8
	ca303a	AMS	142.4	1.7	232.7	12.0	44.6	77.6	
		Para.	351.2	12.5	256.8	18.8	112.8	67.1	2.0±0.1
		Ferro.	334.8	15.0	241.9	10.8	117.5	71.4	98.0±0.2
	ca305c	AMS	138.3	45.2	304.7	44.0	41.3	6.9	
		Para.	50.6	49.1	309.5	9.5	211.6	39.3	12.8±0.6
		Ferro.	158.0	72.0	302.5	14.8	35.1	10.0	87.2±1.1
	ca307a	AMS	9.0	38.6	147.5	43.1	260.0	22.2	
		Para.	19.9	40.5	147.9	35.8	261.5	29.1	5.8±0.1
		Ferro.	26.3	36.9	148.5	35.4	266.5	33.5	93.2±0.1
	ca308b	AMS	27.2	27.5	145.6	42.4	275.7	35.2	
		Para.	25.3	26.7	142.0	41.7	273.4	36.6	5.8±0.2
		Ferro.	32.8	25.9	147.8	41.1	280.6	37.9	93.4±0.1
	ca310a	AMS	105.7	28.8	209.8	23.9	332.9	51.0	
		Para.	173.9	51.9	79.2	3.7	346.3	37.9	2.5±0.1
		Ferro.	198.2	38.2	90.9	20.7	339.0	44.5	97.5±0.2
ca310b	AMS	242.7	3.7	149.6	39.2	337.2	50.5		
	Para.	194.9	51.1	99.7	4.2	6.4	38.6	3.6±0.3	
	Ferro.	192.4	38.0	97.0	6.8	358.6	51.2	96.4±0.5	

3.6 Discussion

Measurement of the AMS on a high-field torque magnetometer allows for the separation of the paramagnetic and ferrimagnetic contributions to the total anisotropy, when fields above the saturation magnetization can be applied. The method presented in this paper has advantages over earlier methods. In contrast to Hrouda and Jelinek (1990), whose analysis is based upon computation of a standard deviatoric energy density, the direct analysis of the 2θ component derived from the torque measurements is intuitively simpler. Moreover, instead of only two fields as described by Owens and Bamford (1976) and Lowrie (1989), our method uses a larger number of fields, thereby providing a more accurate definition of the paramagnetic susceptibility tensor and demagnetization tensor. It is also possible to calculate an error parameter for the estimation of the paramagnetic and ferrimagnetic contributions to the torque signal.

In granites, the paramagnetic minerals control the AMS. For this reason the directions of the principal axes of the low-field susceptibility ellipsoid and the paramagnetic ellipsoid agree well (Table 3.3). The ferrimagnetic solutions are not significant statistically.

The magnetic anisotropy of the peridotites provides an example of a mixed magnetic fabric. A good agreement has been found between the directions of the ferrimagnetic and the paramagnetic minerals. The κ_3 axes are generally grouped for the three tensors, although there is often a better agreement between the low-field AMS and the magnetic component that is larger (Table 3.3). There is also a good agreement between the κ_1 and κ_2 axes of the dominant component and the low-field AMS.

In serpentinites, the ferrimagnetic minerals dominate the magnetic anisotropy and the paramagnetic contribution is small. Where the paramagnetic part is significant, the minimum axes agree with those of the ferrimagnetic and AMS ellipsoids. Because of the oblateness of the ellipsoids the distinction between maximum and intermedium axes is not well defined and they are distributed in a girdle subparallel to the foliation plane.

The method developed in this paper has the advantage of splitting the two different components of the magnetic anisotropy with only one instrument and from one measurement method. As with all torsion magnetometer analyses, it is necessary,

however, to make an independent measurement of one of the principal susceptibilities to obtain the full tensor. High-field torque measurements can also provide useful additional rock magnetic information about the carriers of the magnetic anisotropy. The presence of higher order harmonics in the Fourier analysis indicates if preferential alignment of magnetocrystalline anisotropies contribute to the AMS. In this case cubic minerals such as magnetite would make a 4θ contribution and triaxial minerals would lead to a 6θ contribution to the torque curves.

4. Magnetic properties of phyllosilicates

The anisotropy of magnetic susceptibility of single crystals of biotite, muscovite and chlorite has been measured in order to provide an accurate value for the AMS of these common rock-forming minerals. The low-field anisotropy of susceptibility and the anisotropy of the crystals from a high-field torque magnetometer were defined. The combination of high-field torque magnetometer measurements with the paramagnetic bulk susceptibility obtained from magnetization curves in the crystal permit the definition of the full paramagnetic susceptibility tensor. The paramagnetic component of the susceptibility anisotropy is consistent with the crystallographic structure of phyllosilicates. In the crystals where the ferromagnetic phases have a significant contribution to the high-field anisotropy, the principal axes of the ferromagnetic anisotropy agree with the low-field measurements. The ellipsoid of paramagnetic susceptibility obtained for the three phyllosilicates is highly oblate in shape. The magnetic susceptibility of biotite has been measured within the basal plane. The results confirm that the basal plane is isotropic. The degree of anisotropy in the three minerals is higher than what has been reported in the literature.

Seite Leer /
Blank leaf

4.1 Introduction

The first reported values of magnetic properties of phyllosilicates were determined for the bulk magnetic susceptibility (Syono, 1960; Hood and Custer, 1967). Compositional analysis revealed how the magnetic susceptibility is related to the cation content in the samples. This led to empirical and theoretical formulas that correlate the cation content with the bulk susceptibility (Rochette, 1987). Later a temperature dependence was introduced in the formula (Rochette et al., 1992).

The layered structure of phyllosilicates suggests that the analysis of their magnetic properties will be dependent on orientation. Using Mössbauer spectroscopy in two orthogonal directions, parallel and perpendicular to the basal plane, the magnetic properties of phyllosilicates were modeled, dividing them according to their structure. The 1:1 layer minerals, with kaolinite and antigorite as the most important members, have magnetic ordering at 10 K and a strong planar symmetry (Coey et al., 1981). Their study reveals the presence of a ferromagnetic interaction between ferrous cations while the ferric cations present an antiferromagnetic interaction, below the ordering temperature.

The 2:1 layer minerals, corresponding to the mica group, have a similar behaviour (Ballet and Coey, 1982). The magnetization curves and susceptibility below the ordering temperature of these phyllosilicates shows that there is a weak interplane interaction of antiferromagnetic character. With a simple model of isotropic distribution of ferric cations and trigonal distribution of ferrous cations it is possible to estimate the paramagnetic constant of this interaction.

Biotite is the phyllosilicate whose magnetic anisotropy is best known. Ballet and Coey (1982) modeled the magnetic anisotropy of micas as due to the anisotropic configuration of ferrous cations in the crystal, with an isotropic interaction of the ferric cations. In their study the magnetic susceptibility of two biotite crystals were measured. The magnetic behaviour of eight samples of biotite was determined by Beausoleil et al. (1983) who found $\kappa_{\perp}/\kappa_{\parallel} = 1.25$.

Borradaile et al. (1987) reported on the AMS of two biotite single crystals, measured with an induction coil, where the degree of anisotropy was $P_j = 1.40$ and the shape of the anisotropy ellipsoid was $T = 0.97$. Ten biotite single crystals were measured by Zapletal (1990) in low-field with a KLY-2 in order to determine a

representative value of their magnetic anisotropy. Although the samples were selected because of their low ferromagnetic content it was shown that they acquired an IRM in fields up to 1 T. The directions of the anisotropy of remanence varied with the applied field, showing the possibility of a ferromagnetic contribution to the measurements.

An advancement in the determination of the magnetic anisotropy of biotites was made by applying high-field methods for the isolation of the paramagnetic component of the anisotropy (Borradaile and Werner, 1994). Twenty-nine crystals were analyzed, using measurements of hysteresis loops. A mean anisotropy degree of $P_j = 1.74$ was determined, which is higher than the values reported previously. The mean shape factor was found to be $T = 0.67$, less oblate than expected due to the presence of some samples, which had prolate ellipsoids.

Magnetic properties of muscovite have been given in Ballet and Coey (1982). They showed a ferromagnetic interaction in the basal plane, characterized by a positive paramagnetic Curie temperature, and an antiferromagnetic interaction perpendicular to the basal plane, with negative Curie temperature. Borradaile et al. (1987) reported a single value of the anisotropy of magnetic susceptibility in a crystal of muscovite, where the anisotropy degree found was $P_j = 1.43$ and the shape parameter $T = 0.44$. A later study by Borradaile and Werner (1994) analyzed the anisotropy of the paramagnetic susceptibility using hysteresis loops. They obtained a broad range of values, which included prolate anisotropies. The average ellipsoid is characterized by an anisotropy degree $P_j = 1.26$ and an oblate ellipsoid with shape parameter $T = 0.67$.

Little work has been done on the determination of the magnetic anisotropy of chlorite. Ballet et al. (1985) reported on the anisotropy of the magnetic susceptibility, where they found a positive paramagnetic Curie temperature in the basal plane and a negative value perpendicular to the basal plane. Borradaile et al. (1987) examined four single crystals of chlorite measured with an induction coil instrument. They reported a value of $P_j = 1.38$ and $T = 0.43$. Further investigations using high field methods separated the ferromagnetic component due to impurities from the paramagnetic signal of the crystal. Using this method, Borradaile and Werner (1994) analyzed a large number of single crystals and found $P_j = 1.53$ and $T = 0.28$. The average value of the shape parameter is close to neutral due to some samples with prolate ellipsoids or an inversion of the magnetic susceptibility axes, in which the

maximum susceptibility lay along the crystallographic c-axis. This results in a high scatter in the data.

It is important to establish reliable values for the magnetic properties of phyllosilicate single crystals, since they are responsible for the magnetic anisotropy in weakly magnetic rocks. For example, it has been found that paramagnetic minerals are often the carriers of the magnetic anisotropy in mudrocks (Hounslow, 1985), slates (Borradaile et al., 1985/86) and shales (Hirt et al., 1995).

This chapter presents reliable values of the magnetic susceptibility for single crystals of biotite, chlorite and muscovite. This can only be obtained from high-field measurements on a torque magnetometer, which allows for the isolation of the anisotropy of the paramagnetic susceptibility (Martín-Hernández and Hirt, 2001).

4.2 Crystallographic description of phyllosilicates

Phyllosilicates or sheet silicates are composed of layer sheets $(\text{Si,Al})\text{O}_4$ composed of SiO_4 tetrahedral structures (Figure 4.1a). In addition, octahedral layers of $(\text{Fe,Mg})\text{O}_6$ or AlO_6 are also present in phyllosilicate minerals (Figure 4.1b). Each of these two structures forms single layers stacked in different configurations to build the whole group of phyllosilicates. Individual layers are interconnected by weak Van der Waals forces.

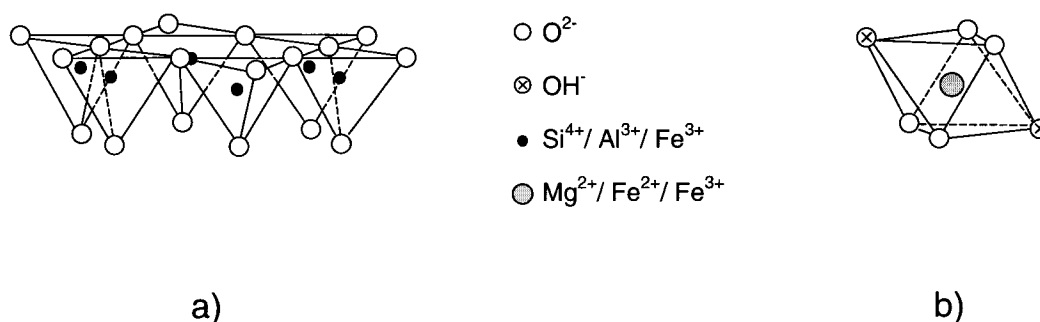


Figure 4.1: Simplified design of the main crystallographic structures present in phyllosilicates. a) two-dimensional basic sheet in which cations are tetrahedrally coordinated by oxygen and b) octahedral cell with hydroxyl groups (modified from Coey et al.(1981)).

Mica like biotite and muscovite form the simplest group of phyllosilicates. The general structure has an octahedral layer sandwiched between two identical

tetrahedral layers. Such a structure is called a 2:1 layer configuration (Figure 4.2). Sheet silicates belonging to this group can be subdivided into subgroups depending on the nature of the cations between the two tetrahedral layers. The most important subgroups are talc, mica, vermiculite and smectite.

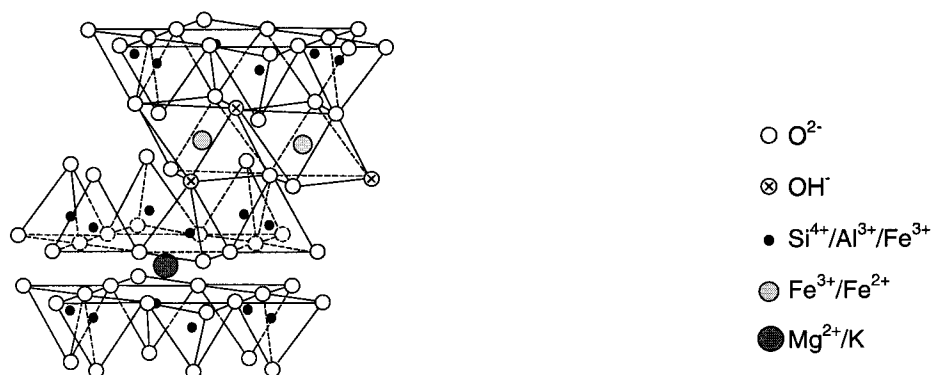
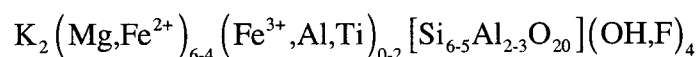


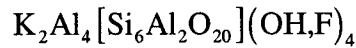
Figure 4.2: Spatial configuration of tetrahedral and octahedral layers for a general mica (modified from Ballet and Coey (1982)).

The term biotite is used to describe an iron-rich phyllosilicate from this group. It is part of a continuous chemical and structural series with phlogopite and it is one of the most common rock-forming minerals, present in pegmatites, granites, slates and shales, gabbros and basalts. In biotites, the octahedral sites are completely filled by Si and Al. A general chemical composition is given by the following formula, although it varies within the series (Deer et al., 1975):



The color of biotite ranges from black to dark brown, reddish brown or green depending on the Mg/Fe proportion in a specimen.

Muscovite is another common rock-forming mineral, and it is found in shales, slates and granites. Muscovite also belongs to the 2:1 structural group (Figure 4.2). In muscovite one quarter of the tetrahedral sites are occupied by Al and three-quarters by Si. The twelve-fold coordinated positions between composite layers are fully occupied by K. The general formula that describes the muscovite chemical composition is (Deer et al., 1975):



The more complicated structure, to which the chlorite group belongs, is the so-called 2:1:1 structure. It consists of a 2:1 layered structure in addition to a single sheet of cations octahedrally coordinated by hydroxyls (Figure 4.3).

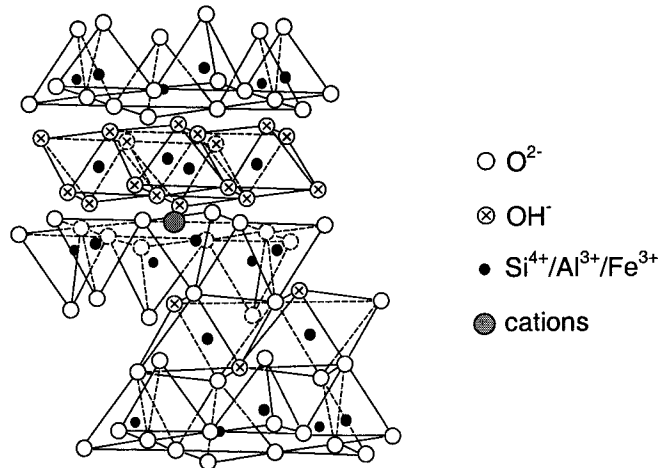
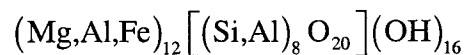


Figure 4.3: Chlorite (or 2:1:1 layer) structure (after Ballet et al. (1985)).

There are multiple variations of the Fe²⁺, Fe³⁺, Si or Mg content within the series as well as substitutions or alterations in the layer sequence. The general formula is (Deer et al., 1975):



Chlorite color depends on its composition. In general it shows a dark blue color, green, brown or yellowish tones. Chlorite is widely distributed in low-grade metamorphic rocks and is the most characteristic mineral of the greenschist facies. It is also present in igneous rocks and argillaceous rocks.

Phyllosilicates are monoclinic as a result of the layered structure. They have a perfect cleavage and hexagonal shape of the basal plane for single crystals. Paramagnetic behavior of phyllosilicates is mainly due to the presence of Fe and Mn cations in the crystallographic structure of the crystals. The sheet structure confers an anisotropic distribution of the cations in the crystal. The iron-iron distance between

planes is much greater than within the plane. The magnetic properties have a two-dimensional character with two equal magnetic susceptibility directions in the basal plane and the minimum c-axis perpendicular to it (Figure 4.4).

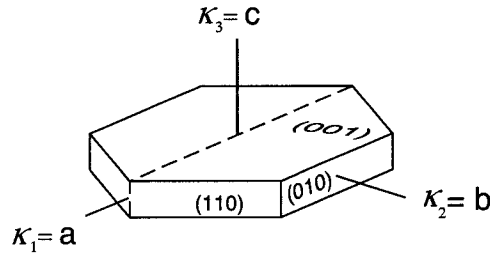


Figure 4.4: General illustration of crystallographic and magnetic susceptibility axes of a general phyllosilicate single crystal (modified from Deer et al. (1975)).

4.3 Samples description

The analyzed crystals were selected from different geographic localities in order to check whether the magnetic susceptibility of the crystal is independent on the ferromagnetic content or the composition of the crystal. Each crystal was cut in a different number of specimens (Table 4.1).

Table 4.1: Weight and origin of the analyzed single crystals. (1) Bancroft, Canada, (2) Swiss Alps, (3) Bear Lake, Canada, (4) Madras, India, (5) Zermat, Switzerland and (6) unknown locality. The densities used (ρ_{bio} , density of biotite, ρ_{chl} , density of chlorite and ρ_{mu} , density of muscovite) are reported by Deer et al. (1975).

biotite	mass (g)	loc	muscovite	mass (g)	loc	chlorite	mass (g)	loc
bio1.01	0.1833	(1)	mu1.01	4.3692	(2)	chl1.01	2.0472	(5)
bio1.02	0.1460	(1)	mu1.02	3.7698	(2)	chl1.02	3.1319	(5)
bio1.03	0.9286	(1)	mu1.03	0.8499	(2)	chl1.03	3.0872	(5)
bio1.04	0.6362	(1)	mu2.01	0.8210	(4)	chl2.01	3.9634	(6)
bio2.01	0.3389	(1)	mu2.02	0.4429	(4)	chl2.02	3.9649	(6)
bio2.02	0.5455	(1)	mu2.02	0.5473	(4)	chl3.01	8.4671	(2)
bio3.01	4.6900	(2)	mu3.01	1.6042	(4)	chl4.01	0.7215	(2)
bio4.01	0.2906	(2)	mu3.02	1.3225	(4)	chl4.02	0.4725	(2)
bio5.01	2.4499	(1)	mu3.03	1.2578	(4)	chl4.03	0.6654	(2)
bio6.01	11.949	(3)				chl5.01	4.2054	(5)
bio6.02	8.0893	(3)				chl5.02	1.6525	(5)
$\rho_{bio} = 2.9 \text{ [g cm}^{-3}\text{]}$			$\rho_{mu} = 2.8 \text{ [g cm}^{-3}\text{]}$			$\rho_{chl} = 2.7 \text{ [g cm}^{-3}\text{]}$		

The individual specimens have rectangular shape and they have been mounted into plastic boxes, attached to the holder with non-magnetic glue. The samples were oriented in the holder with the crystallographic c-axis in the E-W direction, as perpendicular to the base of the holder cylinder as possible or 45° tilt of the basal plane.

4.4 Measurement procedure

Two different types of measurements have been done to analyze the magnetic properties of phyllosilicates: measurement of the anisotropy of magnetic susceptibility and measurements of bulk magnetic properties. Some of the mineral magnetic analyses have been made as a function of the orientation of the samples.

The low-field anisotropy of magnetic susceptibility was measured on a KLY-2 susceptibility bridge from AGICO (see section 2.4.2.1) where the magnetic susceptibility is fitted by an ellipsoid with principal axes $\kappa_1 \geq \kappa_2 \geq \kappa_3$. In some selected samples the AMS was measured at the temperature of liquid nitrogen, in order to enhance the paramagnetic signal of the magnetic susceptibility (see section 2.2.2).

The high-field magnetic anisotropy was then measured on a high-field torque magnetometer (Bergmüller et al., 1994). The samples were measured in four fields above 1200 mT, which is high enough to saturate the ferrimagnetic inclusions in the crystals. The processing of the obtained signal allows separation of the paramagnetic and ferromagnetic components using the method reported by Martín-Hernández and Hirt (2001) (see Chapter 3).

A small chip was cut from each crystal to measure hysteresis properties. The paramagnetic susceptibility was defined from the slope of the hysteresis curve above the saturation of the ferrimagnetic minerals (see section 2.4.1.5). Three mutually perpendicular measurements were made to estimate a mean bulk paramagnetic susceptibility for each crystal. One of the measurements was always normal the other two within the basal plane. The bulk value is added to the deviatoric paramagnetic tensor obtained from measurement on the high-field magnetometer to compute the full paramagnetic tensor. Both the low-field AMS and the high-field paramagnetic tensor were normalized with the following criterion: $\kappa_1 + \kappa_2 + \kappa_3 = 3$.

The magnetic susceptibility was also analyzed at low temperature. It was determined from the slope of the magnetic hysteresis curves in high-field, measured at different temperatures on a PCM-VSM equipped with a cryostat at the Institute of Rock Magnetism, University of Minnesota. During the experiment hysteresis curves were measured from 10 K up to 300 K using measurement steps of 10 K.

IRM acquisition curves were done in order to characterize the ferromagnetic phases present in the different phyllosilicate crystals (see section 2.4.1.3). Samples were measured up to a maximum field of 1 T, magnetizing them in an electromagnet at diverse field intervals.

The magnetization of the biotite and muscovite crystals has also been studied at low temperature, using a Quantum Design MPMS2 susceptometer at the Institute of Rock Magnetism, University of Minnesota. The samples were cooled down to 10 K in a saturating field of 2.5 T. The samples were subsequently thermally demagnetized in zero field up to 300 K, with measurements made after thermal steps of 5 K. The variations in the magnetization allow the identification of the ferromagnetic phases in the sample. A second experiment, done with the same instrument, consisted of measuring the magnetization when the sample was cooled down in zero field conditions after magnetizing it at room temperature with a saturating field of 2.5 T. The sample was subsequently thermally demagnetized in zero field and measured between 10 K and 300 K. The differences between the field-cooled and zero-field-cooled curves allow for the identification of ferromagnetic phases.

4.4.1 *Mössbauer spectrometry*

One of the most useful methods for estimating the iron content in minerals is Mössbauer spectrometry, which is based on recoil-free emission and absorption of γ radiation by the nucleus of solid materials. When a nucleus is bombarded by γ -rays, it jumps to a higher energy level and emits a lower energy photon on return to the initial state. If the nucleus is located in a crystal lattice there is no recoil effect in the process. The difference in energy between the absorbed and emitted photon is the energy of the transition experienced by the nucleus. The absorption is a function that depends on the oxidation state and the crystallographic location of the nucleus. The main features of a Mossbauer spectrogram are the isomer shift (δ), produced by an

interaction between electric monopoles that arises from the difference in s-electron densities of the emitting and absorbing nuclei. The other feature is the quadrupole splitting (Δ) that occurs when an electric gradient acts in the nucleus and therefore is sensitive to the oxidation state, coordination number and site distribution. The isomer shift δ allows the identification of the cations (Figure 4.5a) and the Δ quadrupole splitting their spatial configuration (Figure 4.5b). A good summary of the physical principles that govern Mössbauer analysis can be found in Murad (1988). The most recent techniques in data processing are reported in Rancourt (1998).

Fitting the measurements with Lorentzian shape doublets, it is possible to identify the ferric and ferrous cations and their crystallographic location. The method provides information about the fractions of the different cations in the population. The relation between spectral area (A) ratios and population (N) ratios for the ferric and ferrous species is:

$$A^{3+}/A^{2+} = (f^{2+}/f^{3+})(N^{2+}/N^{3+}) \quad (4.1)$$

where A^i is the area subtended by the fitted function for a specific cation, N^i is the population of this cation in the sample and f^i is the *recoilless fraction*, or energy that is transformed by the nuclei after the photon impact. In most cases the recoilless fraction can be neglected.

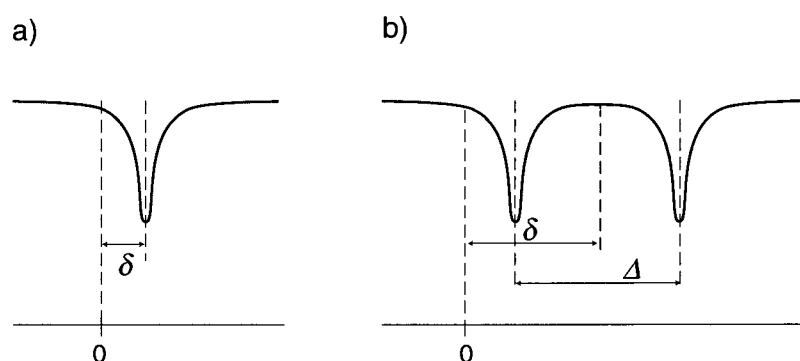


Figure 4.5: a) Single-line absorption spectrum and isomer shift (δ) with respect to the zero and b) elemental doublet with the definition of quadrupole splitting (Δ) (modified after Rancourt (1998)).

A powder from each biotite crystal was prepared. Samples were measured in a Ranger Scientific Mossbauer Spectrometer operating at room temperature with a ^{57}Co radioactive source for the γ -rays, at the Institute for Rock Magnetism, University of Minnesota.

4.5 Biotite

4.5.1 Rock magnetic properties of biotite

4.5.1.1 IRM acquisition curve

In order to identify the ferromagnetic phases present in biotite crystals, IRM acquisition curves were measured on one specimen of each analyzed crystal (Figure 4.6). The results show the presence of a low coercivity phase that saturates between 300 mT and 400 mT in all specimens, which is probably due to the presence of magnetite inclusions in the crystal. The presence of a low coercivity phase in biotite crystals has been pointed out by Zapletal (1990). The ferromagnetic phase in his work had a slightly higher coercivity and was identified as magnetite or maghemite. Borradaile and Werner (1994) characterized the ferromagnetic inclusions of biotite crystals mainly as multidomain magnetite grains.

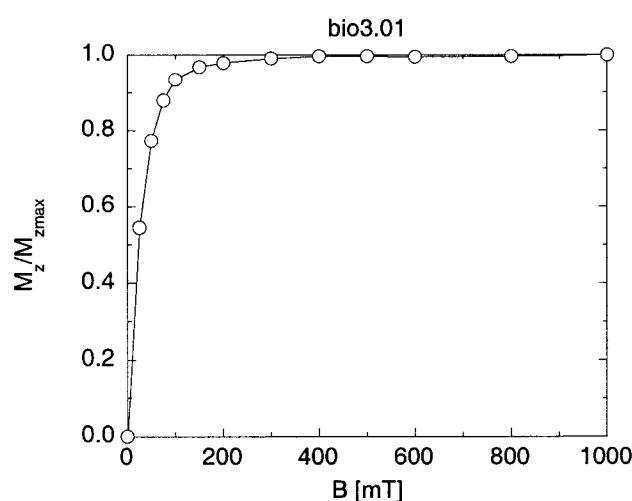


Figure 4.6: IRM acquisition curve in a biotite crystal. The field is applied in a direction contained in the basal plane.

4.5.1.2 Magnetization at low temperatures

The behavior of biotite at low temperatures was analyzed in six different samples to check for the paramagnetic purity of the crystals using the methods described in section 4.4. Stepwise thermal demagnetization of the field-cooled specimen is shown in Figure 4.7. The presence of changes in the magnetization can be correlated with the blocking temperature of the ferromagnetic minerals, changes in the crystallographic configuration at low temperatures or ordering effects at low temperatures.

All the samples present a sudden drop in the remanent magnetization at temperatures ranging between 110 and 130 K (Figure 4.7). It can be due to the magnetite Verwey transition where magnetite changes its crystallographic configuration from cubic to monoclinic (Verwey, 1939) or warming through the isotropic point, where the magnetocrystalline anisotropy constant κ_1 changes sign (Syono, 1960). This transition shows the presence of pure magnetite either that is of multidomain grain size or that is made up of interacting single domain grains. Another change in the magnetization occurs between 30 and 35 K. This systematic change in all the crystals is due to the magnetic ordering of biotite. The low temperatures measurements show that the crystals undergo ordering below 30 K which is expected for biotite but also shows a transition between 110 and 130 K that indicates the presence of pure magnetite.

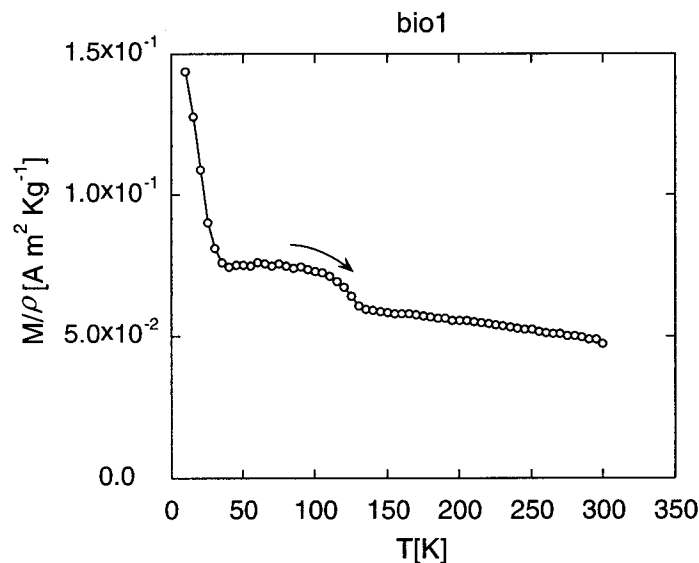


Figure 4.7: Thermal demagnetization of a SIRM acquired after an initial cooling to 10 K in a saturating field of 2.5 T.

4.5.1.3 Hysteresis loops and magnetic susceptibility at low temperatures

The magnetic susceptibility was also analyzed at low temperature. In this experiment the magnetic susceptibility was obtained from the slope of the magnetic hysteresis loop at different temperatures between 10 K and 300 K. The hysteresis shows magnetic ordering below 30 K. The loops remain closed but they are no longer linear and the magnetization resembles the paramagnetic Langevin function (Figure 4.8a).

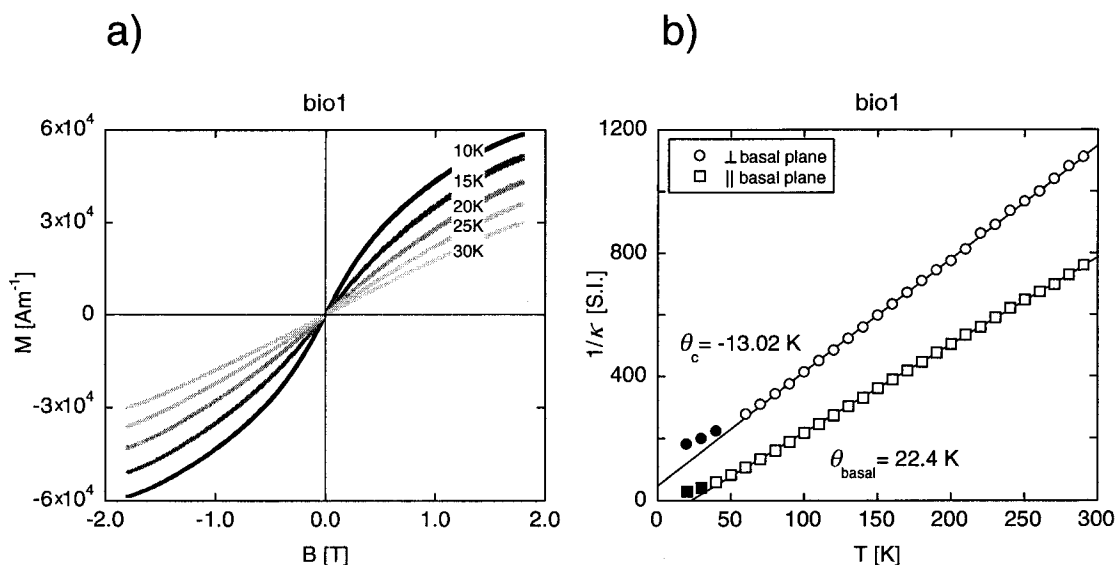


Figure 4.8: a) Magnetic hysteresis loops at different temperatures in a biotite crystal. b) Inverse of the magnetic susceptibility as a function of temperature in two mutually perpendicular planes, one measurement within the basal plane and one parallel to the crystallographic c -axis.

Magnetic susceptibility follows the Curie-Weiss law above the ordering temperature (Figure 4.8b). The paramagnetic Curie temperature and Curie constant can be derived and are listed in Table 4.2. The values obtained for the Curie constant are consistent with those reported in the literature and are more homogeneous than those reported by Beausoleil et al. (1983). The largest deviation is found in sample bio4, but the value is still within the range reported in the literature.

Table 4.2: Experimental paramagnetic Curie constant (C) and paramagnetic Curie temperature (θ) in the biotite crystals. Measurements were done parallel (\parallel) and perpendicular (\perp) to the basal plane. Empty cells are data are data not measured.

sample	θ_{\parallel} [K]	C_{\parallel} [S.I. \times K]	θ_{\perp} [K]	C_{\perp} [S.I. \times K]
bio1	22.4	0.2727	-13.2	0.3532
bio2	21.5	0.4398	-13.8	0.3565
bio3	22.5	0.4161		
bio4	12.6	0.3353		
bio5	29.1	0.2845		
bio6	22.3	0.3192		

4.5.1.4 Magnetic susceptibility in the basal plane

It is uncertain whether magnetic susceptibility within the basal plane of mica is isotropic or not. In some studies, the minimum susceptibility was reported to deviate 5° with respect to the crystallographic c -axis, as a result of the location of the cations in the octahedral sites (Borradaile and Werner, 1994). In other works the direction normal to the basal plane has been considered the hard direction of magnetization, i.e., the minimum direction of susceptibility (Ballet and Coey, 1982). In order to check for possible anisotropy in the basal plane of biotite, the magnetic susceptibility has been evaluated as a function of orientation within the plane. The magnetic susceptibility has been determined from the slope of the hysteresis loop above the saturation of the ferromagnetic phases. The samples were measured on a VSM at intervals of 10° from 0 to 360° . The directional magnetic susceptibility has been represented as a function of the orientation in Figure 4.9.

The measured data were fitted with Fourier analysis to define the harmonic of a series of trigonometric function. The differences found between a circle that is represented by the first Fourier coefficient and the function of the best-fit ellipse never exceeded 4%. It is not possible to distinguish whether the deviation from a circle is due to an anisotropy or to a possible misorientation of the crystal in the instrument. The magnetic susceptibility can be considered isotropic in the basal plane of biotites for the accuracy at the level of the measurements done. The minimum susceptibility axis is thus perpendicular to the basal plane, which implies that there is no interaction between the biotite sheets, at least at room temperature conditions.

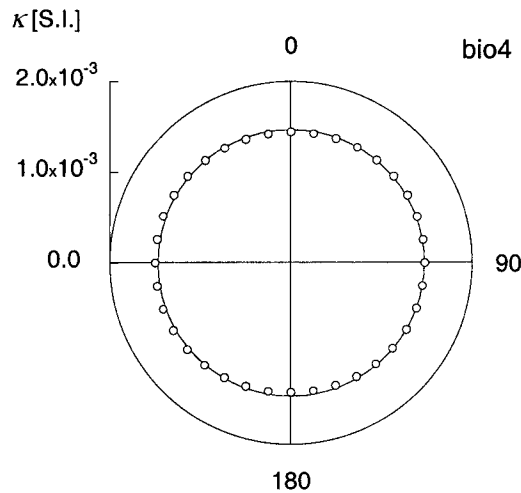


Figure 4.9: Paramagnetic susceptibility of a biotite crystal in the basal plane. Solid line represents the best-fit centered circle to the magnetic susceptibility and open circles represent measured values.

4.5.1.5 Mössbauer spectrometry

A Mössbauer spectrum was measured for four biotite crystals. The samples were prepared to powder. A least squares fit with three Lorentzian shape doublets was used to identify the presence of ferrous octahedral cations [Fe^{2+}], ferric octahedral cations [Fe^{3+}] and tetrahedral ferric cations ($\langle \text{Fe}^{3+} \rangle$). The spectra reveal the homogeneous composition of the biotite crystals, but there is variability in the proportion of iron (Figure 4.10). None of the samples shows signs of hyperfine splitting which would indicate the presence of ferrimagnetic phases.

In the specific case of biotite the recoilless fraction measured is nearly 1 (Lalonde et al., 1998). Therefore the ratio of subtended areas is proportional to the ratio of population in Eq. (4.1). The ratio of $\text{Fe}^{2+}/\text{Fe}^{3+}$ in the analyzed biotites is summarized in Table 4.3.

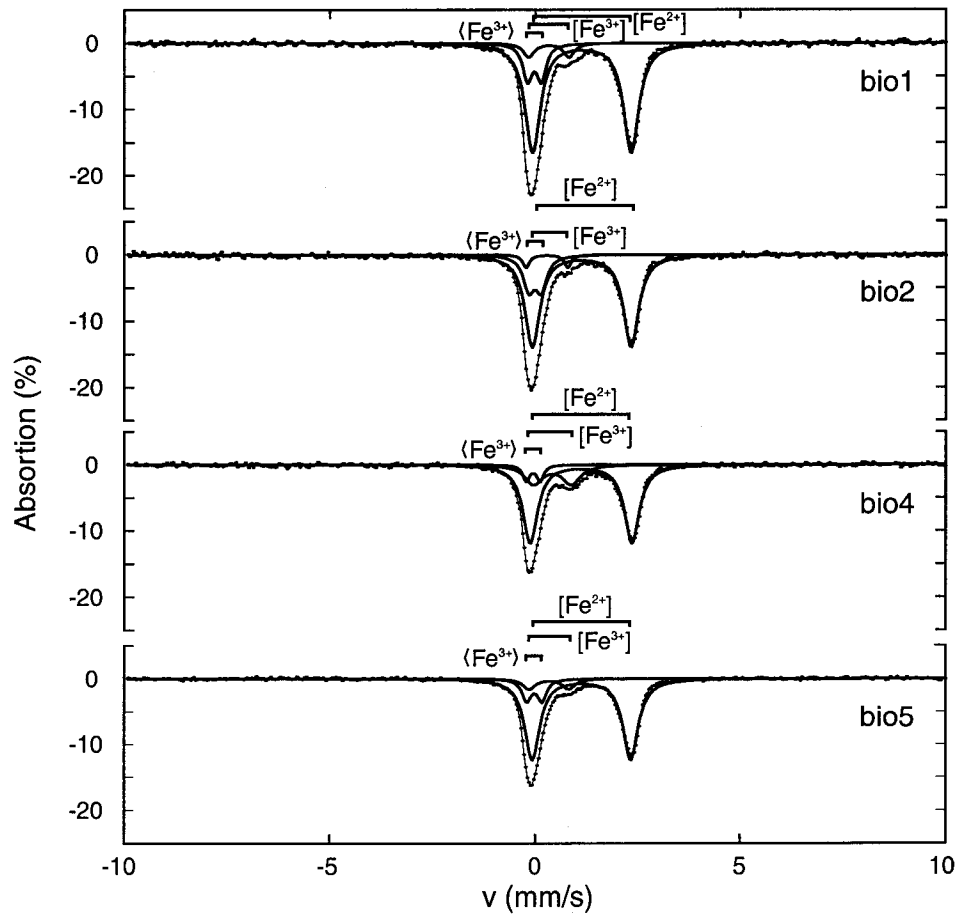


Figure 4.10: Mössbauer spectra of biotite powder samples. Dots correspond to the measurements, the curves correspond to the best fit Lorentzian function where $\langle \text{Fe}^{3+} \rangle$ corresponds to tetrahedral ferric cations, $[\text{Fe}^{3+}]$ to octahedrally coordinate of ferric cations and $[\text{Fe}^{2+}]$ to octahedrally coordinate of ferrous cations.

Table 4.3: Mössbauer data for the biotite samples.

sample	site	δ [mm/s]	Δ [mm/s]	Fe^{2+} (%)	$\text{Fe}^{2+}/\text{Fe}^{3+}$
bio1	$[\text{Fe}^{2+}]$	1.143	2.416	81	3.4
	$[\text{Fe}^{3+}]$	0.335	0.992		
	$\langle \text{Fe}^{3+} \rangle$	-0.021	0.336		
bio2	$[\text{Fe}^{2+}]$	1.140	2.421	74	3.0
	$[\text{Fe}^{3+}]$	0.288	1.026		
	$\langle \text{Fe}^{3+} \rangle$	-0.007	0.303		
bio4	$[\text{Fe}^{2+}]$	1.129	2.495	77	2.5
	$[\text{Fe}^{3+}]$	0.430	0.929		
	$\langle \text{Fe}^{3+} \rangle$	-0.047	0.337		
bio5	$[\text{Fe}^{2+}]$	1.142	2.415	87	3.7
	$[\text{Fe}^{3+}]$	0.345	0.978		
	$\langle \text{Fe}^{3+} \rangle$	-0.015	0.371		

4.5.2 Magnetic anisotropy of biotites

4.5.2.1 Low-field anisotropy of magnetic susceptibility of biotite

Table 4.4 and Figure 4.12 (black symbols) summarize the values of the low-field anisotropy of magnetic susceptibility measured in the biotite crystals. The shape determined by low-field methods is well-constrained in the oblate area of the Jelinek plot. Anisotropy degree tends to be slightly higher than the values reported in previous works.

Table 4.4: Magnitudes and directions of the low-field magnetic susceptibility of biotite crystals. The mean is evaluated as the arithmetic mean and the error is the standard variation of the data, in this and subsequent figures.

name	κ_1^{LF}	D_1^{LF}	I_1^{LF}	κ_2^{LF}	D_2^{LF}	I_2^{LF}	κ_3^{LF}	D_3^{LF}	I_3^{LF}	κ_{bulk}^{LF} [S.I.]	T^{LF}	P_j^{LF}
bio1.01	1.091	0.6	31.7	1.062	182.4	58.3	0.848	91.1	0.8	1.35×10^{-3}	0.79	1.32
bio1.02	1.127	175.0	68.5	1.079	351.8	21.4	0.794	82.2	1.1	0.98×10^{-3}	0.75	1.47
bio1.03	1.084	0.3	51.0	1.078	176.0	38.9	0.838	267.7	2.1	1.02×10^{-3}	0.95	1.34
bio1.04	1.090	189.0	82.4	1.064	357.4	7.5	0.845	87.6	1.5	1.22×10^{-3}	0.81	1.32
bio2.01	1.093	90.0	88.5	1.080	0.0	0.0	0.827	270.0	1.5	1.04×10^{-3}	0.91	1.37
bio2.02	1.092	356.1	75.1	1.083	176.0	14.9	0.825	266.0	0.0	1.10×10^{-3}	0.94	1.37
bio3.01	1.125	190.4	21.0	1.114	300.8	42.3	0.761	81.4	40.3	1.74×10^{-3}	0.95	1.56
bio4.01	1.104	180.2	29.7	1.084	10.5	59.9	0.812	272.7	4.5	0.74×10^{-3}	0.88	1.41
bio5.01	1.087	341.9	84.2	1.067	177.1	5.6	0.846	87.0	1.5	1.13×10^{-3}	0.86	1.32
bio6.01	1.084	237.0	81.4	1.073	91.2	7.2	0.844	0.6	4.8	1.10×10^{-3}	0.92	1.33
bio6.02	1.074	177.4	19.6	1.074	2.3	70.3	0.852	267.9	1.5	1.09×10^{-3}	0.99	1.31
mean	1.10			1.08			0.83			1.1×10^{-3}	0.88	1.37
	± 0.02			± 0.01			± 0.03			$\pm 0.2 \times 10^{-3}$	± 0.14	± 0.06

4.5.2.2 High-field anisotropy of biotite

Eleven samples have been measured in a high-field torque magnetometer to obtain the paramagnetic and ferromagnetic contributions to the magnetic anisotropy. The torque was found to be proportional to the square to the applied field. The second order term of the analysis of the signal is a straight line that goes through the origin in all the samples (Figure 4.11).

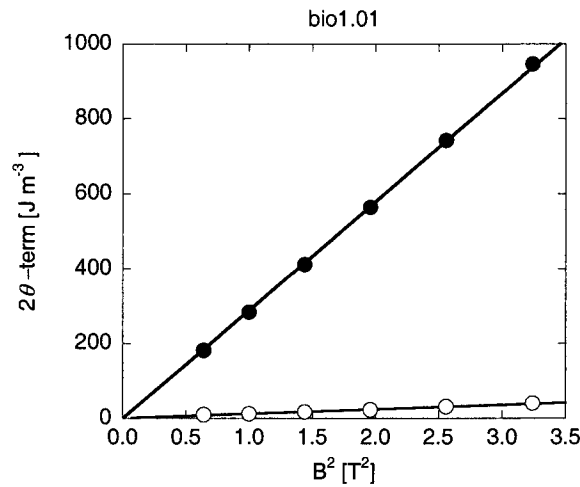


Figure 4.11: Amplitude of the 2θ -term of the torque signal as a function of B^2 for a biotite. Black symbols correspond to the cosine term and open symbol to the sinus term.

The ferromagnetic phases do not contribute significantly to the high-field anisotropy (Table 4.5), since the intercept is not statistically different from zero. Therefore the anisotropy can be considered to be due to biotite.

Table 4.5: Percentage of anisotropic paramagnetic and ferromagnetic minerals evaluated from the torque signal in biotite crystals.

name	% paramagnetic	%ferromagnetic
bio1.01	96 ± 6	4 ± 4
bio1.02	96 ± 5	4 ± 5
bio1.03	96 ± 5	4 ± 4
bio1.04	94 ± 7	6 ± 6
bio2.01	94 ± 7	6 ± 6
bio2.02	94 ± 6	6 ± 6
bio3.01	97 ± 6	3 ± 6
bio4.01	94 ± 8	6 ± 6
bio5.01	99 ± 12	1 ± 3
bio6.01	94 ± 15	6 ± 8
bio6.02	94 ± 8	6 ± 6

The anisotropy of the paramagnetic fraction was calculated in all the samples and the results are summarized in Table 4.6 and Figure 4.12 (open symbols). Since it was not possible to measure the paramagnetic susceptibility on the same sample that was measured in the torque magnetometer, a mean value was calculated with the samples

4. Magnetic properties of phyllosilicates

from the same crystal to obtain the magnitudes of the principal axes of the AMS ellipsoid.

Table 4.6: Magnitudes and directions of the paramagnetic susceptibility of biotite crystals.

name	κ_1^{para}	D_1^{para}	I_1^{para}	κ_2^{para}	D_2^{para}	I_2^{para}	κ_3^{para}	D_3^{para}	I_3^{para}	$\kappa_{\text{bulk}}^{\text{para}}$ [S.I.]	T^{para}	P_1^{para}
bio1.01	1.151	9.2	47.0	1.135	179.9	42.6	0.714	274.2	4.6	1.23×10^{-3}	0.94	1.72
bio1.02	1.162	183.8	39.1	1.143	359.0	50.8	0.695	91.9	2.3	1.23×10^{-3}	0.93	1.79
bio1.03	1.142	2.3	10.0	1.107	156.2	78.8	0.751	271.4	4.8	1.23×10^{-3}	0.85	1.60
bio1.04	1.161	156.0	71.3	1.146	356.0	17.6	0.692	264.1	6.0	1.23×10^{-3}	0.95	1.81
bio2.01	1.168	186.8	71.6	1.154	1.8	18.3	0.678	92.3	1.5	1.18×10^{-3}	0.95	1.86
bio2.02	1.167	176.2	74.9	1.155	359.2	15.1	0.678	269.0	0.7	1.18×10^{-3}	0.96	1.86
bio3.01	1.187	312.2	28.5	1.144	202.6	31.7	0.669	74.8	44.7	1.59×10^{-3}	0.87	1.90
bio4.01	1.101	1.4	29.4	1.096	172.9	60.3	0.803	269.3	3.7	1.38×10^{-3}	0.97	1.44
bio5.01	1.179	158.4	78.2	1.165	354.9	11.3	0.657	264.2	3.2	1.09×10^{-3}	0.96	1.95
bio6.01	1.173	106.8	44.2	1.164	265.4	43.8	0.663	6.0	10.9	1.12×10^{-3}	0.97	1.92
bio6.02	1.158	176.9	18.9	1.149	18.3	69.8	0.693	269.2	6.9	1.12×10^{-3}	0.97	1.80
mean	1.16			1.14			0.70			1.24×10^{-3}	0.9	1.78
	± 0.02			± 0.02			± 0.04			$\pm 0.14 \times 10^{-3}$	± 0.2	± 0.14

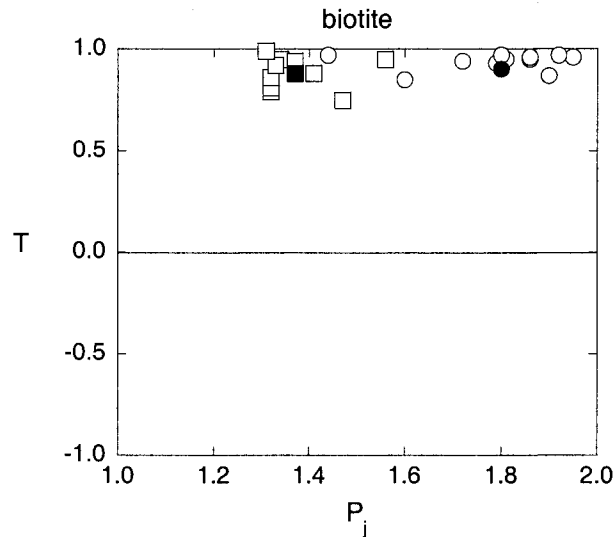


Figure 4.12: Jelinek plot of the magnetic susceptibility ellipsoid for single crystals of biotite. Squares represent values measured on the AGICO Kappabridge KLY-2. Circles represent the paramagnetic component of the susceptibility anisotropy calculated from high-field torque magnetometer measurements. Full symbols represents the para mean value. The same symbols are used in subsequent figures.

4.5.2.3 *Summary of biotite results*

Magnetite has been confirmed in all studied biotite crystals as seen from the presence of magnetite Verwey transition and/or magnetite isotropic point (Figure 4.7).

The anisotropy of the paramagnetic fraction, due to the anisotropy of the crystals alone has been found to be controlled by the crystallographic axes. The degree of flattening is high, $T = 0.9 \pm 0.2$ and anisotropy degree is also high, $P_j = 1.78 \pm 0.14$. The minimum susceptibility axis is sub-parallel to the pole to basal plane, which suggests that there is no interaction between the sheets of the crystals. Maximum and intermediate axes are contained in the basal plane. The orientation of maximum and intermediate axes of susceptibility with respect to the crystallographic axes in the basal plane could not be established within the accuracy of the measurements. However, the measurements done within the basal plane suggest that the susceptibility is isotropic.

The bulk susceptibility of phyllosilicates has been found to be dependent on the iron content, and a similar dependence is found between the anisotropy degree and Fe^{2+}/Fe^{3+} ratio (Table 4.6 and Table 4.3). This correspondence confirms the validity of the formula for the susceptibility given by Rochette et al. (1992).

4.6 Muscovite

4.6.1 *Rock magnetic properties of muscovite*

4.6.1.1 *IRM acquisition curve*

IRM acquisition curves have been done on one specimen of each crystal of muscovite. The curve reveals the presence of a low coercivity phase that starts to acquire magnetization at very low coercivities. An additional higher coercivity phase does not saturate at 1 T (Figure 4.13). The presence of pseudo-single domain magnetite in muscovite has been reported by Borradaile and Werner (1994) but there was no evidence of a high coercivity phase in any previous study.

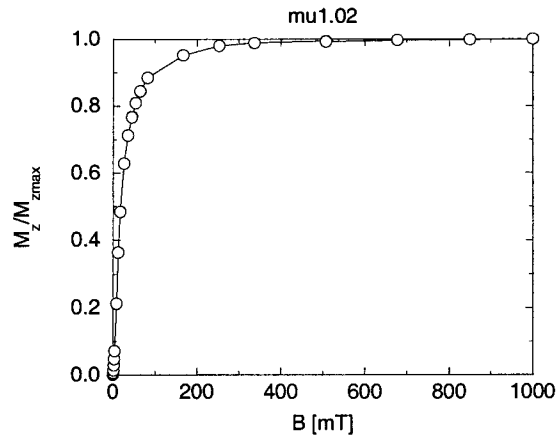


Figure 4.13: IRM acquisition curve in a muscovite crystal. The field is applied in a direction contained in the basal plane.

4.6.1.2 Magnetization at low temperatures

For low temperature experiments a saturating field of 2.5 T was applied to the sample. The sample was cooled down to 50 K in a zero-field and subsequently warmed up to room temperature under the same conditions with measurements taken every 5 K. The sample exhibits a drop in magnetization upon cooling between 105 K and 130 K. Since the magnetization is not recovered when warming above 130 K, the loss of magnetization would occur at the magnetite isotropic point (Muxworthy, 1999). This behavior suggests pure magnetite is present in the sample.

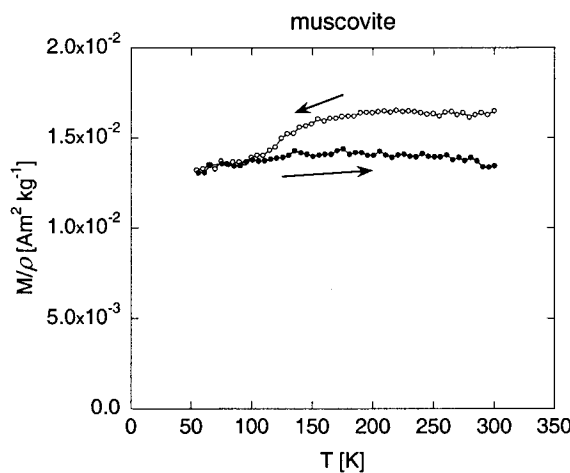


Figure 4.14: Low temperature remanence experiments in a muscovite crystal. Open symbols correspond to the cooling curve and black symbols to the warming curve.

4.6.2 Magnetic anisotropy of muscovite mica

4.6.2.1 Low field anisotropy of magnetic susceptibility of muscovite

Table 4.7 and Figure 4.16 (black symbols) summarize the values of the low-field anisotropy of magnetic susceptibility of the crystals used in this work. The dispersion of the data is high, especially for crystal mu1. The dark gray color of the sample suggests the possibility of a high concentration of ferromagnetic impurities this is further supported by the mean susceptibility of $2.7 \times 10^{-4} \pm 1.1 \times 10^{-4}$ [S.I.] in contrast with the value of 1.65×10^{-4} [S.I.] reported by Borradaile and Werner (1994).

Table 4.7: Magnitudes and directions of the low-field magnetic susceptibility of muscovite.

name	κ_1^{LF}	D_1^{LF}	I_1^{LF}	κ_1^{LF}	D_2^{LF}	I_2^{LF}	κ_1^{LF}	D_3^{LF}	I_3^{LF}	κ_{bulk}^{LF} [S.I.]	T^{LF}	P_j^{LF}
mu1.01	1.334	334.6	1.9	1.092	242.8	44.2	0.575	66.6	45.8	0.402×10^{-3}	0.52	2.41
mu1.02	1.457	356.7	11.2	1.320	183.1	78.7	0.223	86.9	1.2	1.126×10^{-3}	0.89	8.30
mu1.03	1.304	171.2	63.5	1.130	355.3	26.5	0.566	264.5	1.7	0.306×10^{-3}	0.66	2.44
mu2.01	1.092	3.0	32.1	1.055	176.6	57.7	0.853	271.2	2.9	0.077×10^{-3}	0.72	1.31
mu2.02	1.121	104.4	79.8	1.009	348.1	4.6	0.869	257.3	9.1	0.079×10^{-3}	0.17	1.29
mu2.03	1.125	338.1	80.3	1.061	180.7	9.0	0.814	90.1	3.7	0.065×10^{-3}	0.64	1.41
mu3.01	1.122	180.8	56.3	1.074	0.1	33.7	0.804	90.3	0.3	0.118×10^{-3}	0.73	1.44
mu3.02	1.106	106.4	84.6	1.068	357.5	1.8	0.825	267.3	5.1	0.116×10^{-3}	0.76	1.38
mu3.03	1.111	202.8	85.2	1.079	0.4	4.5	0.810	90.5	1.8	0.115×10^{-3}	0.81	1.42
mean	1.20			1.10			0.7			0.27×10^{-3}	0.7	1.8
	± 0.13			± 0.09			± 0.2			$\pm 0.11 \times 10^{-3}$	± 0.5	± 0.6

4.6.2.2 High-field anisotropy of muscovite

The nine samples have been measured with a high-field torque magnetometer. The mu1 samples have a statistically not significant ferromagnetic fraction, represented by a zero intercept of the line that fits the 2θ -term of the Fourier analysis as a function of the square of applied field (Figure 4.15a and Table 4.8). In other samples the intercept of the fitting is different from zero, therefore the ferromagnetic fraction can be considered statistically significant (Figure 4.15b).

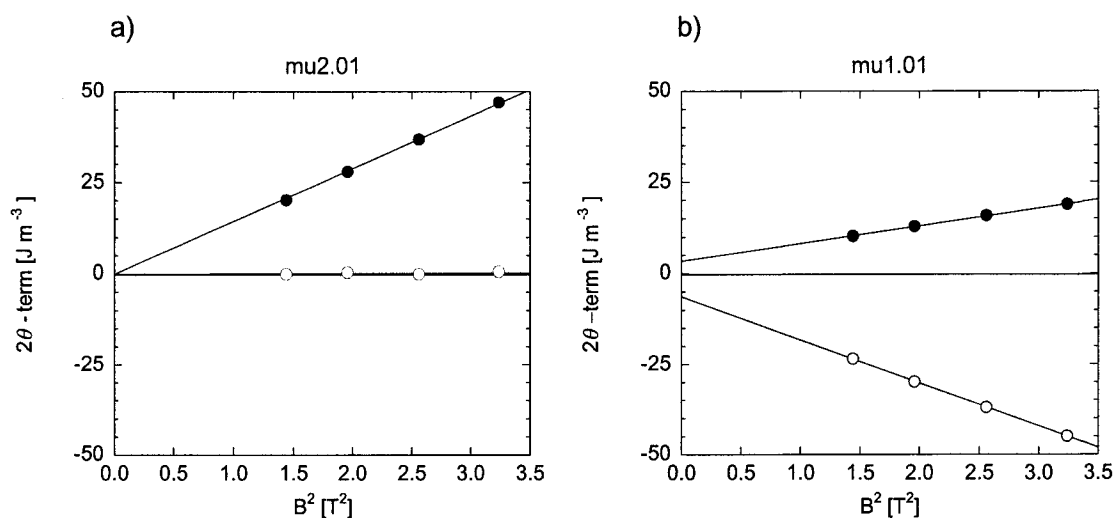


Figure 4.15: Amplitude of the 2θ -term of the torque signal as a function of B^2 for two muscovite crystals. a) sample without a statistically significant ferromagnetic fraction and b) sample with statistically significant ferromagnetic fraction.

Table 4.8: Percentage of anisotropic paramagnetic and ferromagnetic minerals evaluated from the torque signal in muscovite crystals.

name	% paramagnetic	%ferromagnetic
mu1.01	57 ± 11	43 ± 14
mu1.02	26 ± 10	74 ± 27
mu1.03	63 ± 12	38 ± 12
mu2.01	92 ± 9	8 ± 10
mu2.02	95 ± 10	5 ± 6
mu2.03	89 ± 10	11 ± 30
mu3.01	94 ± 8	6 ± 6
mu3.02	94 ± 6	6 ± 6
mu3.03	94 ± 5	6 ± 6

Table 4.9 presents the values of the paramagnetic component of the magnetic anisotropy obtained from the high-field measurements. All the paramagnetic ellipsoids show an oblate shape with a fairly homogeneous value of the anisotropy degree, after the separation from the ferromagnetic tensor. The values are well-grouped in the oblate shape zone of the Jelinek plot with a mean anisotropy degree of $P_j = 1.29$ (Figure 4.16, open symbols).

4. Magnetic properties of phyllosilicates

Table 4.9: Magnitude and directions of the paramagnetic susceptibility of muscovite.

name	κ_1^{para}	D_1^{para}	I_1^{para}	κ_2^{para}	D_2^{para}	I_2^{para}	κ_3^{para}	D_3^{para}	I_3^{para}	$\kappa_{\text{bulk}}^{\text{para}}$ [S.I.]	T^{para}	P_i^{para}
mu1.01	1.095	307.7	23.7	1.068	197.8	37.7	0.837	61.7	43.0	2.41×10^{-4}	0.82	1.35
mu1.02	1.136	161.3	65.4	1.109	1.1	23.3	0.755	267.9	7.4	2.41×10^{-4}	0.88	1.58
mu1.03	1.086	176.6	4.7	1.059	26.1	84.7	0.855	266.8	2.6	2.41×10^{-4}	0.79	1.30
mu2.01	1.042	358.2	25.2	1.029	190.8	64.2	0.929	90.6	4.9	3.44×10^{-4}	0.79	1.13
mu2.02	1.043	355.4	57.5	1.025	189.9	31.7	0.932	95.8	6.6	3.44×10^{-4}	0.69	1.13
mu2.03	1.038	184.9	33.5	1.029	4.1	56.5	0.933	94.7	0.4	3.44×10^{-4}	0.85	1.13
mu3.01	1.087	357.8	77.7	1.071	179.7	12.3	0.842	89.7	0.4	2.79×10^{-4}	0.89	1.33
mu3.02	1.084	1.5	15.7	1.077	171.4	74.1	0.839	270.7	2.6	2.79×10^{-4}	0.95	1.34
mu3.03	1.090	38.3	89.3	1.073	179.7	0.5	0.837	269.7	0.4	2.79×10^{-4}	0.88	1.35
mean	1.08			1.06			0.87			2.88×10^{-4}	0.8	1.28
	± 0.03			± 0.03			± 0.06			$\pm 0.15 \times 10^{-4}$	± 0.3	± 0.10

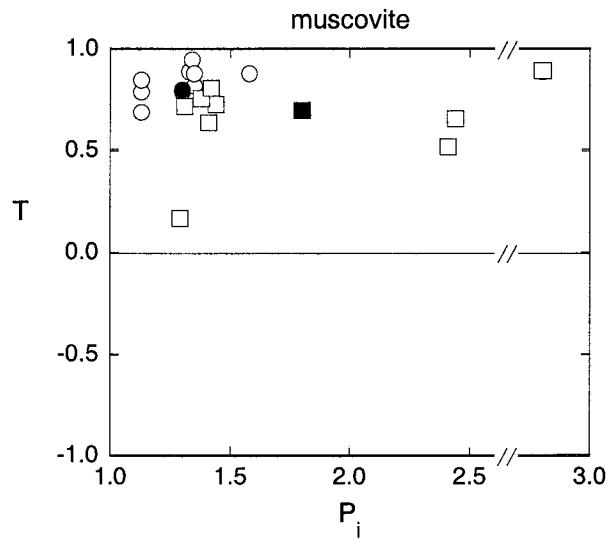


Figure 4.16: Jelinek plot of the magnetic susceptibility for muscovite single crystals.

The differences between low-field and high-field methods are due to the ferrimagnetic component that contributes to the low-field AMS. Figure 4.17 illustrates the effectiveness of the separation method. Figure 4.17a presents the principal axes for the paramagnetic component, the ferrimagnetic component and the low-field measurement. The three ellipsoids agree in their directions and the oblate shape. The low-field measurement, however, shows an exceptionally high degree of anisotropy (Table 4.7). This is due to the ferrimagnetic contribution to the low-field AMS properties of the crystal itself. The U parameter of the three fabrics is displayed in Figure 4.17. This parameter is analogous to the T shape parameter but can be applied to deviatoric tensors (Jelinek, 1981). Mathematically it is defined as:

$$U = \frac{2f_2 - f_1 - f_3}{f_1 - f_3} \quad (4.2)$$

where f_i are the principal values of the ferromagnetic anisotropy tensor. The same parameter can be calculated for the paramagnetic susceptibility tensor.

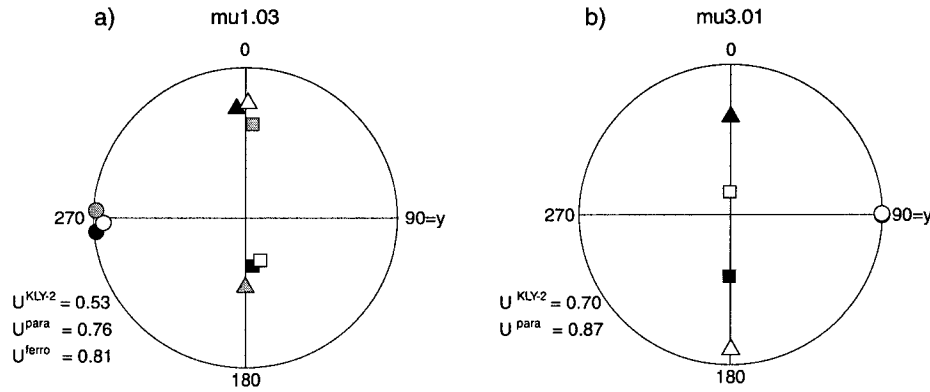


Figure 4.17: Directions of the principal axes of the susceptibility ellipsoid for two muscovite samples; a) mu1.03 with a significant ferromagnetic component and b) mu3.01 with no significant ferromagnetic component. Squares represent maximum axes, triangles represent intermediate axes and circles represent minimum axes of the susceptibility ellipsoid in this and subsequent figures. Opens symbols show the directions for the paramagnetic fabric, gray symbols represent the ferrimagnetic fabric and black symbols the low-field magnetic susceptibility principal axes.

Table 4.10 shows the ferrimagnetic tensor of anisotropy for those muscovite samples where it was found to be statistically significant.

Table 4.10: High-field ferromagnetic tensor for the analyzed muscovite crystals where N/S means an statistically not significant value of the ferromagnetic anisotropy tensor, in this and subsequent tables.

name	f_1^{ferro}	D_1^{ferro}	l_1^{ferro}	f_2^{ferro}	D_2^{ferro}	l_2^{ferro}	f_3^{ferro}	D_3^{ferro}	l_3^{ferro}	U^{ferro}
mu1.01	1.87×10^{-5}	271.1	44.4	1.03×10^{-5}	168.4	12.7	-2.89×10^{-5}	66.3	42.9	0.65
mu1.02	8.32×10^{-5}	168.6	80.4	8.07×10^{-5}	353.7	9.6	-16.40×10^{-5}	263.5	0.8	0.98
mu1.03	1.25×10^{-5}	4.3	37.1	0.93×10^{-5}	180.3	52.9	-2.18×10^{-5}	272.9	2.0	0.81
mu2.01	N/S			N/S			N/S			
mu2.02	N/S			N/S			N/S			
mu2.03	N/S			N/S			N/S			
mu3.01	N/S			N/S			N/S			
mu3.02	N/S			N/S			N/S			
mu3.03	N/S			N/S			N/S			

4.6.2.3 *Summary of muscovite results*

The low intensity of the hysteresis loops measured in muscovite samples make it impossible to analyze the anisotropy of muscovite within the basal plane. Therefore it is not possible to determine whether the minimum susceptibility axis is sub-parallel to the pole to basal plane or to the optical axes. The principal axes of the paramagnetic AMS ellipsoid are close enough to the crystallographic axes that it is possible to say that they control the magnetic anisotropy of muscovite.

Some of the samples presented a significant contribution of the ferromagnetic fraction to the AMS, but a relationship between the orientation of the anisotropy of ferromagnetic minerals with respect to the crystal.

The anisotropy degree found is $P_j = 1.28 \pm 0.10$, in the same order than previously reported values. The magnetic ellipsoid found is more oblate than values in the literature, with a shape parameter $T = 0.85 \pm 0.3$.

4.7 Chlorites

4.7.1 *Rock magnetic properties of chlorite*

4.7.1.1 *IRM acquisition curve*

The IRM acquisition curve of a chlorite crystal in the present study reveals the presence of a low coercivity phase that almost saturates at 300 mT; it is most likely magnetite. The study done by Borradaile and Werner (1994) shows a ferromagnetic phase in chlorites that is compatible with pseudo-single domain magnetite or multi-domain magnetite. A second phase with a higher coercivity may also be present in the chlorite sample. The presence of hematite in chlorite samples has been reported previously from high-field torque magnetometer analysis (Parry, 1971).

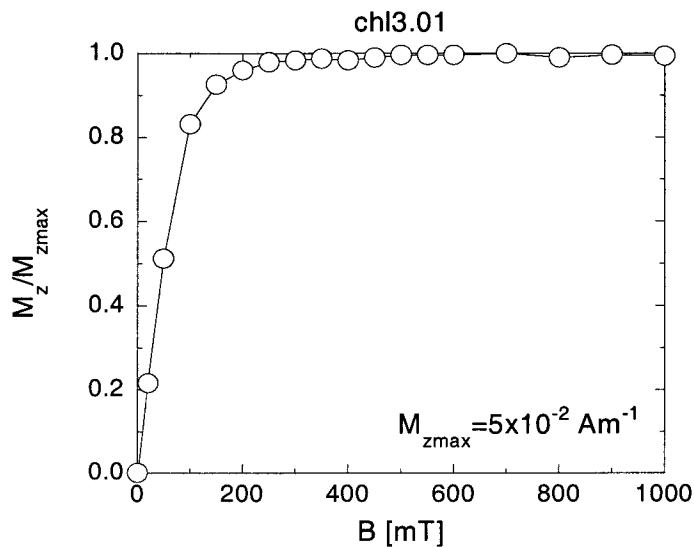


Figure 4.18: IRM acquisition curve in a chlorite crystal. The field is applied in a direction contained in the basal plane.

4.7.2 Magnetic anisotropy of chlorite

4.7.2.1 Low-field anisotropy of magnetic susceptibility of chlorite

The low-field magnetic anisotropy results are given in Table 4.11 and in Figure 4.20 (black symbols). In the calculations of mean values, sample ch12.02 has been excluded because of its high value of the bulk susceptibility. The dispersion in the degree of anisotropy and the shape parameter is high, as is the bulk susceptibility of chlorite. The average value of 1.1507×10^{-3} [S.I.] is higher than the value of 0.551×10^{-3} [S.I.] reported by Borradaile and Werner (1994). This suggests that there may be ferromagnetic impurities in the analyzed samples. The values of the T parameters do not agree with the expected oblate shape of AMS ellipsoid that should arise from the phyllosilicate crystal structure.

Table 4.11: Magnitudes and directions of the low-field magnetic susceptibility of chlorite..

name	κ_1^{LF}	D_1^{LF}	I_1^{LF}	κ_2^{LF}	D_2^{LF}	I_2^{LF}	κ_3^{LF}	D_3^{LF}	I_3^{LF}	κ_{bulk}^{LF} [S.I]	T^{LF}	P_j^{LF}
chl1.01	1.052	352.8	1.2	1.033	224.9	88.1	0.914	82.8	1.5	0.210×10^{-3}	0.74	1.17
chl1.02	1.042	177.3	28.1	1.028	352.9	61.9	0.930	86.3	1.8	0.237×10^{-3}	0.77	1.13
chl1.03	1.040	352.4	17.1	1.033	162.3	72.6	0.927	261.5	2.9	0.214×10^{-3}	0.89	1.14
chl2.01	1.303	301.1	5.4	0.986	31.3	1.9	0.711	140.4	84.2	1.389×10^{-3}	0.08	1.83
chl2.02	1.518	161.5	2.2	1.008	252.1	15.0	0.475	63.3	74.9	11.579×10^{-3}	0.30	3.25
chl3.01	1.044	176.0	21.2	1.040	358.1	68.8	0.916	266.3	0.7	0.242×10^{-3}	0.94	1.16
chl4.01	1.180	0.1	8.9	1.068	180.8	81.1	0.753	90.1	0.1	1.876×10^{-3}	0.56	1.60
chl4.02	1.185	345.7	86.4	1.036	179.8	3.5	0.779	89.7	0.9	1.495×10^{-3}	0.36	1.53
chl4.03	1.253	176.9	5.7	1.054	28.4	83.3	0.693	267.2	3.5	2.309×10^{-3}	0.42	1.84
chl5.01	1.524	219.5	3.1	0.893	128.2	22.5	0.583	316.9	67.2	3.122×10^{-3}	-0.11	2.62
chl5.02	1.142	31.5	59.7	1.014	182.6	27.1	0.844	279.1	12.5	0.413×10^{-3}	0.21	1.36
mean	1.21			1.02			0.77			1.1×10^{-3}	0.2	1.6
	± 0.18			± 0.05			± 0.15			$\pm 0.1 \times 10^{-3}$	± 0.6	± 0.4

4.7.2.2 High-field anisotropy of chlorite

The samples have been measured with a high field torque magnetometer in four fields high enough to saturate the ferrimagnetic component. Some samples presented a non-significant ferromagnetic fraction (Figure 4.19a), while others show a statistically significant contribution of the ferromagnetic minerals to the torque signal (Figure 4.19b).

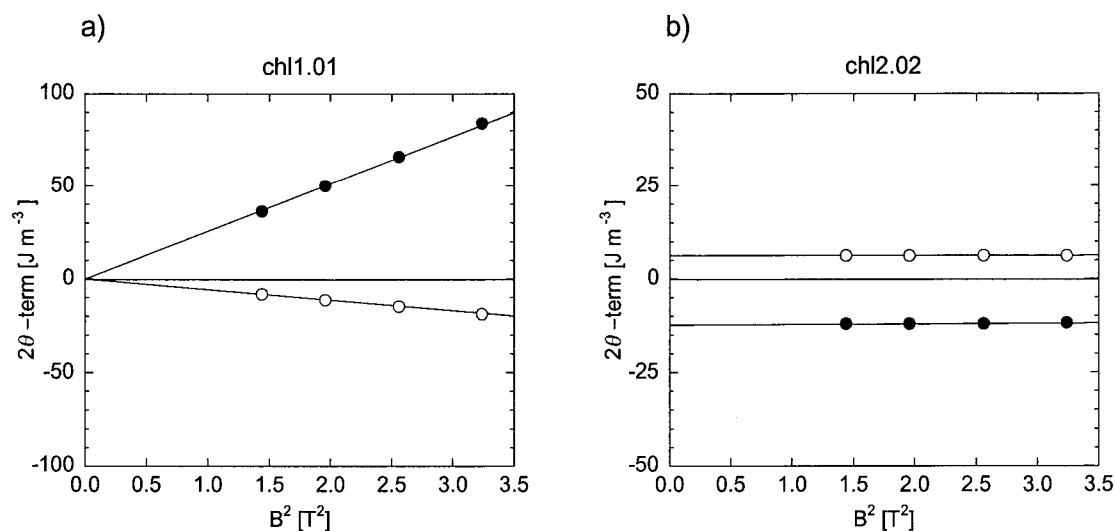


Figure 4.19: Amplitude of the 2θ -term of the torque signal as a function of B^2 for chlorite crystals. a) sample without statistically significant ferromagnetic fraction and b) sample with a statistically significant ferromagnetic fraction.

4. Magnetic properties of phyllosilicates

The analysis of the torque measurements reveals the ratio of anisotropic paramagnetic and ferromagnetic minerals to the torque signal summarized in Table 4.12. Crystals 2 and 5 show a significant ferromagnetic contribution.

Table 4.12: Percentage of anisotropic paramagnetic and ferromagnetic minerals from the torque signal in chlorite crystals.

name	% paramagnetic	%ferromagnetic
chl1.01	94 ± 9	5 ± 7
chl1.02	94 ± 6	6 ± 6
chl1.03	94 ± 11	6 ± 8
chl2.01	62 ± 3	38 ± 4
chl2.02	12 ± 1	88 ± 15
chl3.01	94 ± 10	6 ± 6
chl4.01	97 ± 8	3 ± 6
chl4.02	94 ± 9	5 ± 7
chl4.03	94 ± 9	5 ± 7
chl5.01	31 ± 3	69 ± 10
chl5.02	90 ± 9	10 ± 8

The values obtained for the paramagnetic component of the anisotropy of the susceptibility of the crystals are summarized in Table 4.13. The average susceptibility is closer to the expected value for chlorite, and the shape of the susceptibility ellipsoid is oblate as expected.

Table 4.13: Magnitude and directions of the paramagnetic susceptibility of chlorite.

name	K_1^{para}	D_1^{para}	I_1^{para}	K_2^{para}	D_2^{para}	I_2^{para}	K_3^{para}	D_3^{para}	I_3^{para}	K_{bulk}^{para} [S.I.]	T^{para}	P_j^{para}
chl1.01	1.090	358.2	8.3	1.079	181.4	81.7	0.831	88.2	0.5	0.226×10^{-3}	0.92	1.36
chl1.02	1.070	353.1	29.1	1.059	176.5	60.9	0.872	83.9	1.4	0.275×10^{-3}	0.90	1.26
chl1.03	1.069	172.3	2.6	1.058	46.9	85.4	0.874	262.5	3.7	0.275×10^{-3}	0.89	1.26
chl2.01	1.063	14.1	75.7	1.062	180.4	13.9	0.875	271.2	3.2	0.316×10^{-3}	0.99	1.25
chl2.02	1.070	171.2	60.4	1.054	1.7	29.2	0.875	269.2	4.5	0.316×10^{-3}	0.85	1.25
chl3.01	1.118	192.1	71.5	1.117	356.8	17.9	0.765	88.2	4.6	0.195×10^{-3}	1.00	1.55
chl4.01	1.075	39.8	85.3	1.074	180.2	3.6	0.851	270.4	3.0	3.260×10^{-3}	0.99	1.31
chl4.02	1.074	350.0	29.1	1.071	175.8	60.7	0.855	81.4	2.5	3.260×10^{-3}	0.97	1.30
chl4.03	1.071	175.6	27.9	1.067	358.7	62.0	0.861	266.3	1.3	3.260×10^{-3}	0.96	1.28
chl5.01	0.928	12.0	32.3	0.925	167.4	55.1	0.706	274.5	11.6	0.245×10^{-3}	0.98	1.37
chl5.02	0.928	176.0	65.7	0.925	353.3	24.2	0.706	83.8	1.0	0.245×10^{-3}	0.98	1.37
mean	1.05 ± 0.06			1.05 ± 0.06			0.82 ± 0.07			1.1×10^{-3} $\pm 1.0 \times 10^{-3}$	1.0 ± 0.7	1.3 ± 0.1

Figure 4.20 shows the shape and degree of anisotropy of the paramagnetic susceptibility ellipsoids and their mean value. The shapes of the AMS ellipsoid

measured with the torque magnetometer are well constrained as compared with the dispersed values measured with the KLY-2.

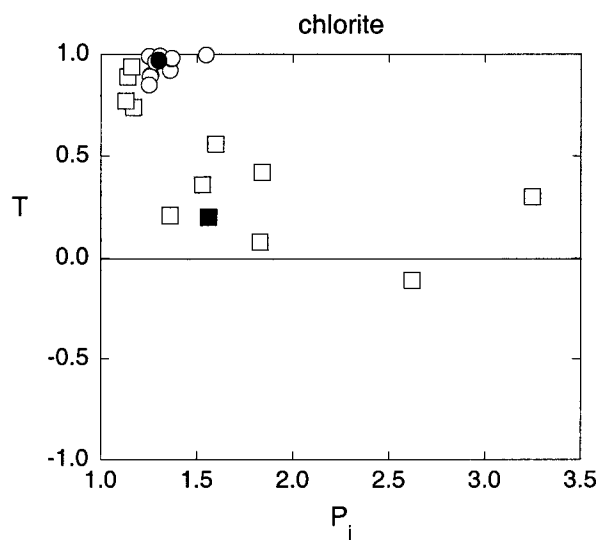


Figure 4.20: Jelinek plot of the magnetic susceptibility ellipsoid for chlorite single crystals.

Figure 4.21 shows an example that compares orientation of the principal axes from low-field and high-field measurements. The minimum axis of the paramagnetic susceptibility is sub-parallel to the crystal c-axis (Figure 4.21a). The direction of the minimum axis of the ferrimagnetic fraction agrees with the low-field magnetic susceptibility in chl2.01 (Figure 4.21a). This suggests that the ferrimagnetic fraction controls the low-field magnetic susceptibility in samples that have a significant ferrimagnetic component. At low-fields the susceptibility ellipsoid has slightly prolate shape that results from the overlapping of two oblate fabrics that are orthogonal to each other. In the purer crystals, the ferromagnetic phase does not contribute significantly to the magnetic anisotropy (Table 4.12). Therefore there is a very good agreement between axial directions of the low-field susceptibility ellipsoid and the paramagnetic ellipsoid and their shapes (Figure 4.21b).

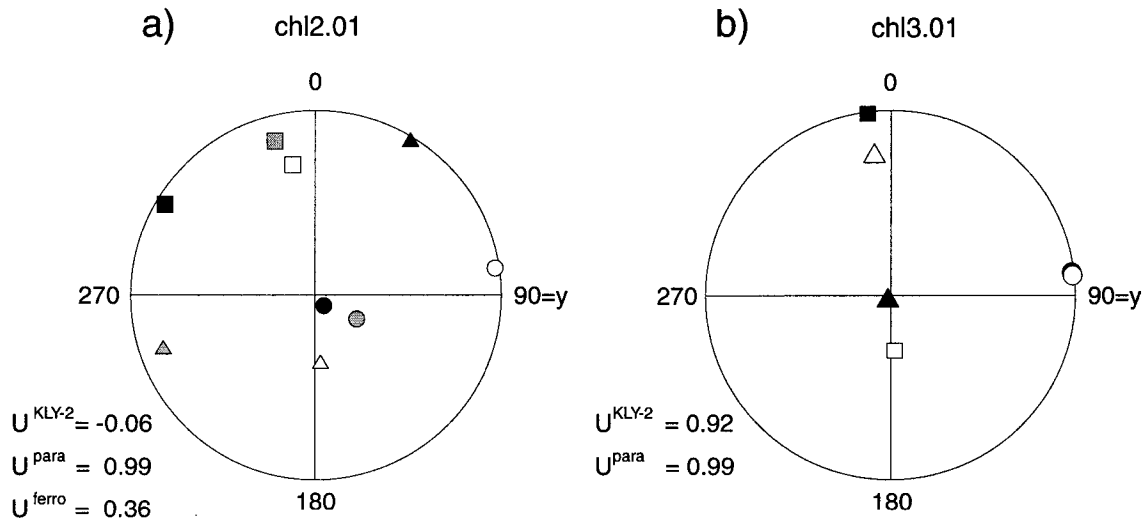


Figure 4.21: Magnetic susceptibility directions for a chlorite sample. Open symbols show the directions for the paramagnetic fabric, gray symbols represent the ferrimagnetic fabric and black symbols the low field magnetic susceptibility measured with the Kappabridge.

Table 4.14 summarized the main parameters of the ferrimagnetic tensor of chlorites in the samples where a statistically significant contribution is made to the high-field torque signal.

Table 4.14: High field ferromagnetic tensor of chlorite crystals and the U shape.

name	f_1^{ferro}	D_1^{ferro}	I_1^{ferro}	f_2^{ferro}	D_2^{ferro}	I_2^{ferro}	f_3^{ferro}	D_3^{ferro}	I_3^{ferro}	U^{ferro}
chl1.01	N/S			N/S			N/S			
chl1.02	N/S			N/S			N/S			
chl1.03	N/S			N/S			N/S			
chl2.01	1.84×10^{-5}	43.2	5.6	4.97×10^{-6}	312.0	12.1	-2.34×10^{-5}	157.7	76.6	0.36
chl2.02	1.86×10^{-4}	345.2	14.9	1.08×10^{-4}	251.3	14.3	-2.94×10^{-4}	119.6	69.1	0.68
chl3.01	N/S			N/S			N/S			
chl4.01	N/S			N/S			N/S			
chl4.02	N/S			N/S			N/S			
chl4.03	N/S			N/S			N/S			
chl5.01	6.99×10^{-5}	40.5	10.0	-3.52×10^{-6}	310.0	3.0	-6.64×10^{-5}	203.3	79.6	-0.08
chl5.02	4.08×10^{-6}	56.2	48.2	-1.02×10^{-6}	192.0	32.6	-3.06×10^{-6}	297.8	23.0	-0.43

4.7.2.3 Summary of chlorite results

The κ_3 axes of the paramagnetic fraction in chlorite crystals has been found to lie sub-parallel to the crystallographic c-axis. The anisotropy in the basal plane was not

evaluated because it was not possible to obtain a flat surface to mount in the VSM holder. The AMS measured at low-fields showed in some samples extremely high degrees of anisotropy and prolate anisotropy ellipsoids not oriented in the crystallographic axes of the chlorite. The separation of the magnetic components allows the evaluation of the paramagnetic anisotropy where the shape parameter was very oblate with $T = 1.0 \pm 0.7$ and the anisotropy degree $P_j = 1.3 \pm 0.1$.

4.8 Discussion

The AMS of phyllosilicates presented here are based on the method of separation of the paramagnetic component to the anisotropy from measurements with a high-field torque magnetometer. The orientation of the principal axes and shape of the anisotropy ellipsoid obtained values are consistent with the crystallographic structure of phyllosilicates. To confirm the accuracy of the torque measurements they were compared with susceptibility differences obtained from hysteresis curves. Table 4.15 summarizes the comparison of the two methods for all the analyzed phyllosilicates.

Table 4.15: Differences of the paramagnetic susceptibility values in the basal plane ($\kappa_{||}$) and perpendicular to it (κ_{\perp}) with two different instruments for all the analyzed crystals. Susceptibility values are expressed in [S.I.] units.

biotite	$(\kappa_{ }-\kappa_{\perp})^{\text{VSM}}$	$(\kappa_1-\kappa_3)^{\text{tor}}$	muscovite	$(\kappa_{ }-\kappa_{\perp})^{\text{VSM}}$	$(\kappa_{ }-\kappa_{\perp})^{\text{tor}}$	chlorite	$(\kappa_{ }-\kappa_{\perp})^{\text{VSM}}$	$(\kappa_{ }-\kappa_{\perp})^{\text{tor}}$
bio1.01	4.91×10^{-4}	5.38×10^{-4}	mu1.01	4.72×10^{-5}	6.21×10^{-5}	chl1.01	5.00×10^{-5}	5.86×10^{-5}
bio1.02	3.99×10^{-4}	5.76×10^{-4}	mu1.02	5.22×10^{-5}	9.17×10^{-5}	chl1.02	7.33×10^{-5}	5.44×10^{-5}
bio1.03	2.72×10^{-4}	4.82×10^{-4}	mu1.03	4.34×10^{-5}	5.58×10^{-5}	chl1.03	8.59×10^{-5}	5.37×10^{-5}
bio1.04	2.72×10^{-4}	5.79×10^{-4}	mu2.01	3.56×10^{-5}	3.87×10^{-5}	chl2.01	1.01×10^{-4}	5.92×10^{-5}
bio2.01	4.19×10^{-4}	5.77×10^{-4}	mu2.02	3.50×10^{-5}	3.82×10^{-5}	chl2.02	8.27×10^{-5}	6.18×10^{-5}
bio3.01	4.59×10^{-4}	5.76×10^{-4}	mu2.03	4.76×10^{-5}	3.60×10^{-5}	chl3.01	7.94×10^{-5}	6.89×10^{-5}
bio4.01	3.44×10^{-4}	8.25×10^{-4}	mu3.01	4.51×10^{-5}	6.82×10^{-5}	chl4.01	2.30×10^{-4}	7.29×10^{-4}
bio4.02	2.97×10^{-4}	4.10×10^{-4}	mu3.02	5.58×10^{-5}	6.83×10^{-5}	chl4.02	2.41×10^{-4}	7.14×10^{-4}
bio5.01	4.93×10^{-4}	5.70×10^{-4}	mu3.03	5.41×10^{-5}	7.07×10^{-5}	chl5.01	5.07×10^{-4}	6.85×10^{-4}
bio6.01	5.28×10^{-4}	5.74×10^{-4}				chl6.01	8.02×10^{-5}	5.45×10^{-5}
bio6.02	4.74×10^{-4}	5.23×10^{-4}				chl6.02	8.02×10^{-5}	5.88×10^{-5}

Figure 4.22 shows a graphic representation of the two different methods. The differences in results obtained by the two methods are uniform for all samples.

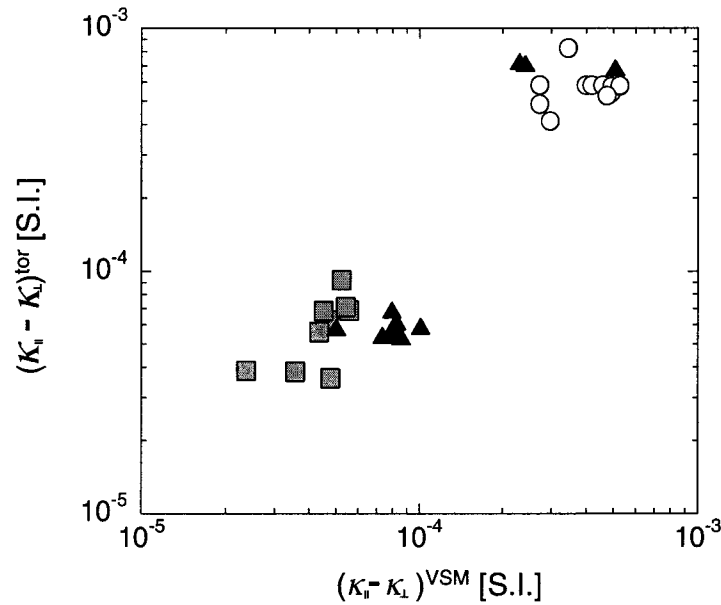


Figure 4.22: Relationship between the difference of magnetic susceptibility in the basal plane and perpendicular to it measured with two different methods. Open circles denote measurements done in biotite, squares in muscovite and triangles in chlorite.

The advantage of using the high-field torque magnetometer is that the measurement procedure does not require that the samples are measured along assumed principal axes. Therefore it is not necessary to know the orientation of the crystallographic axes of the crystal. The procedure also gives an estimate of the error of the measurement. A comparison between the values obtained from this study and those reported in previous works are shown in Figure 4.23. The data of the present study reflect the sheet structure of the crystals, where Fe cations lie in planes.

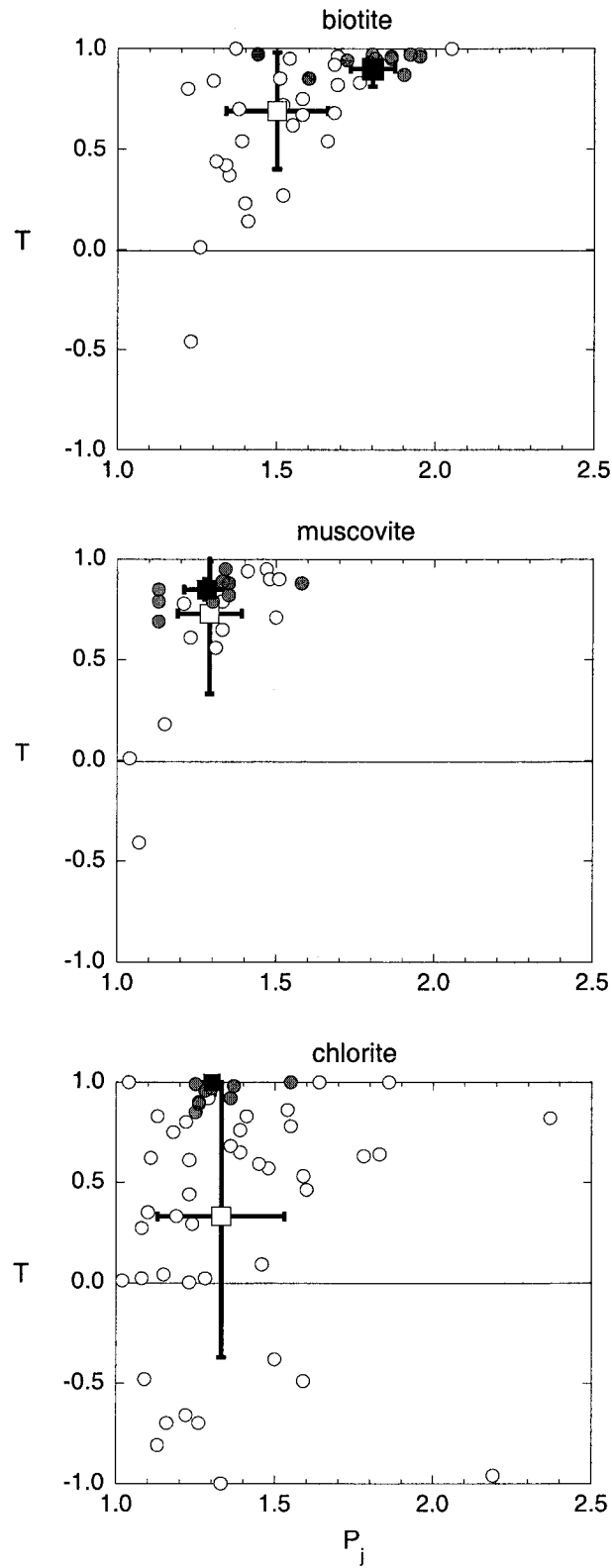


Figure 4.23: Jelinek plot showing the magnetic anisotropy of the studied phyllosilicates. Grey symbols represent the data measured in this work and open symbols data from Borradaile and Werner (1994). Squares represent the mean values for the two sets of measurements with their standard deviation.

4.9 Conclusions

The results presented in this work have two advantages over results previously reported in the literature. Firstly, the values were obtained by separation of the paramagnetic component of the crystals from the ferromagnetic component of the impurities. This provides a more accurate value with respect to low-field methods that measure all the components in the crystal (Borradaile et al., 1987; Zapletal, 1990).

Previous studies have shown that the bulk susceptibility is dependent on the content of iron and manganese in the crystals. The Mössbauer measurements in this study show that the main magnetic anisotropy parameters of biotite single crystals are governed by the cation content. The anisotropy degree is therefore a magnetic parameter that depends on the cation content because of its direct relation with the bulk susceptibility. The variation in the degree of anisotropy seems to be related to the cation content.

Of the measured crystals, chlorite is the one with greatest ferromagnetic contribution of the AMS. The analysis of the ferromagnetic signal does not allow definitive conclusions about the relationship between the crystallographic axes and the magnetic orientation of the ferromagnetic minerals. The dominant axis of the ferromagnetic component tends to lie either perpendicular to the basal plane of the crystal or parallel. A more detailed analysis of the magnetic parameter of the inclusions would be needed to establish the spatial configuration of the particles within the crystal.

The presence of the ferromagnetic inclusions has been shown to be as the main source of scatter in the parameters use to describe the AMS ellipsoid (Borradaile and Werner, 1994; Lagroix and Borradaile, 2000). In low-field measurements they can mask the paramagnetic anisotropy of the crystals. It should be noted that the presence of ferrimagnetic inclusions does not necessary contribute to the AMS. It does contribute, however, to the bulk susceptibility. Therefore the orientation of the principal axes may not be affected by a ferrimagnetic fraction if this is isotropically distributed. The magnitude of the principal axes will be affected instead.

5. Fabric analysis

In samples with magnetic anisotropy carried by phyllosilicates, the preferred orientation of the pole to basal plane of phyllosilicates governs mostly the AMS. The analysis of the magnetic fabric of these rocks is a useful indicator of different stages of deformation the rocks have undergone. To enrich our knowledge of the mechanisms by which these deformations are registered an extensive analysis on slates with different deformation stages has been made. The study comprises sites with slaty cleavage alone, slaty cleavage with stretching lineation, crenulation cleavage and a progressive deformation from kink bands to slaty cleavage at the outcrop scale. An excellent correlation has been found between the fabric of phyllosilicates determined by texture goniometry and AMS, with regard to both to their principal orientations and their ellipsoidal shapes. The analysed samples are slates from the Luarca formation, in the Ibero-Asturian Arc, northern Spain. The heterogeneity found in the texture of the samples with a well-defined slaty cleavage along the slate belt suggests that the arc did not form by tectonic bending.

Seite Leer /
Blank leaf

5.1 Introduction

One of the oldest aspects of structural geology is the description and analysis of deformational fabrics. An excellent review of all the techniques used for fabric analysis can be found in Ramsay and Huber (1983) and (1987). The use of anisotropy of magnetic susceptibility (AMS) as a qualitative recorder of deformation in rocks has become well established since the first studies of magnetic anisotropy (Graham, 1954; Fuller, 1963). In some cases it has been possible to correlate the magnitude of anisotropy of the susceptibility ellipsoid with the finite strain determined by direct methods, e.g., deformation of ooids (Kligfield et al., 1981) or analysis of concretions (Hirt et al., 1988). Some authors have found a relation between differences in the principal semiaxes of the strain ellipsoid and the differences in the magnetic susceptibility ellipsoid semiaxes (Hrouda, 1979). In other studies, the individual strain semiaxes are found to be proportional to the magnetic susceptibility semiaxes (e.g., Kligfield et al., 1981; Hirt et al., 1988). Quantitative correlation fails in cases of recrystallization of paramagnetic minerals, although the AMS still shows preferred directions related to the principal axes of strain that can exist in the samples.

In some cases, the absence of strain markers or rare abundance makes it difficult to analyse deformation. The use of magnetic anisotropy as proxy has turned out to be an excellent tool (e.g., Hirt et al., 2000). For this reason it is important to understand the deformation that causes a magnetic fabric in a rock and what the limits of this technique are. Numerous studies have examined the case of magnetic anisotropy that is carried by ferromagnetic minerals (Fuller, 1963; Uyeda et al., 1963; Tarling and Hrouda, 1993). Less is known about magnetic anisotropy due to paramagnetic minerals and about the processes that lead to a paramagnetic fabric. In particular, phyllosilicates are common rock forming minerals and are responsible for the magnetic anisotropy of many rocks, e.g., slates, shales or schists. It is known that in these types of rocks the anisotropy often arises from the intrinsic anisotropy of the single crystals of paramagnetic phases that have a preferential orientation in the rock (Zapletal, 1990; Borradaile and Werner, 1994 and Chapter 4 of this study). Some experiments have been made with synthetic samples where the orientation of microcrystals of phyllosilicates has been varied (Borradaile et al., 1985/86). Measurements of the lattice preferred orientation (LPO) of phyllosilicates with an X-

ray texture goniometer and the comparison with the AMS has been used by several authors to demonstrate the direct relationship between the LPO of phyllosilicates and the anisotropy of magnetic susceptibility (Ihmlé et al., 1989; Hirt et al., 1995; Lüneburg, 1995; Siegesmund et al., 1995; Lüneburg et al., 1999; Robion et al., 1999). Texture goniometry provides actual preferred orientation of specific minerals, e.g., mica or chlorite on a local scale whereas AMS gives the bulk anisotropy on a sample size.

This chapter investigates the relationship between the phyllosilicate fabric in natural samples and their magnetic anisotropy. A brief introduction to the mathematical methods used for the textural data analysis is presented. Then case studies of magnetic fabrics carried by paramagnetic minerals are presented using rocks from the Navio-Alto Sil slate belt in Northwestern Spain. Examples from rocks with slaty cleavage, secondary crenulation cleavage and kinks with different wavelength are examined in order to see how the magnetic fabric responds to different deformation features. The evolution of the Asturian Arc is not well known and the origin of the arc is still controversial. Ries and Schackleton (1976) proposed a tectonic bending origin. Matte and Ribeiro (1986) concluded that the arc was produced by relative motion of the core of the arc. The work of Hirt et al. (2000) and Julivert and Soldevila (1998) supports the second model. The results from these measurements are useful in distinguishing which model is more reliable for the evolution of the arc.

5.2 Methods

5.2.1 *Texture goniometer*

The preferred orientation of crystallographic planes of a mineral can be determined by X-ray goniometry. The technique is based on Bragg diffraction by which atomic planes of crystals deflect electromagnetic waves. Bragg's law relates the emitted wavelength λ with the lattice spacing d of the crystal planes and the scattering angle θ (Figure 5.1).

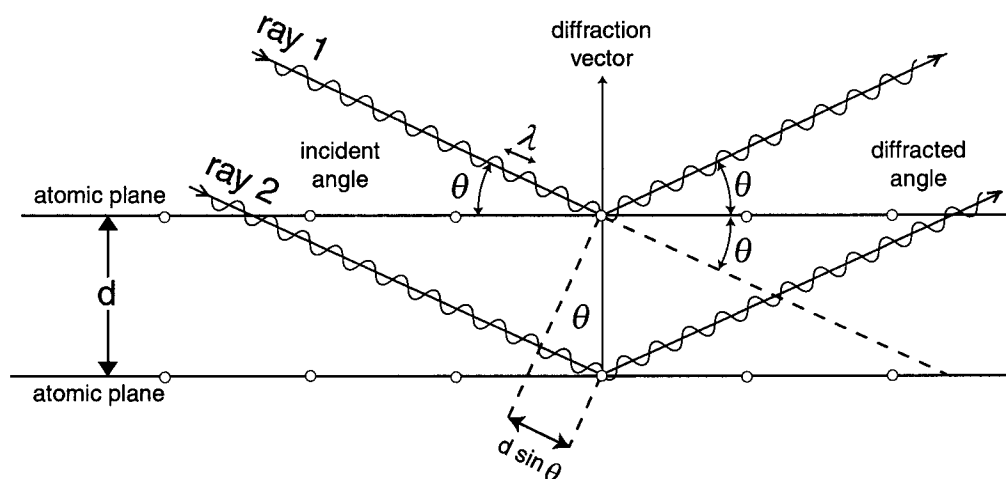


Figure 5.1: Bragg's law for a crystal with interplane lattice spacing d .

The extra distance travelled by the second ray from source to detector is given by:

$$\text{distance} = 2d \sin \theta \quad (5.1)$$

In order to have constructive interference, the extra distance must be a multiple of the wavelength. Therefore a maximum occurs at:

$$n\lambda = 2d \sin \theta \quad (5.2)$$

where n is an integer number.

Varying the orientation of the sample over different spatial directions of a hemisphere, those rays with larger diffracted intensities correspond to directions with higher preferential orientation of the selected crystallographic planes.

A texture goniometer consists of an X-ray source, a mount which holds and rotates the sample, and an X-ray counter tube or receptor. Once the crystallographic plane has been selected, the diffraction angle θ is determined from the source wavelength using Eq. (5.2). The orientation of the sample is systematically modified over a hemisphere. For each individual orientation the intensity of the diffracted beam is measured by the detector. Variations of the preferential crystallographic orientation constitute the pole figure for a specific crystallographic plane.

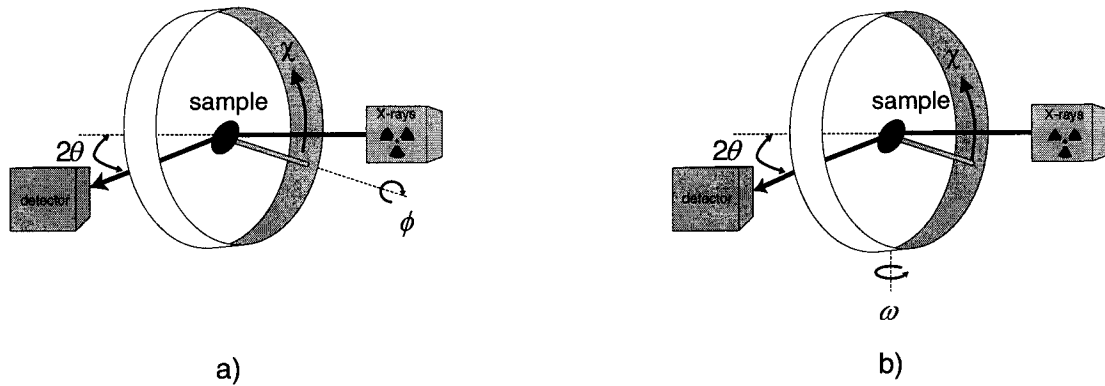


Figure 5.2: Pole figure measurements with an X-ray texture goniometer in a) reflection mode and b) transmission mode. The angles ω , ϕ and χ represent the orientation of the sample (after Wenk (1985)).

Two standard methods for pole figure measurements have been developed for goniometer analysis. In the reflection mode the beam is observed at the incident side of the sample (Figure 5.2a). The specimens in this study were blocks of the rock sample with a flat surface. As the tilt angle increases the reflected beam has a defocusing effect and a correction must be made to compensate this effect. The optimal measuring angle for this technique is less than 70° tilting angle. Above 70° tilt, the defocusing effect is too high. The sample must be impermeable to X-rays to avoid intensity loss, which is certainly the case for a thickness of several millimetres. The signal is also corrected for background signal.

In transmission mode the X-ray beam passes through the sample (Figure 5.2b). This requires a specimen that is a thin section ($50 \mu\text{m}$) removed from the glass. This method is applied for tilt angles greater than 60° . The combination of reflection and transmission measurements from a single specimen provides a complete pole figure after appropriate intensity corrections (Casey, 1981). The surface of the specimen measured varies largely with diffraction and tilt angles and extends between 2 and 20 mm.

The samples in this study have been measured on a SCINTAG-USA/DMS 2000 goniometer equipped with a Cu-X-ray source with a wavelength $\lambda = 1.54 \text{ \AA}$. All the spatial directions on the hemisphere were covered with a grid of $5^\circ \times 5^\circ$ with a total of 1387 measurements (Figure 5.3a). To have the same weight a scaling factor was assigned for each of the nodes in the grid. The weight factor for each node consists of the area subtended for each individual node of the grid (Figure 5.3b).

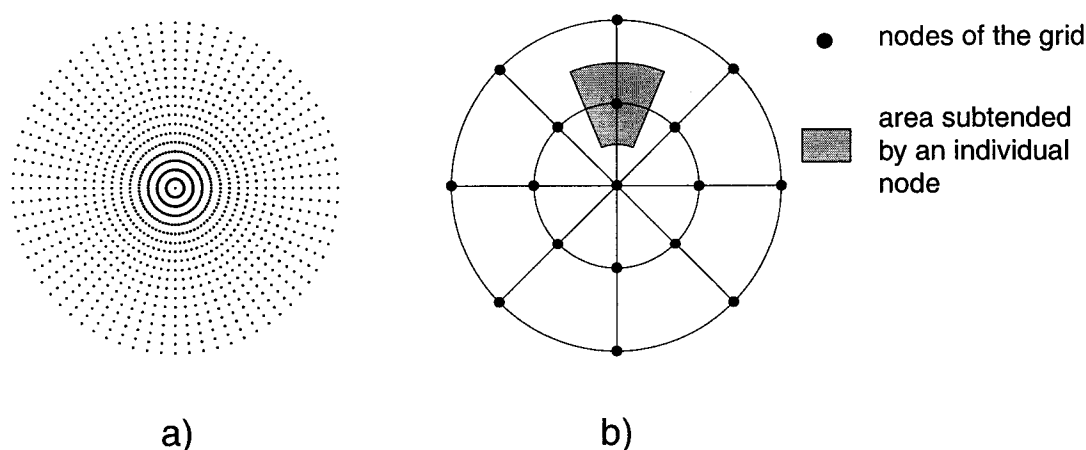


Figure 5.3: a) Original $5^\circ \times 5^\circ$ grid for the goniometer measurements, b) simplified diagram of the area subtended by one of the nodes.

5.2.2 X-ray diffraction scan

In order to identify the minerals present in the samples used in this study, X-ray diffractograms were made over a wide range of 2θ angles. As explained above in Eq. (5.2), Bragg's law relates diffraction angle with specific crystal lattice spacing. Figure 5.4 shows an example of a diffractogram for a slate, in which the diffraction peaks for mica (001) (8.71°) and chlorite(002) (12.41°) are shown (Brindley and Brown, 1980). Only these two minerals showed significant peaks in the diffractogram and were the selected peaks in the texture goniometry analysis. The 2θ angles are converted to planar lattice spacing using Bragg's law.

It should be noted that the mineral identification is not unique; different diffraction peaks can overlap so that it is not possible to separate individual peak maxima. This is particularly a problem with the micas in the samples. The planar distance for basal plane of biotite is 10.1 \AA while the value for different polymorphs of muscovite can range from 9.97 \AA to 10.0 \AA (Brindley and Brown, 1980). Thus the measured signal at the corresponding diffraction angle of 8.71° is a superposition of the intensity due to biotite and muscovite, and is simply called "mica". The chosen peaks, mica (001) and chlorite (002), fulfil the two main premises required for the measurements: high-diffraction intensity and well-isolated peaks with respect to neighbouring peaks.

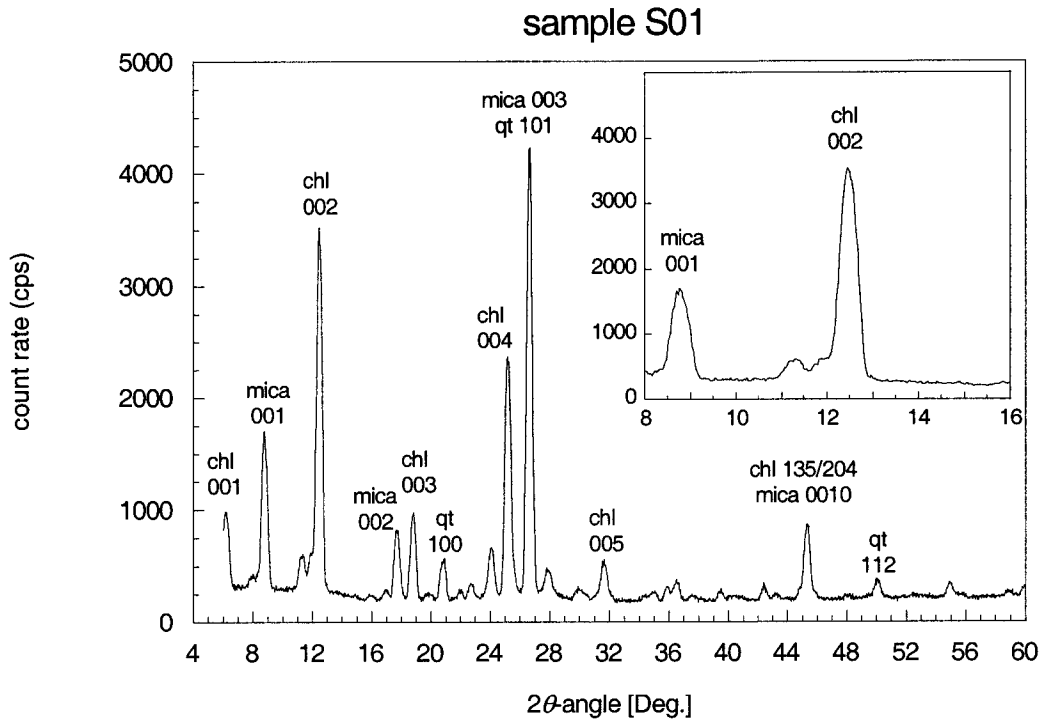


Figure 5.4: Diffraction scan on a slate sample, S01. The sample section which contains the cleavage plane is oriented perpendicular to the diffraction vector. The main peaks are identified as diffraction peaks of mica and chlorite (chl) but also picks due to the presence of quartz (qt) have been measured. The inset shows the two diffraction peaks used for the fabric measurements.

5.2.3 The Scanning Electron Microscope

The Scanning Electron Microscope (SEM) is a microscope that uses electrons to form an image. It produces a beam of electrons that scans the specimen surface and emission signals result from the interaction between the high-energetic beam electrons and the specimen. Secondary electrons (SE) are low-energy electrons predominantly produced by the interactions between energetic beam electrons and weakly bonded conduction-band electrons in metals or the valence electrons of insulators and semiconductors. Back-scattered electrons (BSE) are high-energy electrons of the emitted beam that are deflected from the sample due to collisions with the atomic nuclei.

The SE radiation is very sensitive to variations in the topography of the sample. To obtain an SE-image the sample is covered by a gold layer that improves the conductivity and avoids charge build-up for non-conducting specimens/

The BSE radiation is highly dependent on the atomic number of the nuclei and therefore is used to analyse the composition of the samples. The surface of samples used for BSE imaging are polished and coated with a layer of carbon to improve the conductivity. The emitted X-rays give a semiquantitative analysis (EDX) of the element composition of the samples, focusing the electron beam on a restricted area.

The instrument used for the analysis is a CAMSCAN CS44LB. The instrument has a standard SE detector operating with 25 kvolts and a 2 nA beam current. For BSE imaging, the instrument has a 4 quadrant semiconductor detector operating at 15 kvolts. The working distances ranged between 20-24 mm in all the measurements.

5.2.4 *Texture analysis*

5.2.4.1 *Pole density distribution*

The data obtained from the diffraction experiments consist of a pole density distribution or "*pole figure*". To obtain the complete orientation distribution for a mineral, the three-dimensional Orientation Distribution Function (ODF) is required. The number of pole figures necessary to determine the ODF depends on the crystal symmetry (Bunge, 1982). In the particular case of platy minerals such as phyllosilicates only the poles to basal plane (001) respectively (002) are important. It is assumed that no preferential direction exists in the basal plane of the phyllosilicate.

The common way in which pole density distributions have been represented is as contour plots of the orientation distribution, in which the probability density is normalised. The distance between contour lines as well as the maximum intensity can be chosen for each representation. Multiples of 1 represent multiples of random distributions (m.r.d.), illustrating how well-developed the texture of the sample is compared to a random orientation distribution (Figure 5.5). The probability density is plotted in sample coordinates on lower hemisphere equal area projection, with the x direction of the sample oriented toward top. The original textural data were first filtered to eliminate high frequencies due to noise of the measurement.

5.2.4.2 Texture ellipsoid

The vector components for each point over the unit hemisphere are calculated, using coordinates:

$$\begin{aligned}x &= e_1 = \cos \varphi \sin \theta \\y &= e_2 = \sin \varphi \sin \theta \\z &= e_3 = \cos \theta\end{aligned}\quad (5.3)$$

where θ is the vertical angle between the z -direction and the vector and φ is the azimuthal orientation. A matrix T is defined in order to fit the probability density into a symmetric second-rank tensor (Cheeney, 1983). Every term of the T matrix is defined as an integral over the hemisphere of the product of two vector components weighted with the probability density measured in this direction.

$$T(i, j) = \frac{3}{2\pi} \int_0^{2\pi} \int_0^{\pi/2} e_i(\theta, \varphi) e_j(\theta, \varphi) P(\theta, \varphi) d\theta d\varphi \quad (5.4)$$

The discrete expression of the symmetric T matrix is given by:

$$T(i, j) = \frac{3}{2\pi} \sum_l e_i(\theta_l, \varphi_l) e_j(\theta_l, \varphi_l) P(\theta_l, \varphi_l) A(\theta_l) \quad i, j = 1, 2, 3 \quad (5.5)$$

where e_1 , e_2 and e_3 are the Cartesian coordinates of the l -direction defined by θ_l and φ_l (Eq. (5.3)), $P(\theta, \varphi)$ is the probability density for the l -direction and $A(\theta)$ is the scaling factor or area subtended by this direction and defined by:

$$A(\theta_l) = \cos \theta_{l+1} - \cos \theta_l \quad (5.6)$$

By finding the eigenvalues and eigenvectors of the symmetric matrix T the principal directions of the texture ellipsoid are determined. The principal values of the ellipsoid are defined as $t_3 \geq t_2 \geq t_1$ (with the normalisation criteria $t_3 + t_2 + t_1 = 3$), because the maximum textural direction is related to the minimum susceptibility direction in phyllosilicates (Siegesmund et al., 1995; Lüneburg et al., 1999). For a random texture, in which $P(\theta, \varphi) \equiv 1$, the eigenvalues obtained would be $t_3 = t_2 = t_1 = 1$.

For a phyllosilicate single crystal the eigenvalues are $t_3 = 3$; $t_2 = t_1 = 0$. An example of the orientation of the eigenvalues of a specific phyllosilicate mineral fabric on the equal area projection is shown in Figure 5.5.

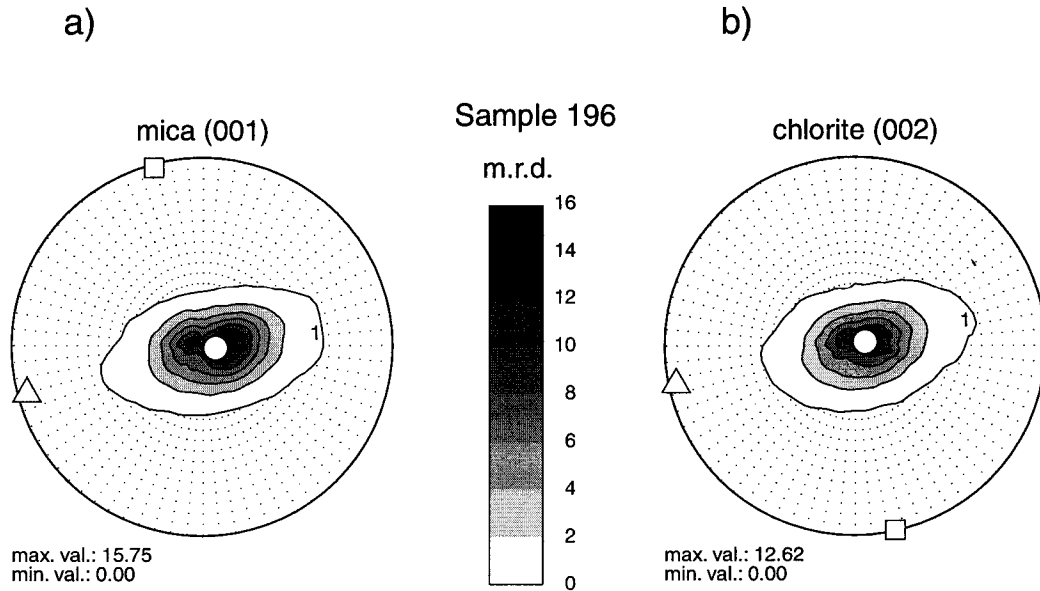


Figure 5.5: Contour lines of the probability density of phyllosilicate basal poles for a slate sample. a) mica (001), and b) chlorite (002). The first contour line correspond to 1 considered random distribution, the bar represents the gray scale from 0 to 16 multiples of random distribution (m.r.d.). Maximum and minimum density for each pole figure indicated. Symbols represent eigenvectors of the texture ellipsoid, where circles correspond to the maximum eigenvalue, triangles the intermediate eigenvalue and squares minimum eigenvalue in this and subsequent figures.

5.3 Results

5.3.1 Studied area

The Navia-Alto Sil slate belt is a Hercynian orogenic belt located in northwestern Spain, to the West of the core of the Ibero-Armorican arc. It is located in the West Asturian-Leonese zone. The regional metamorphism grades from greenschist in the east to amphibolite facies toward the west (Martinez and Rolet, 1988). The Navia-Alto Sil slate belt is located in the eastern part of the zone in the greenschist facies area, where the intrusion of granitic bodies has produced andalucite by contact

metamorphism. The belt consists of Ordovician slates, the Luarca formation, which was chosen for this study (Figure 5.6). The slates are typical roofing slates, that display a well-developed slaty cleavage, persistent all the belt. Three main deformation phases of Hercynian age can be identified in the rocks used in this study (Julivert and Soldevila, 1998). These include:

- A first deformation phase, responsible for the generation of folds with a planar slaty cleavage, which is found at sites S01, S05, S06, S07, S08, S09, S10 and S11. A stretching lineation has been defined at S46 and S04, based on pressure shadows around pyrites in some of these areas. The shadows around pyrites indicate the presence of pressure solution (Hirt et al., 2000).
- In a second deformation phase a strong crenulation overprints the cleavage in some areas (e.g., S86). This secondary crenulation cleavage is more intense in the northern part of the belt and almost absent in the southern areas.
- Kink bands which show the third deformation phase are found in areas where cleavage has not been disturbed by crenulation cleavage. The wavelength of the kink bands can vary on an outcrop scale from centimetres to decimetres becoming chevron structures (e.g., S37).

An extended analysis of the anisotropy of magnetic susceptibility has been done in the area by Hirt et al. (2000). They also measured finite strain at three areas along the arc by pressure shadows around pyrites and from the distribution of rutiles. A good correlation was found between the stretching lineation direction and the maximum magnetic susceptibility directions. The magnetic anisotropy data presented in this work includes some results published by Hirt et al. (2000), with the addition of new data. The notation of the sites from the published study is maintained in here. A total of 300 cylindrical samples with 2.54 cm of diameter and 2.3 cm length was collected. From each site, one sample was further used for texture analysis, being cut in the appropriate plane. The mineral texture was examined at 12 sites in the Luarca slates, distributed around the fold belt (Figure 5.6).

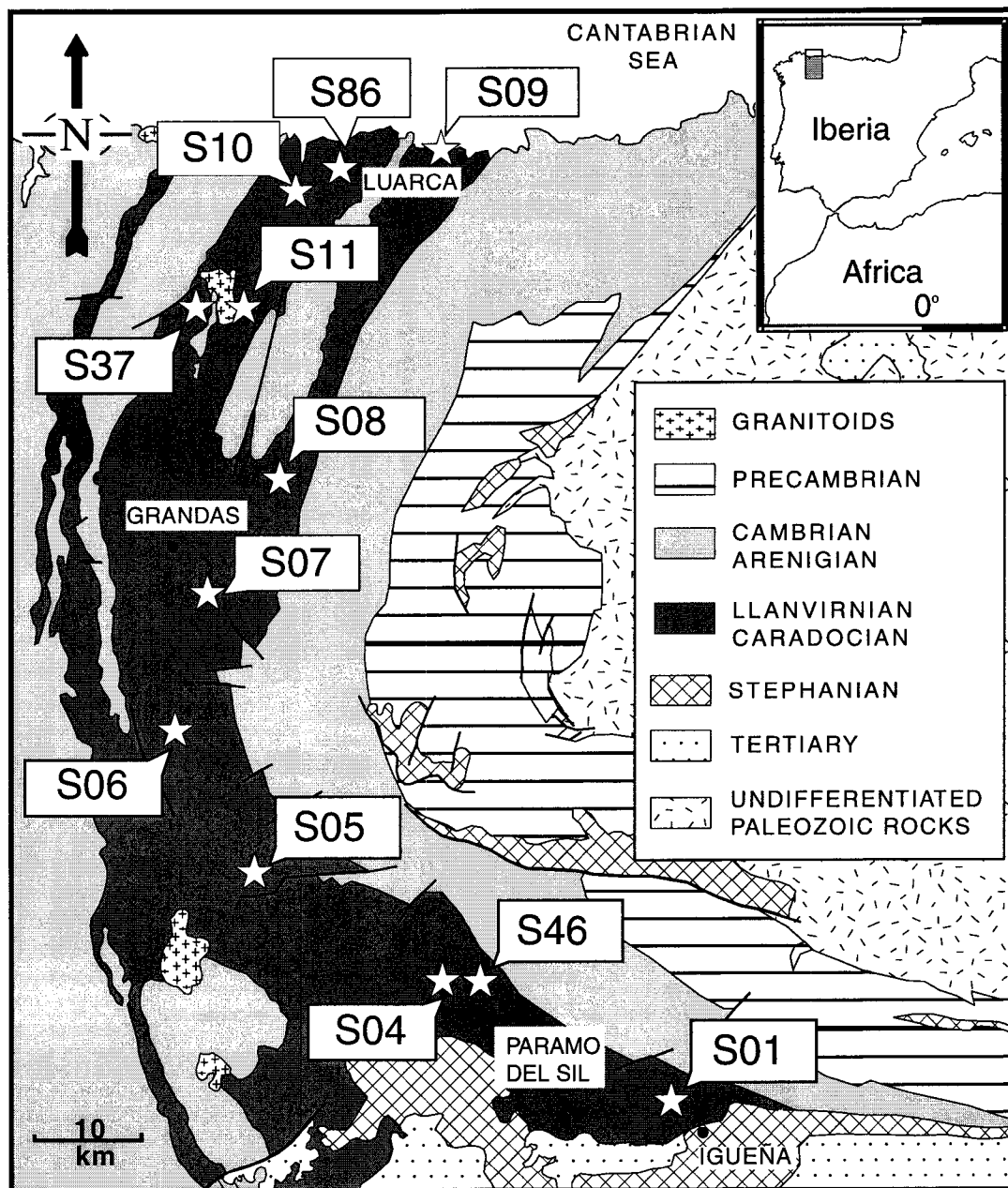


Figure 5.6: Geological sketch map of the Navia-Alto Sil slate belt, north-western Spain (modified from Julivert and Soldevila (1998) and Hirt et al.(2000)). The stars show the locations where samples were taken.

The AMS parameters of the samples analysed by texture goniometry are summarised in Appendix B. The mica and chlorite fabric tensor parameters are summarised in Appendix C and D respectively. The same samples have been measured by texture goniometry and AMS, therefore in the appendices the same label in different tables corresponds to the same sample.

5.3.2 Composition analysis of slates

5.3.2.1 X-ray diffraction

A systematic analysis of X-ray diffraction (XRD) scans has been done on the bulk samples in order to evaluate qualitatively their mineral composition (see section 5.2.2). The analysis reveals a homogeneous phyllosilicate composition of the slates along the belt (Figure 5.7).

Other samples measured along the arc presented similar features. The most relevant peaks are identified as mica and chlorite (Figure 5.4 and Figure 5.7). The bulk composition of the paramagnetic minerals in the slates is therefore similar and dominated by the presence of these phyllosilicates. No distinction could be made between micas (biotite and muscovite).

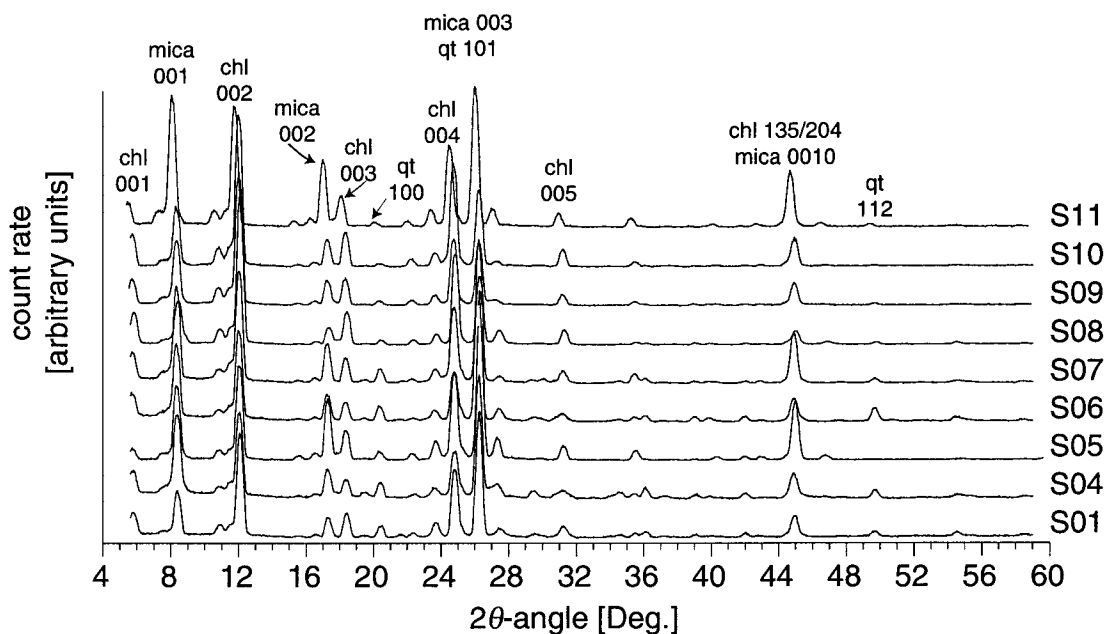


Figure 5.7: X-ray diffraction scan in normal direction for selected samples along the slate belt showing their similar bulk composition. Sample normal is parallel to the diffraction vector and normal to cleavage.

5.3.2.2 SEM back-scatter electron images

The BSE image shown in Figure 5.8 permits the identification and quantitative estimation of the main minerals in the slates.

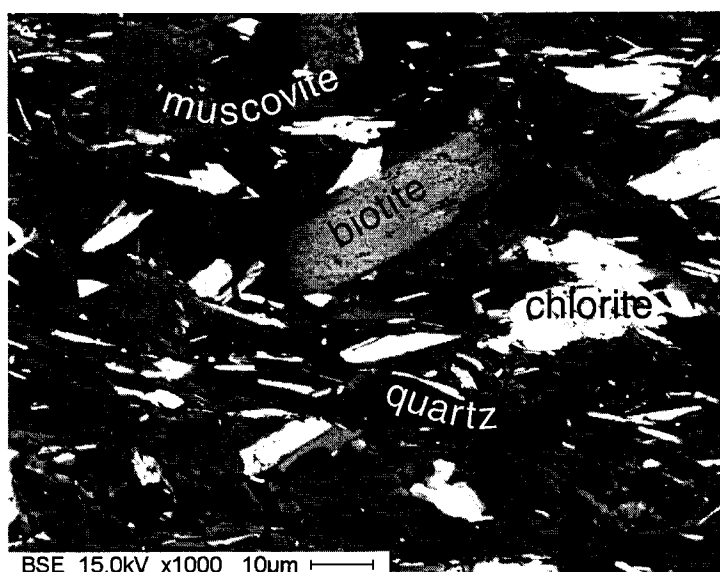


Figure 5.8: Back-scatter electron image of sample S05b in a plane perpendicular to cleavage. Labels show the minerals identified by EDX.

The three main phyllosilicates found in the samples are biotite, muscovite and chlorite. There was also abundance of quartz. Few bright white grains correspond to oxides and sulphides with high atomic number metals such as Ti and Fe. The analysis of different images from samples S04, S04b and S05b gives a semiquantitative estimation of the mineral content in the slates (Table 5.1).

Table 5.1: Semiquantitative estimation of the mineralogical content in the analyzed slates.

sample	quartz	muscovite	biotite	chlorite	oxides	undetermined
S04.a	32%	35%	8%	10%	0%	15%
S04.b	31%	33%	8%	10%	3%	15%
S04b.a	38%	32%	0%	10%	3%	17%
S05.a	18%	43%	0%	9%	0%	30%
S05.b	37%	44%	0%	6%	2%	11%
mean	31%	37%	3%	9%	2%	18%

EDX provides information about the composition of iron oxides, such as magnetite and iron sulphides, such as pyrite. Figure 5.9a shows the presence of a magnetite grain of 25 μm with some small pyrite inclusions. The presence pyrites of was also identify with different configurations (Figure 5.9b). The SEM images do not show a preferential distribution of these minerals which could lead to a significant contribution of the magnetic anisotropy in the samples.

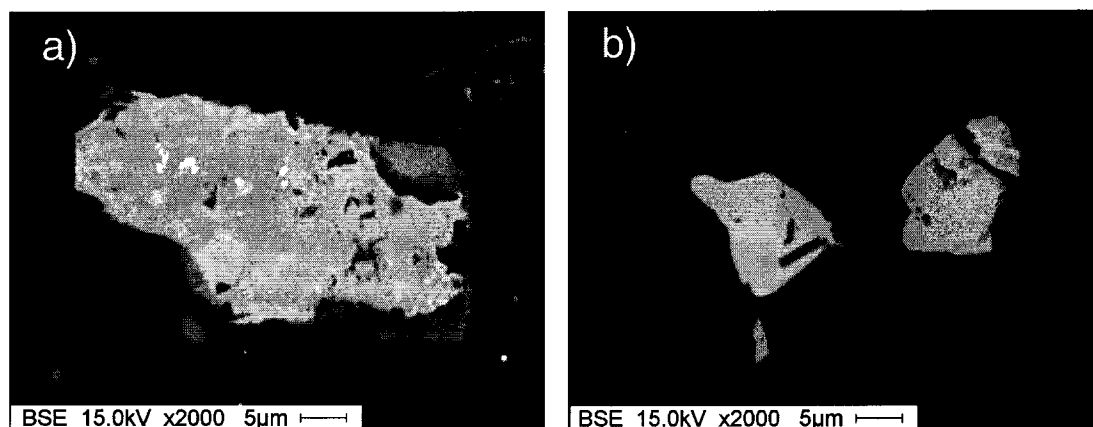


Figure 5.9: Back-scatter electron images showing the presence of iron oxides and iron sulphides at site S04. a) magnetite grain with some small pyrite grains in the top (bright white) and b) two pyrite grains with a small biotite attached to the one in the right.

5.3.2.3 IRM acquisition curves and thermal demagnetization

In order to characterise the ferromagnetic phases present in the samples, IRM acquisition curves and thermal demagnetisation of orthogonal IRM components have been measured.

The results, summarised in Figure 5.10, show a broad variety of ferromagnetic phases in the samples. No uniform pattern has been found in the distribution of ferromagnetic components within the Navia-Alto Sil slate belt. An orthogonal IRM component was then applied to selected samples, using the method outlined in Lowrie (1990). A 1.8 T field was first applied along the sample Z-axis, followed by a 0.6 T field along the sample Y-axis and finally a 0.2 T field along the sample X-axis.

The IRM acquisition curve indicates the presence in some outcrops of a low coercivity phase that saturates between 200 mT and 400 mT (Figure 5.10a). The thermal demagnetisation is dominated by the soft component (Figure 5.10b). Although the demagnetisation was not completed in all the samples because of remagnetisation of the samples in the process, the curve suggests the presence of magnetite or maghemite, since the acquisition curve is not completely saturated at 1 T.

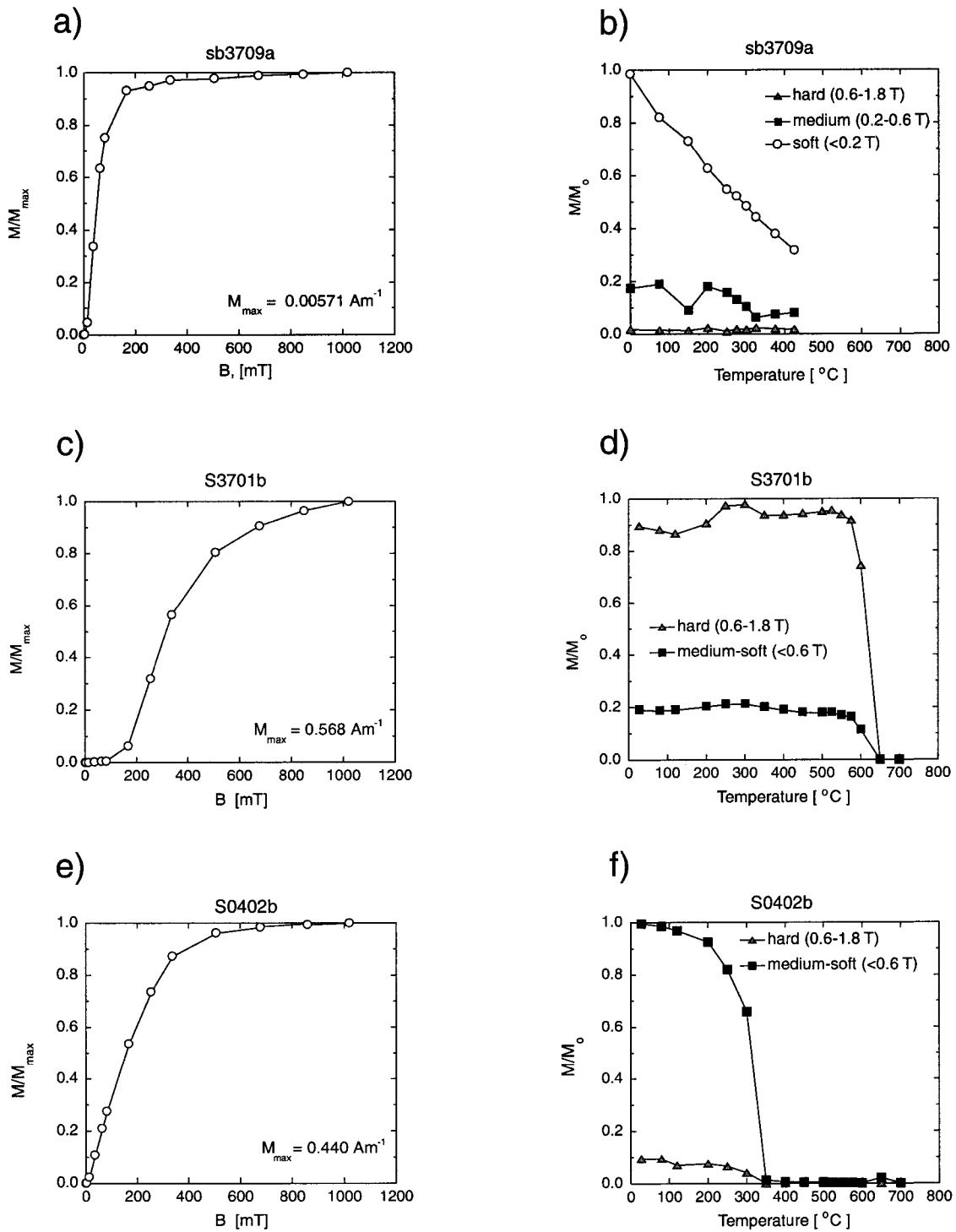


Figure 5.10: IRM acquisition (a, c, e) and demagnetisation curves (b, d, f) of two orthogonal components from a selection of samples.

Other outcrops, however, do not contain low coercivity minerals, as shown by a concave curve at low fields (Figure 5.10c). The high coercivity phase does not even saturate at the highest applied field of 1.02 T. The thermal demagnetisation of

orthogonal component IRM indicates that the high coercivity has an unblocking temperature of 650°C (Figure 5.10d). The medium coercivity is also removed at the same temperature, suggesting that the same mineral is responsible for the magnetisation of this medium component. Hematite is the only ferromagnetic mineral present.

Some specimens were dominated by a ferromagnetic mineral with a medium coercivity in the acquisition curve. The ferromagnetic minerals are nearly saturated by 600 mT (Figure 5.10e). Thermal demagnetisation of IRM is dominated by the medium-low coercivity component which has a sudden drop in the magnetisation by 350°C (Figure 5.10f). The high coercivity component is only 10% of the total intensity and shows the same behaviour as the medium-low coercivity component. Pyrrhotite is the main ferromagnetic phase presents in the samples and possibly some traces of hematite.

5.3.2.4 *Hysteresis curves*

Hysteresis curves were measured to further characterise the magnetic mineralogy of selected samples in the slates along the belt. The measurements were done on a Micromag VSM with variable spacing between the electromagnet poles. Small cubes from the samples were cut and measured to a maximum field of 1 T. Corrections for the sample holder signal were done in all the samples. Results from the same sites in which IRM acquisition and demagnetisation curves were obtained are presented in Figure 5.11.

The hysteresis curves show a closed loop with linear trends in all samples. The slope of the linear trend in the hysteresis curve has been used to estimate the bulk paramagnetic susceptibility of the samples. Hysteresis was measured in three mutually perpendicular planes in order to estimate the bulk paramagnetic susceptibility. The obtained paramagnetic susceptibility gives a lower boundary for the low-field magnetic susceptibility measured with the KLY-2. The differences between the two susceptibilities range between 1 and 5%.

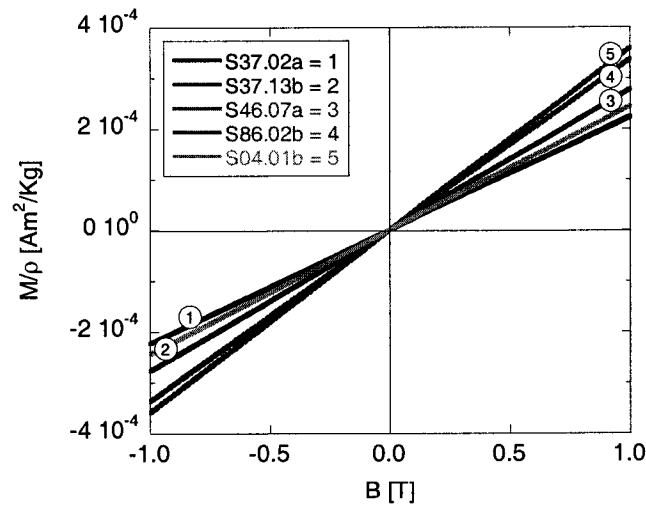


Figure 5.11: Magnetic hysteresis curves of slates from the Navia-Alto Sil slate belt.

5.3.2.5 High-field torque magnetometer

A set of experiments has been performed with the intention of determining the carriers of the anisotropy of magnetic susceptibility. A selection of samples has been measured on a high-field torque magnetometer. The amplitude of the torque signal, depends linearly on the square of the applied field above the saturation of the ferromagnetic phases. On fitting the data with a least squares method, the intercept with the ordinate axis was found to be not significantly different from zero. This suggests that no significant ferrimagnetic phases contribute to the anisotropy of the samples (Figure 5.12a). This is further confirmed with the analysis of the principal directions of the AMS (Figure 5.12b).

After the separation of the ferrimagnetic and paramagnetic components of the samples, using the method outlined in Chapter 3, the ferrimagnetic part could not be considered statistically significant. The directions of the principal axes of AMS are almost coincident with the paramagnetic susceptibility axes obtained with the torque magnetometer (Figure 5.12b).

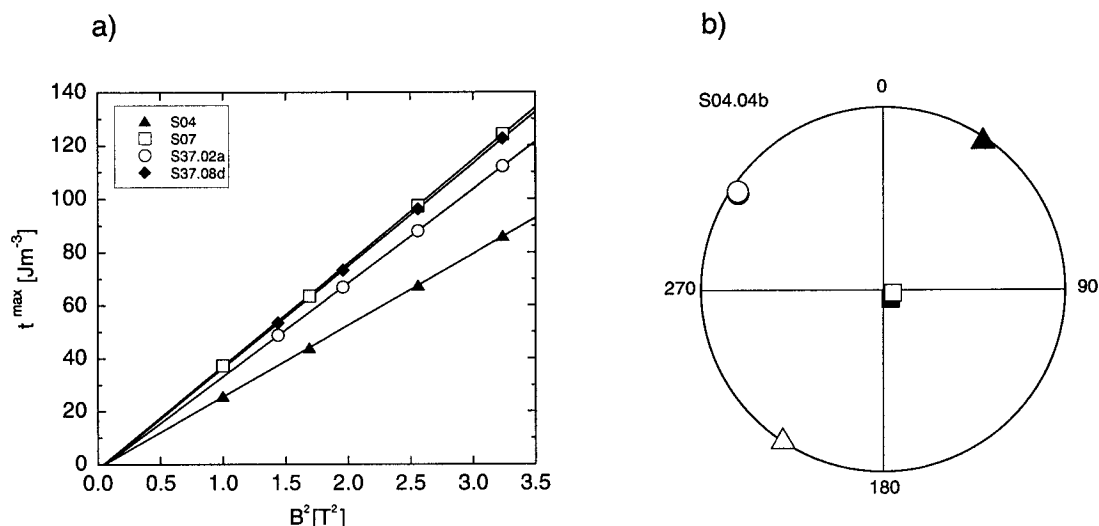


Figure 5.12: Measurements on a high-field torque magnetometer. a) maximum amplitude of the torque signal as a function of the square of applied field for four representative samples and b) principal directions of the anisotropy of the magnetic susceptibility in sample coordinates. Black symbols show the AMS principal directions and open symbols those of the paramagnetic susceptibility.

5.3.2.6 Magnetic susceptibility at low temperature

Measurements of the magnetic susceptibility at different temperatures yield information about the type of magnetic minerals in the samples. Since the susceptibility of paramagnetic minerals follows the Curie-Weiss law, the ratio of the magnetic susceptibility at two different temperatures is the inverse ratio of the temperatures when $T \gg \theta$ (see section 2.2.2). For this reason the magnetic susceptibility was measured at room temperature (293 K) and at liquid nitrogen temperature (77 K). If the susceptibility of the samples is carried by paramagnetic phases the ratio of the two susceptibilities should be $293/77 \approx 3.8$. A total of 113 samples were measured along the slate belt in this experiment (Figure 5.13a).

A linear regression was computed with the magnetic susceptibility at room temperature and its correspondent at 77 K with the following fit, where R is the linear correlation coefficient:

$$K_{bulk}^{77K} = (3.8 \pm 0.4) K_{bulk}^{293K} \quad R=0.80$$

A very good agreement is found between the theoretical value for a purely paramagnetic mineralogy. The error interval calculated with a 95% confidence reflects mostly the errors in the temperature. The principal axes of the low-field magnetic susceptibility at low temperature are also the same as those measured at room temperature (Figure 5.13b).

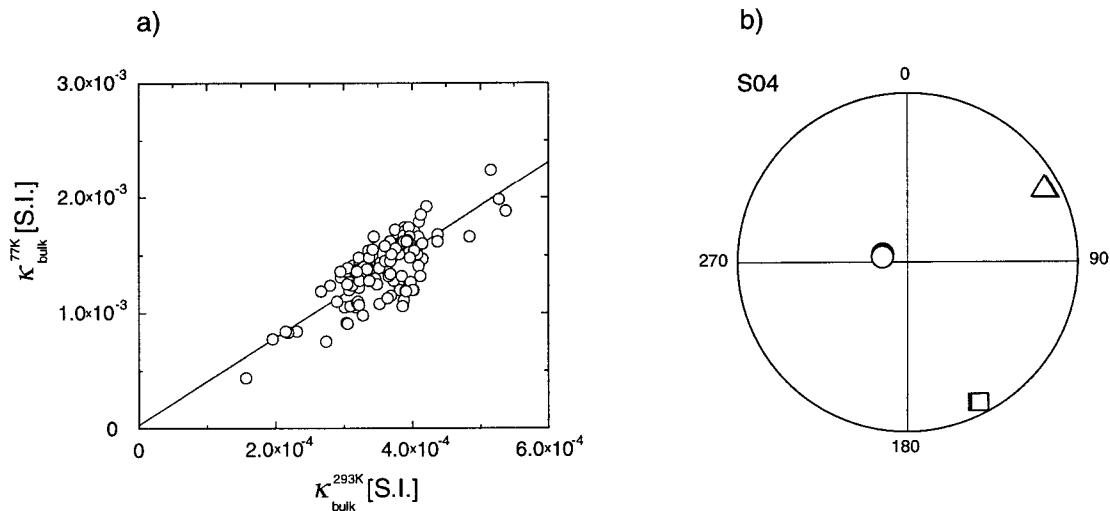


Figure 5.13: Low temperature susceptibility measurements. a) Relationship between the bulk susceptibility at room temperature and at 77 K. Line shows the best linear fitting calculated by least squares. b) Low-field anisotropy of magnetic susceptibility measured at two different temperatures; black symbols represent the measurements at room temperature and open symbols measurements at 77 K.

The results obtained from this experiment further prove that the magnetic anisotropy in the analysed samples is carried mainly by the paramagnetic minerals in the rocks. In the light of the X-ray diffraction and SEM analysis, which identifies the minerals in the slates, the anisotropy is evidently carried by the phyllosilicates (chlorite and mica).

5.3.3 Slaty cleavage

Texture goniometry is an excellent tool for the analysis of cleavage development (Sintubin, 1994; Lüneburg, 1995). Two main features are found in samples with a well-developed slaty cleavage. A high intensity pole figure is found the northern part, with the maximum texture eigenvalue sub-parallel to the pole to cleavage. The

probability density shows a point maxima with axial symmetry within the cleavage plane. Maximum intensity of the texture ellipsoid is sub-parallel to the pole to cleavage for the two analysed phyllosilicates while the other two main texture directions lie in the cleavage plane. Samples S08, S09, S10 and S11 show this texture (Figure 5.14), which have been named *compression texture* by Sintubin (1994). In these samples the anisotropy of the magnetic susceptibility is controlled by the cleavage. Minimum susceptibility directions are sub-parallel to the pole to cleavage and the maximum and intermediate axes show a girdled distribution along a great circle defined by the cleavage plane (Figure 5.15e to Figure 5.15h). The shape of the susceptibility ellipsoid is nearly perfectly oblate and is homogeneous in the whole area, with values lying in the upper part of a Jelinek plot (Figure 5.16e to Figure 5.16h).

In the southern part of the arc, samples S01, S05, S06 and S07, the texture characterised by a less intense fabric with respect to the compression texture and the pole figure distribution has an ellipsoidal shape (Figure 5.14). The maximum texture direction is also sub-parallel to the pole to cleavage. In this study this will be referred to as *elongated texture*.

In the measured samples no stretching lineation was visible at the scale of hand specimens, but the minimum texture direction is sub-parallel to a well-defined magnetic lineation; i.e., a grouping of the maximum susceptibility direction (see Chapter 2) within the cleavage plane (Figure 5.15a to Figure 5.15d). Although the magnetic susceptibility ellipsoid also shows an oblate shape the values are more scattered and the degree of anisotropy is smaller compared to the other sites (Figure 5.16a to Figure 5.16d).

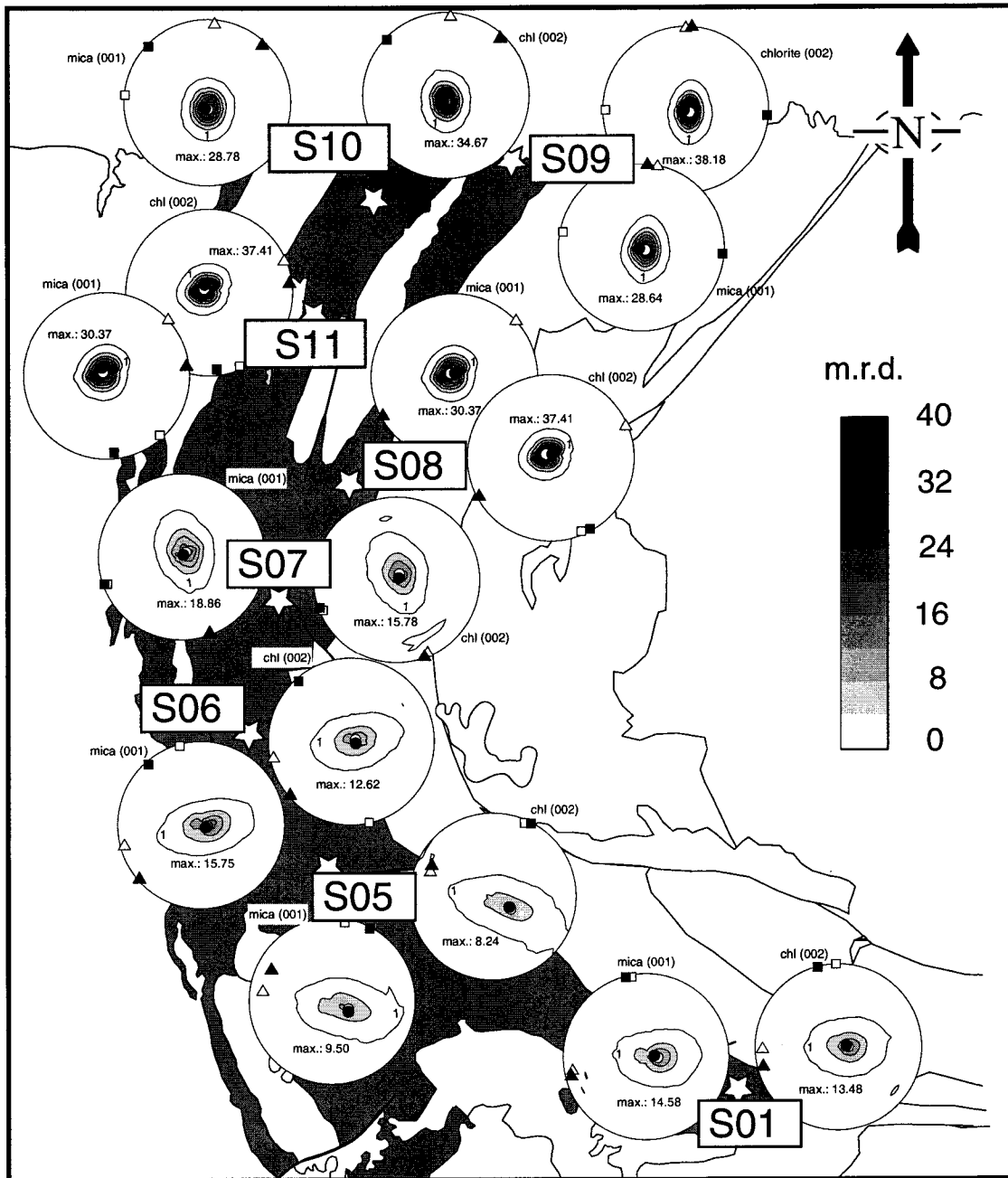


Figure 5.14: Pole figures for mica (001) and chlorite (002) determined by X-ray goniometry. Pole figures are oriented normal to cleavage plane for all samples. The AMS principal directions are represented by black symbols and the fabric principal directions by open symbols. The same symbols and colour scheme are used in subsequent figures.

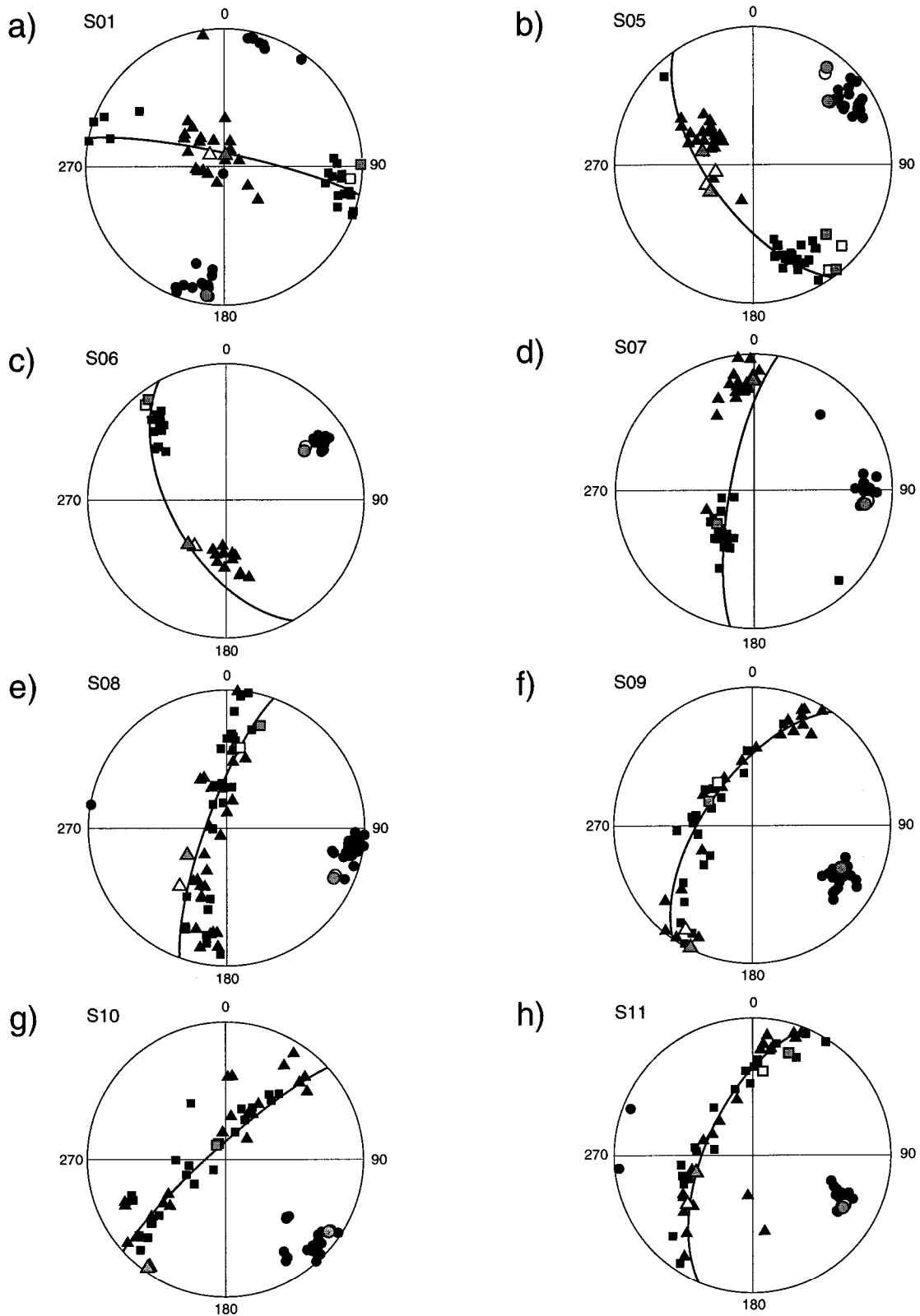


Figure 5.15: Anisotropy of magnetic susceptibility of sites with a well-developed slaty cleavage are plotted with black symbols. Directions of the textural ellipsoid plotted for mica (open symbols) and chlorite (gray symbols) in this and subsequent figures. The great circles represent the cleavage plane measured in the field.

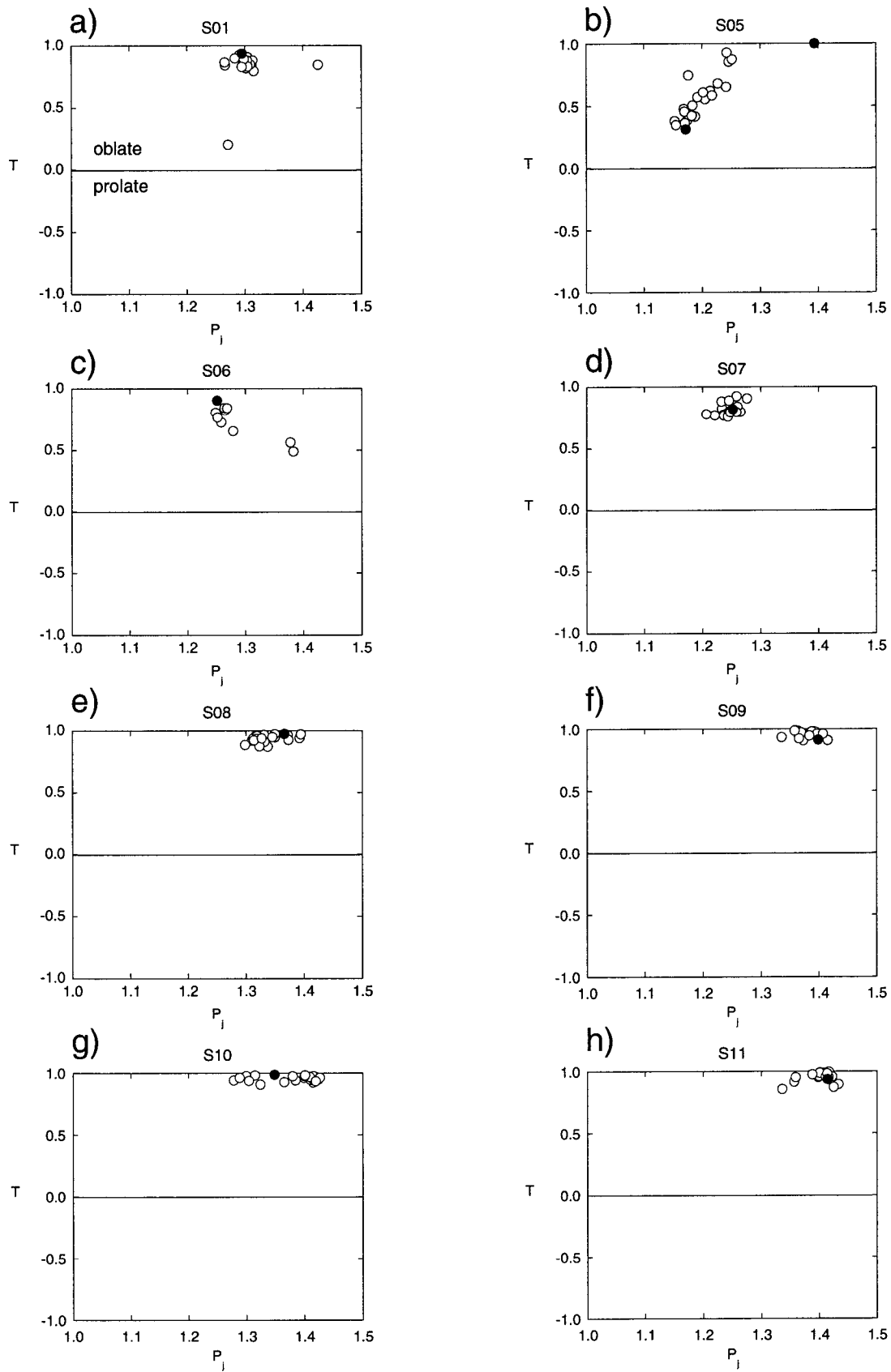


Figure 5.16: Jelinek plot for samples with a well-developed slaty cleavage. Black symbols represent the AMS parameters of the sample analysed with the texture goniometer.

When correlating the magnetic parameters and textural analysis it is not possible to distinguish the maximum and intermediate axes for the sites with near-oblate shape (black symbols in Figure 5.17). It is, however, possible to distinguish between the maximum and intermediate axes when the magnetic anisotropy as well as the texture have triaxial ellipsoids, i.e., show a lineation (gray symbols in Figure 5.17).

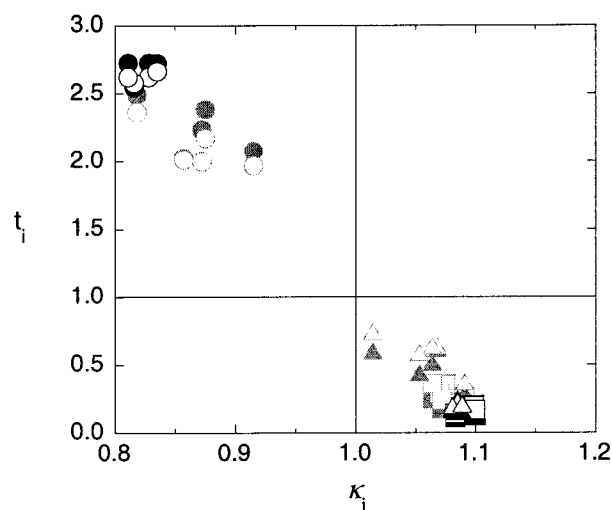


Figure 5.17: Comparison between magnetic anisotropy ellipsoid and textural ellipsoid for sites with a well-developed cleavage. Correlation between the principal values of the textural ellipsoid and normalised semiaxes of the AMS. Symbols in gray correspond to samples with “elongated texture” and black to “compression texture”. For the same colour full symbols are measurements for mica and open symbols for chlorite.

5.3.4 Stretching lineation

In some of the analysed sites with a well-developed slaty cleavage a stretching lineation was observed in the field (e.g. at sites S04 and S46 in Figure 5.6). The stretching lineation was confirmed by the presence of pyrites with pressure shadows within the cleavage plane. These strain markers have been used by Hirt et al. (2000) to determine finite strain orientation, and they found that the direction of maximum magnetic susceptibility reflects the stretching lineation direction. Texture analysis was done at these sites in order to check whether the phyllosilicates reflect the presence of stretching lineation in the samples, since it is not obvious if the phyllosilicates are oriented in the stretching lineation direction.

The texture in the two sites with stretching lineation does not show a general feature. It is characterised by pole figures of medium intensity, less than in samples with “elongate texture”. In samples from site S04 the probability density of chlorite basal plane is distributed in a girdle and for mica shows an elongated shape. The maximum probability direction is sub-parallel to the minimum susceptibility axis and the minimum probability sub-parallel to the magnetic lineation (Figure 5.18). The sample for texture analysis at site S46 shows a point maxima. It was not cut exactly perpendicular to the cleavage plane, however it may not be representative of the mineral fabric in the cleavage plane.

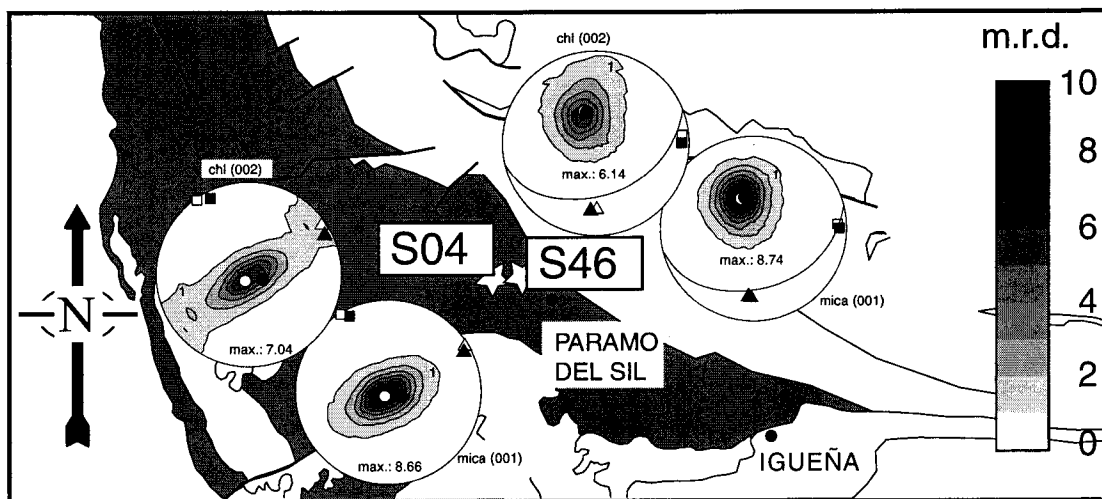


Figure 5.18: Pole figures of mica and chlorite and principal axes of AMS ellipsoid for sites with a stretching lineation. The great circle shows the orientation of cleavage plane in the sample coordinates system. Sample S04 was measured perpendicular to the cleavage plane.

The direction of magnetic lineation is sub-parallel to the direction of minimum probability of phyllosilicate poles for both mica and chlorite (Figure 5.19a and Figure 5.19b). The directions correspond also with the stretching lineation direction measured from pyrite pressure shadows reported in Hirt et al. (2000). The effect of a stretching lineation on the shape of the magnetic susceptibility ellipsoid results in a less oblate ellipsoid that reaches the neutral ellipsoid in site S04. Also the degree of anisotropy is smaller with respect to the values in samples with well-developed cleavage (Figure 5.19c and Figure 5.19d).

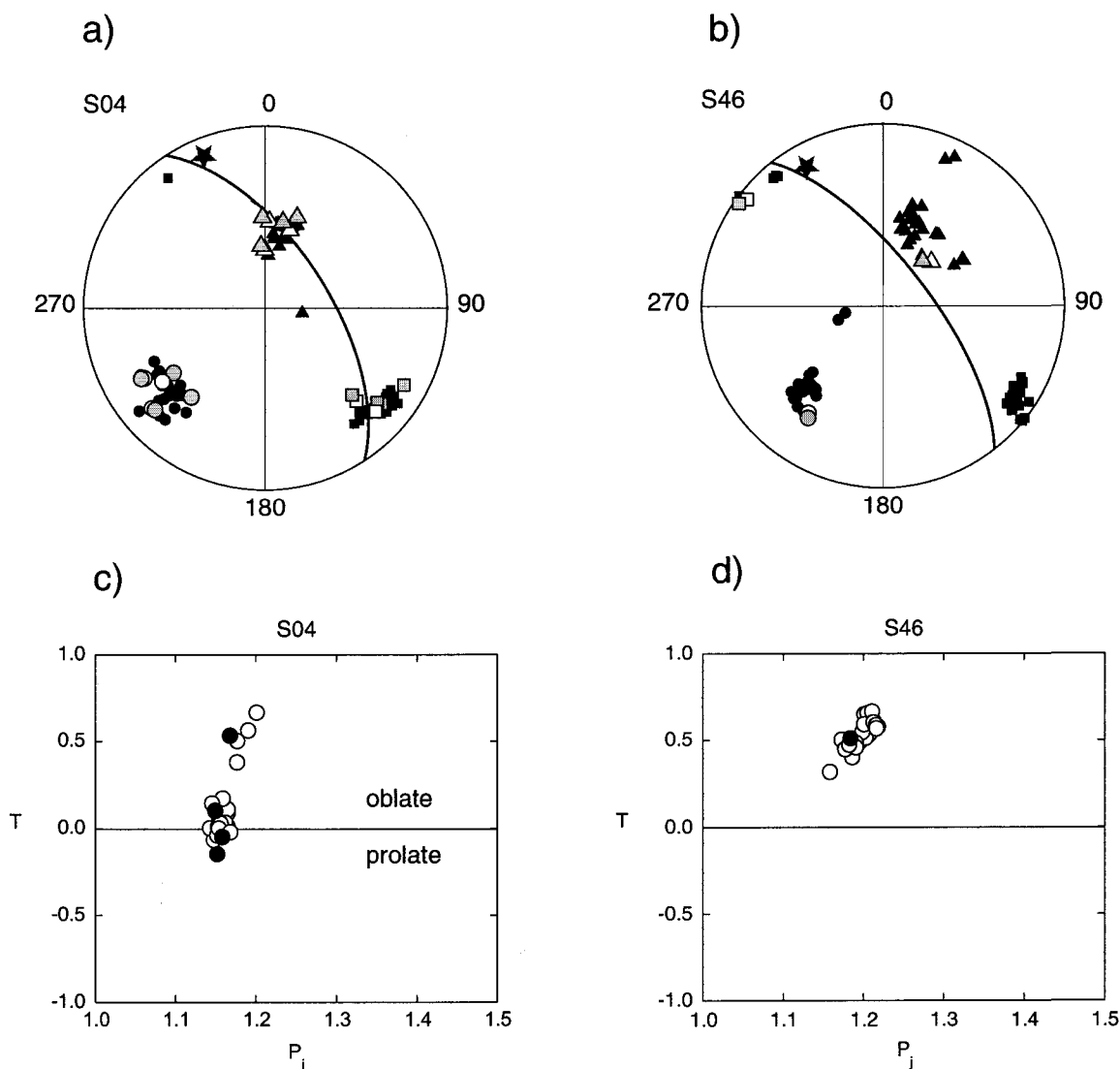


Figure 5.19: Magnetic susceptibility ellipsoid in sites with a well-defined stretching lineation. a) and b) Principal axes of the AMS and the texture ellipsoid for the phyllosilicates. The red star represents the stretching lineation calculated from pyrites pressure shadows. c), d) Jelinek plot for the anisotropy of magnetic susceptibility. Black symbols represent samples that were also measured with the texture goniometer.

The correlation between the magnitudes of the principal values of the anisotropy of magnetic susceptibility and texture eigenvalues is in this case important because it shows how the magnetic lineation is dependent on the phyllosilicates' orientation (Figure 5.20). The values of the correlation are not very significant due to the low number of data points. The most important result is that the maximum and intermediate texture eigenvalues can be differentiated in the plot, which suggests that the lineation is caused by the phyllosilicates.

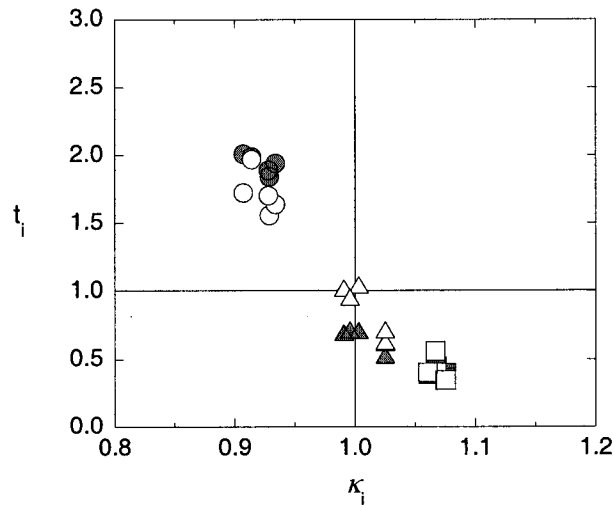


Figure 5.20: Comparison between AMS and textural ellipsoid for sites with stretching lineation. Relationship between principal eigenvalues of the AMS and principal values of the texture ellipsoid.

SEM pictures were used to investigate the origin of both the stretching lineation seen in the field and the magnetic lineation measured. The stretching lineation is visible by eye within the foliation plane. In the SE image it is seen as a linear shadow in the cleavage plane (Figure 5.9a). Several SE images were taken in a plane perpendicular to the cleavage plane and parallel to the lineation direction (plane 2). The cleavage plane can be followed as a horizontal plane where the phyllosilicates are lying (Figure 5.9b). In the space between two cleavage traces the phyllosilicates do not show an orientation pattern. The picture taken in a plane perpendicular to cleavage and perpendicular to the direction of stretching lineation shows the presence in some areas of micro-kinks (Figure 5.9c). Although these features were not found over the entire plane, the micro-kinking may be the origin of a magnetic lineation.

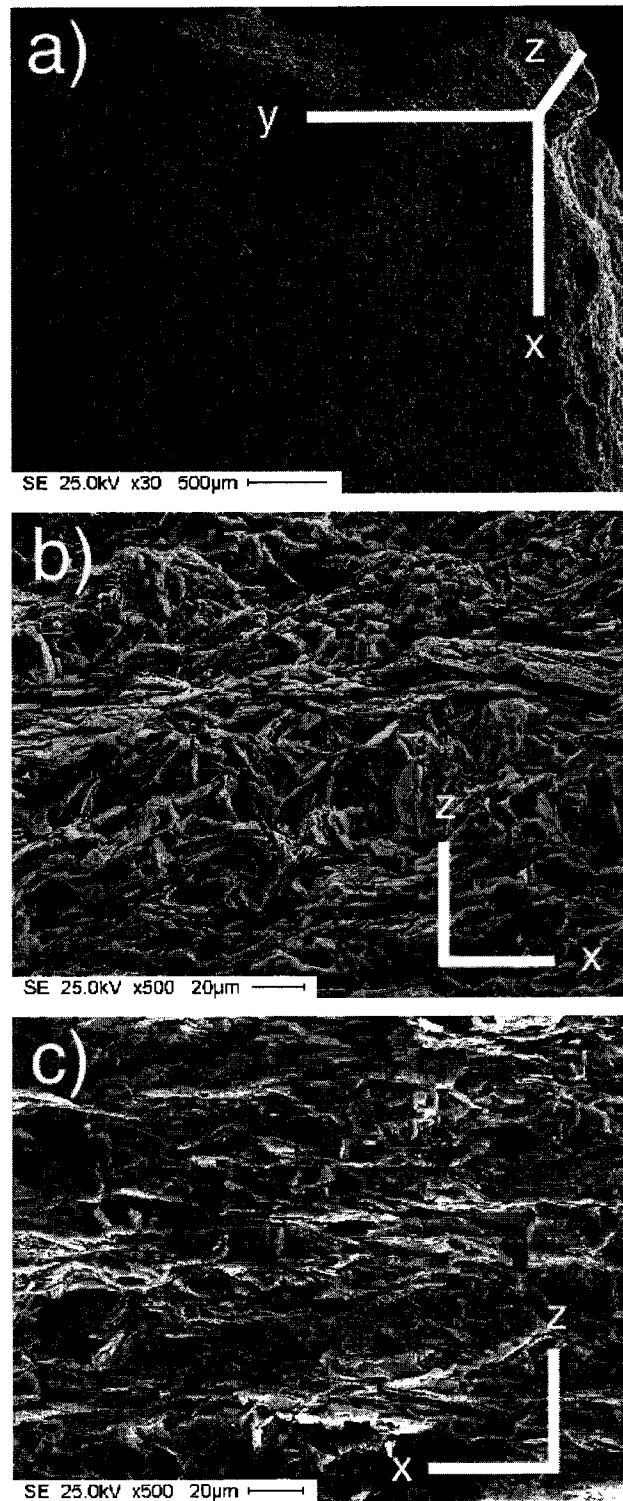


Figure 5.21: SEM images at site S04. a) SE image showing stretching lineation in the cleavage plane seen as a shadow, b) SE image in a plane perpendicular to cleavage (plane yz) and c) SE image in a plane perpendicular to cleavage and into the direction of stretching lineation (plane xz).

5.3.5 Crenulation

The development of a new cleavage fabric overprinting an existing cleavage has been termed as *transition texture* by Sintubin (1994). These textures are characterised by pole figures with medium intensity depending on the development of the secondary crenulation cleavage. The shape of the pole figure is also influenced by the orientation of the two fold limbs of the crenulation. The crenulation leads to an ellipsoidal or girdle configuration of the pole figure. The effect of crenulation on the AMS has been already reported by Johns et al. (1992) and Sun et al. (1995). They reported maximum susceptibility directions sub-parallel to the intersection between crenulation cleavage plane and cleavage plane.

In order to analyse the effect that this deformation has on the anisotropy of magnetic susceptibility one site in the northern part of the belt has been sampled, where the crenulation is more intense (Figure 5.22). The site possesses a well-developed slaty cleavage that is overprinted by a secondary crenulation cleavage.

The principal directions of the AMS ellipsoids were dominated by the cleavage plane (Figure 5.23a).

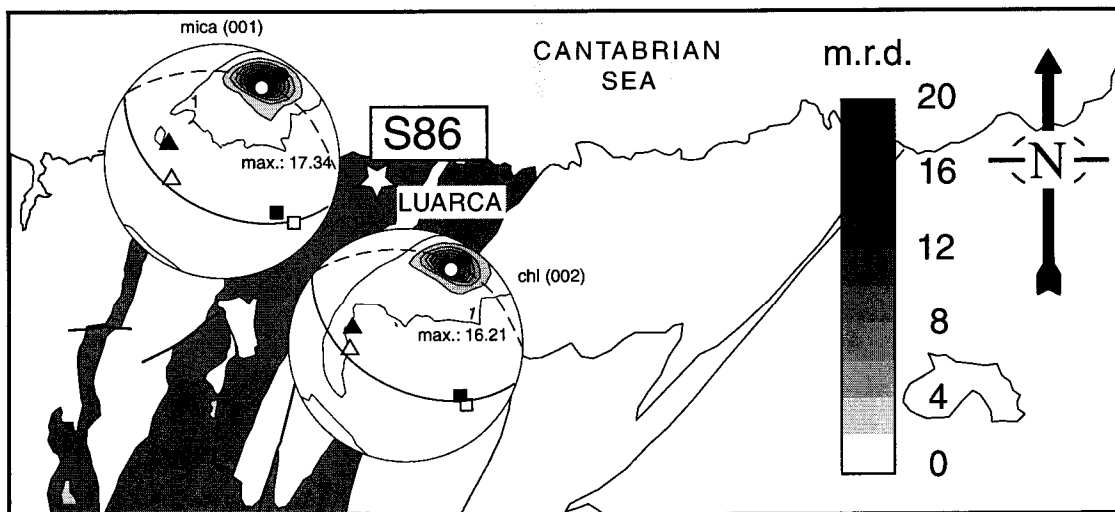


Figure 5.22: Pole figure for mica and chlorite and AMS principal axes of the ellipsoid of the corresponding sample for a site with a well-developed crenulation. Solid line shows slaty cleavage plane and dashed line crenulation plane in sample coordinate system.

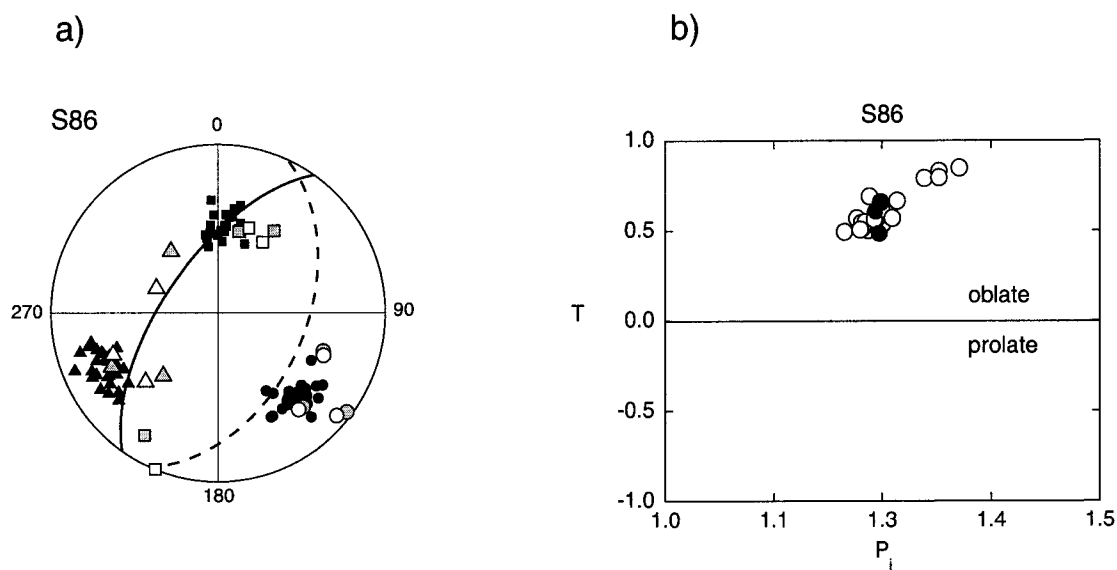


Figure 5.23: Anisotropy of the magnetic susceptibility for site S86 with crenulation. a) Principal axes of the anisotropy of magnetic susceptibility and best-fit ellipsoid of chlorite and mica fabric. Solid line shows slaty cleavage plane (S_1) and dashed line crenulation plane (S_2). b) Jelinek plot showing the shape of the AMS ellipsoid. Black symbols correspond to the samples that were also measured by texture goniometry.

Directions of the axes of minimum susceptibility are sub-parallel to the pole to slaty cleavage. A well-defined magnetic lineation is observed, which is recorded by the paramagnetic phyllosilicates as is shown by the agreement between the κ_1 direction and textural minimum principal direction. This lineation is not coincident with the intersection between cleavage plane (S_1) and crenulation plane (S_2) but offset. This offset may be due to the fact that crenulation could not be measured exactly from the area of the outcrop where the samples were taken. The triaxial AMS ellipsoid shows a higher anisotropy degree than in the case of well-developed cleavage with or without stretching lineation (Figure 5.23b).

Figure 5.24 illustrates the good agreement between the magnitudes of the principal axes of the magnetic and textural ellipsoids in a location where the lineation is caused by the superposition of two oblate magnetic fabrics. The minimum and intermediate axes of the textural ellipsoid are well constrained as in the case of the sites that show a “elongate texture” or well defined stretching lineation.

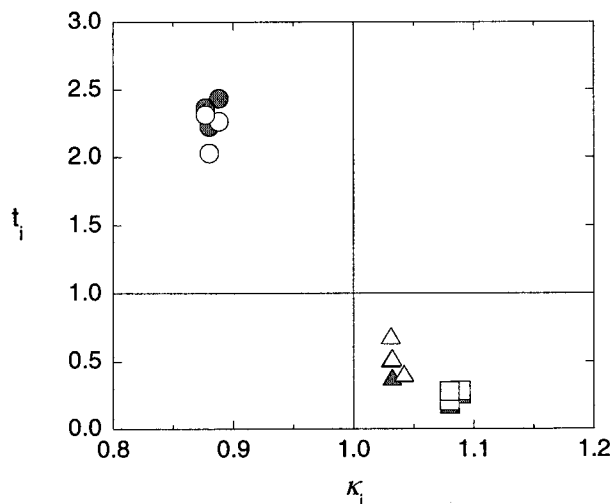


Figure 5.24: Comparison between magnetic anisotropy ellipsoid and textural ellipsoid for site with well developed crenulation cleavage. Relationship between normalised magnitudes of principal values of AMS ellipsoid and textural ellipsoid.

5.3.6 Kink bands

Kink bands exist throughout the Navio-Alto Sil slate belt where an initial cleavage has not been disturbed by crenulation cleavage (Julivert and Soldevila, 1998). Kink structures have usually been avoided in all sites used in paleomagnetic studies and magnetic anisotropy analysis. The outcrop used for this part of the study was particularly selected to analyse how the wavelength of the kink structures affects the AMS. The sampled area has a length of 50 m. Samples 01 to 02 correspond to small-scale structures with kinks of approximately 5 mm wavelength (Figure 5.25a); the samples are highly weathered. Due to the small dimension of the kinks the pole figures show two maxima which corresponds to both limbs. The minimum axis of susceptibility as well as maximum axis of texture ellipsoid lie on a great circle that joins both maxima. Therefore they represent the averaged macroscopic orientation distribution of phyllosilicates. The kink wavelength increases along the outcrop, reaching a wavelength of centimetres (Figure 5.25b). The distance between the two maxima increases in the pole figure and one maximum becomes more intense. The minimum axes of susceptibility tend to be sub-parallel to the direction of the more intense maxima.

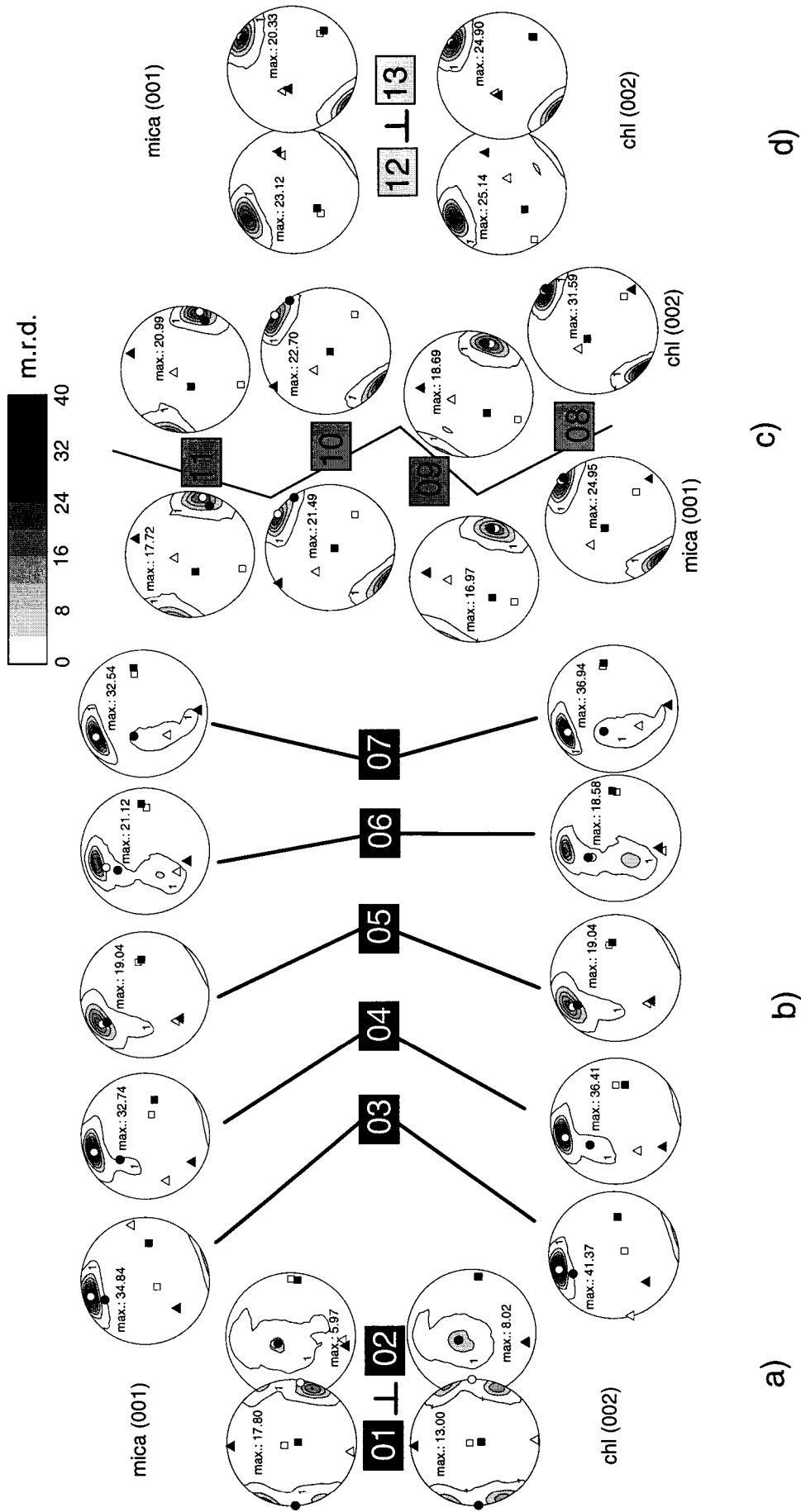


Figure 5.25: Mica and chlorite pole figure a kinked area. AMS is also plotted in black symbols. \perp means cores samples perpendicular to each other.

Sets of four cores were collected from a chevron structure in the outcrop (samples 08 to 11). They were drilled either from a limb or a hinge (Figure 5.25c). The kink has a wavelength of 10-20 cm. Since the texture goniometer measures over an area with radius 2-20mm, only the orientation distribution of a single limb is recorded. The two maxima in the pole figure disappear. At this stage the magnetic susceptibility, which is a bulk property over the whole sample, agrees with the principal directions of the texture measurements.

Samples 12 and 13 correspond to the area where no kinks are present and the samples show only a well-developed slaty cleavage with the typical "compression texture" (Figure 5.25d).

The same division of samples, as in the map in Figure 5.25, has been done for the principal axes of the AMS ellipsoid. Samples in black correspond to cores labelled from 01 to 07 (Figure 5.26a and Figure 5.26b). The AMS is dominated by the two planes of magnetic flattening which represent the two limbs of the kink present in the outcrop. The AMS shows an apparent lineation direction sub-parallel to the intersection between the slaty cleavage plane and the kinks axial plane. Intermediate and minimum axes are distributed in a plane normal to this direction and are statistically scattered. The minimum axis is in the narrower sector between both limbs.

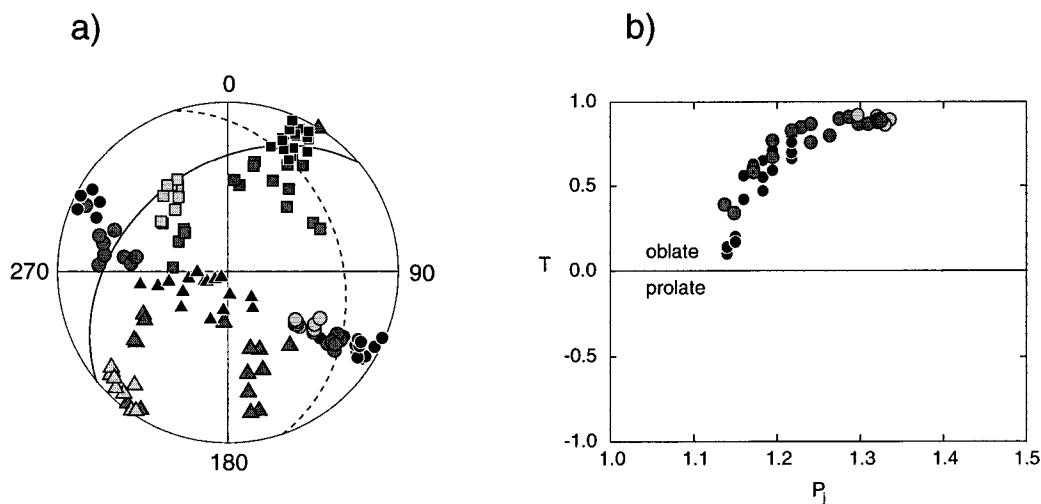


Figure 5.26: Anisotropy of the magnetic susceptibility in site S37. a) variation of the orientation of the AMS ellipsoid principal directions with the wavelength of the structures. Solid line represent the cleavage plane (S_1) and dashed line the kink plane (S_k). The meaning of the different colours is explained in the text. b) variation of the shape and degree of anisotropy along the outcrop.

Samples in gray correspond to cores from a chevron fold (Figure 5.26c). Minimum susceptibility axes are sub-parallel either to the pole to slaty cleavage or the pole to the kink axial plane. Maximum and intermediate axes are distributed on a girdle and there is no evidence of a magnetic lineation.

In the third group of samples, where only slaty cleavage is present (Figure 5.26d), the AMS, shown with light gray symbols, is controlled by the slaty cleavage plane, with κ_3 sub-parallel to the pole to cleavage. A well-defined magnetic lineation lies down-dip in the cleavage plane.

The most important characteristic of this site is the variation of the scale of the fold wavelength. The good agreement between the orientations of the AMS principal axes and the texture principal directions has been shown in Figure 5.25. The texture of phyllosilicates is also governed by the cleavage flattening with maximum eigenvalues sub-parallel to the pole to cleavage. The “textural lineation”, or directions of minimum semiaxes of texture are also sub-parallel to the intersection between cleavage plane and kink plane. This supports the interpreted paramagnetic origin of the measured magnetic lineation: the AMS can be well explained to be originated from LPO of phyllosilicates which are paramagnetic.

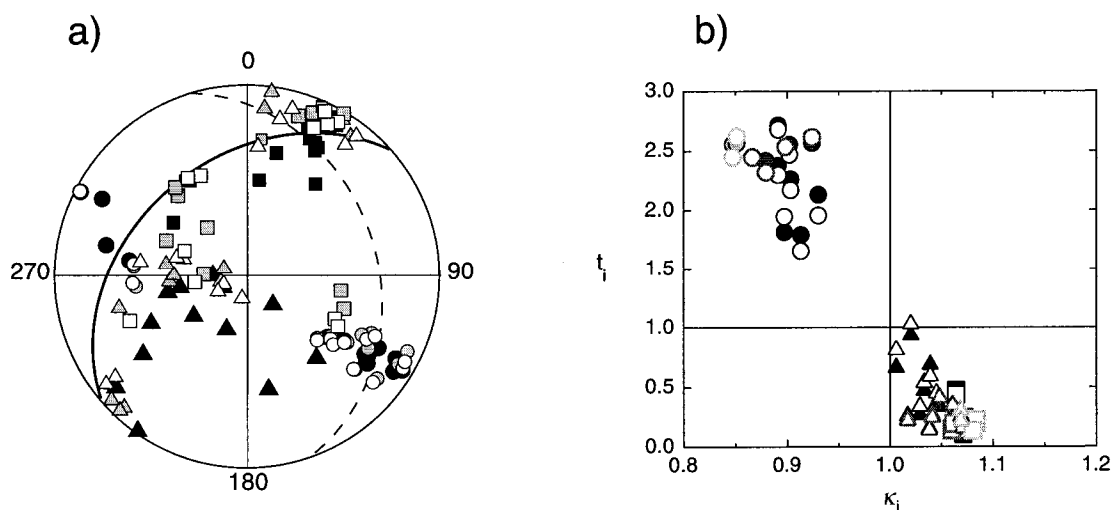


Figure 5.27: a) Comparison between principal axes of AMS and textural ellipsoids at site S37. b) correlation between the normalised eigenvalues AMS and best textural ellipsoid of phyllosilicates.

With respect to the correlation between normalised values of the semiaxes of the AMS and the principal values of the texture tensor eigenvalues it is possible to

identify the three types of behaviour analysed in previous sections (Figure 5.27b). Samples in dark red show that the intermediate and minimum texture principal values are distinct when a magnetic lineation is carried by the phyllosilicates. Although a significant number of samples has not been evaluated from the chevron fold, it is possible to see a trend of decreasing intensity between intermediate and minimum texture eigenvalues. Samples in yellow correspond to those with a well-developed cleavage in which only the maximum principal axes of the texture are distinct.

To verify that LPO of paramagnetic minerals are causing the lineation in the slates, the anisotropy of the paramagnetic fraction was measured on a high-field torque magnetometer. After the separation of the ferrimagnetic and paramagnetic components the paramagnetic anisotropy shows a very good agreement with the low-field measurements (Figure 5.28).

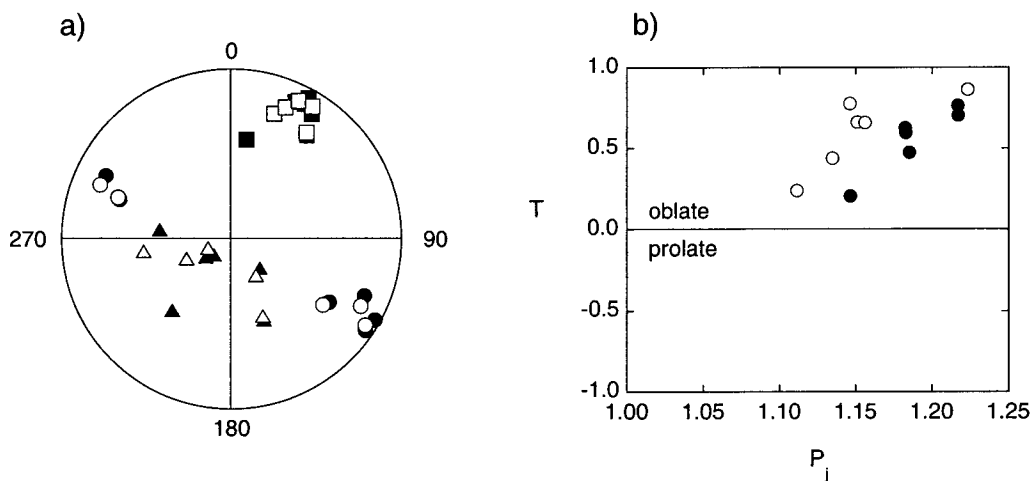


Figure 5.28: Comparison between the low-field AMS (black symbols) and the principal axes of paramagnetic susceptibility from high field torque measurements (open symbols). a) Equal area projection diagram showing the principal axes and b) Jelinek plot.

5.4 Discussion and conclusions

It has been established that in the studied samples the anisotropy of magnetic susceptibility is carried by the LPO of phyllosilicates in the samples, i.e., by mica and chlorite. Since these minerals have a paramagnetic susceptibility and the ferrimagnetic component does not contribute to the magnetic anisotropy it is possible to use low-field magnetic anisotropy measurements for the magnetic fabric of

phyllosilicates. In samples with a significant ferrimagnetic contribution it might be necessary to determine the paramagnetic contribution to the magnetic anisotropy.

The AMS, as well as the fabric of the phyllosilicates are controlled by either one or two main structural features. In the case of slaty cleavage the AMS is governed by the orientation of the cleavage plane with minimum AMS axes and maximum fabric intensity sub-parallel to the pole to cleavage. A minor subdivision along the arc has also been pointed out by Hirt et al. (2000). In the northern part of the slate belt the AMS showed maximum and intermediate axes distributed along a girdle sub-parallel to the cleavage plane. The fabrics of phyllosilicates reveals a compression texture with a high intensity of the pole figure and no preferential direction of the phyllosilicates in the cleavage plane. In the southern part of the arc a distinction between the maximum and intermediate AMS axes can be made. The textures can be identified as “elongate textures” with ellipsoidal pole figure maxima normal to the cleavage plane, less intense pole figures and three distinct principal values of the texture ellipsoid.

In the particular case of sites with slaty cleavage and a well-developed stretching lineation, a magnetic lineation has also been found in the phyllosilicates fabric. Further analysis with low temperature AMS or high-field torque measurements in those samples have confirmed that the paramagnetic susceptibility due to the phyllosilicates carries the magnetic lineation. SEM images show the presence of microkinks in some areas of the plane perpendicular to the stretching lineation. These structures are not found systematically in the plane and are incipient. Therefore microkinks do not fully justify the strong magnetic lineation found and the stretching lineation visible at macroscale.

At the site in which the slaty cleavage has been perturbed by a crenulation cleavage, the AMS is dominated by the two main planes which are the limbs of the kinks. A magnetic lineation has been found along the intersection between the two planes, which corresponds to the minimum direction of the phyllosilicates fabric.

Figure 5.26b summarises the changes in shape and degree of anisotropy of the AMS. The shape of the AMS ellipsoid changes from a medium oblateness to neutral as the angle between the two directions of phyllosilicate c-axes increases. This is a natural example of the model proposed by Housen et al. (1993). They created prolate susceptibility ellipsoid samples by overlapping synthetic planar fabric samples. In our example a progressive change of the shape of the AMS ellipsoid was found from

neutral to oblate with increasing the wavelength of the kinks. The last two cores present typical values of the anisotropy degree for compression textures and an almost perfect oblate shape of the susceptibility ellipsoid. The further development of planar structures shows an increase in the intensity of the maximum semiaxes of the texture at the cost of the intermediate and minimum semiaxes.

Although a geological interpretation is out the aim of this chapter, the obtained results provide useful information about the origin and development of the Asturian Arc. From the two main models which explain the origin of the arc, the oroclinal bending proposed by Ries and Schackleton (1976) can be excluded. If the belt were caused by oroclinal bending then one would expect extensional strain ellipsoids extending along the trend of the outer part of the arc. The inner part would show extension radiating from the core. The fabrics found in the Luarca slates support the model of arc formation by shear zones at the flanks of the arc with no extension in the centre of the arc. The pattern is consistent with models of arc formation proposed by Matte and Ribero (1986). However the possibility of having different textures due to recrystallisation of micas in a strain field or a deformation due to the movement of the arc can not be distinguished.

Seite Leer /
Blank leaf

6. Mathematical simulation of the AMS

AMS measurements have been shown to correlate with crystallographic fabric. In samples, whose magnetic anisotropy is carried by paramagnetic minerals, the preferred orientation of the paramagnetic crystals is responsible for the measured anisotropy. The deformational processes suffered by the rocks play an essential role in the development of fabric and magnetic anisotropy. A mathematical model is presented that simulates the magnetic anisotropy resulting from the mineral texture. The modelling results show how in many cases magnetic fabric can be well determined from mineral fabrics, under a wide range of deformational structures that include slaty cleavage, stretching lineation, crenulation cleavage and kinks with different wavelengths. Comparison of the measured with the simulated AMS is useful in understanding to what extent the method can be applied and what the restrictions are for the interpretation.

Seite Leer /
Blank leaf

6.1 Introduction

The usefulness of AMS as an indicator of rock deformation has been broadly justified since the first works of Graham (1954). The method is fast so that large numbers of samples can be evaluated in a short time. In order to interpret the AMS results, knowledge is required of which minerals carry the magnetic anisotropy and how they are oriented and distributed. The analysis of synthetic samples deformed under controlled conditions helps to understand the mechanisms of fabric formation. In real samples the processes are not as simple and usually not known *a priori*. A mathematical model of the AMS, however, can provide information about the rules that govern the anisotropy of the magnetic susceptibility and can help in understanding the processes that lead to magnetic fabrics.

Owens (1974) established the mathematical basis for modeling magnetic fabrics that are dependent on the preferred orientation of individual grains in the rock. His approach to the problem has been used subsequently by many authors to model the magnetic anisotropy in different materials, e.g. calcite (Owens and Rutter, 1978), shales (Housen et al., 1993) or slates (Housen et al., 1993; Lampert, 1996).

With the application of texture goniometers, which measure the preferred orientation of minerals efficiently and quickly, it is possible to compare a specific mineral fabric with the AMS. Siegesmund et al. (1995) used the harmonic coefficients derived from the pole figure of mica to model the degree of anisotropy and the shape of the AMS ellipsoid in orthogneisses, metagranites and granulites. The components of the magnetic susceptibility ellipsoid are computed as a function of the orientation coefficients. This method has also been applied to a pluton with compositional zoning in order to simulate the magnetic anisotropy (Siegesmund and Becker, 2000).

Hrouda and Schulmann (1990) proposed an inverse method to generate synthetic orientation tensors of the minerals from AMS principal values. The method was extended to compute correlations with deformation in slates (Hrouda et al., 1993).

The following chapter is a further development of the mathematical models presented in previous works, in which the AMS of the samples is not considered to be carried by one single mineral, but at least by two, mica and chlorite. The importance of considering multi-mineral cases is discussed as well as the possibility of including other sources of the magnetic anisotropy in paramagnetic samples. Examples used for

this study come from the Navia-Alto Sil slate belt, which has been described in Chapter 5. The outcrop with kink structures with wavelength between 5 and 100 mm is analyzed to understand the influence of the wavelength of the kinks on the magnetic fabric. This comparison is an example of the limitations of using a bulk property, such as AMS, in the study of samples with inhomogeneous microscale structures.

6.2 Calculation of polycrystal properties

Owens (1974) considered the magnetic susceptibility of a sample, which is due to the preferred orientation of the microcrystals, as a function of the susceptibility of the single crystals that form the sample and their orientation distribution. In crystals with isotropic basal plane it is enough to measure the orientation distribution of the basal plane. Under this condition it is possible to model the studied physical property without the complete orientation distribution.

For a crystal with the basal plane normal the sample direction $\bar{x}(\theta, \varphi)$, the susceptibility tensor in sample coordinates reads $\kappa(\theta, \varphi)$. The total susceptibility κ^{tot} of the sample will be:

$$\kappa^{tot} = \frac{1}{2\pi} \int_{\theta=0}^{\pi/2} \int_{\varphi=0}^{2\pi} P(\theta, \varphi) \kappa(\theta, \varphi) dA(\theta, \varphi) \quad (6.1)$$

where $P(\theta, \varphi)$ is the probability density of a crystal basal pole in the sample direction $\bar{x}(\theta, \varphi)$ given by spherical angles θ and φ and dA is the differential area subtended in this direction. The integration over one hemisphere is enough because both P and κ are symmetric:

The expression for $\kappa(\theta, \varphi)$ is calculated from the single crystal susceptibility by rotations according to the following expression (Figure 6.1):

$$\kappa(\theta, \varphi) = \mathbf{R}^{-1} \kappa(0, 0) \mathbf{R} \quad (6.2)$$

where \mathbf{R} is the rotation matrix to transform the coordinate system ($\mathbf{R}^{-1} = \mathbf{R}^T$).

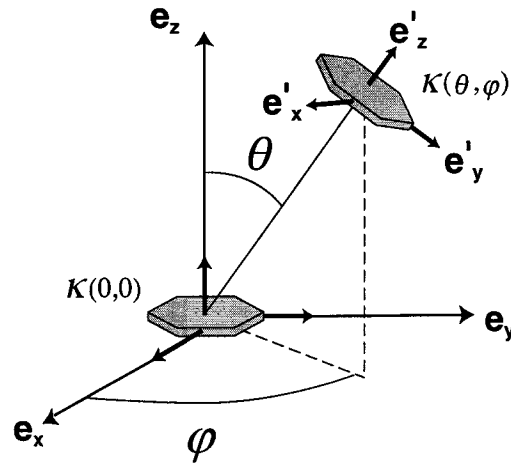


Figure 6.1: Change of coordinates of single crystal properties.

The relationship between the crystal coordinate system (e'_x, e'_y, e'_z) and the sample coordinate system (e_x, e_y, e_z) is given by the following expression:

$$\begin{pmatrix} e'_x \\ e'_y \\ e'_z \end{pmatrix} = \mathbf{R} \begin{pmatrix} e_x \\ e_y \\ e_z \end{pmatrix} \quad (6.3)$$

where \mathbf{R} is the matrix that express the rotation of coordinate system. Substituting \mathbf{R} with its value the expression become:

$$\begin{aligned} \vec{e}'_x &= \cos \theta \cos \varphi \vec{e}_x + \cos \theta \sin \varphi \vec{e}_y - \sin \theta \vec{e}_z \\ \vec{e}'_y &= -\sin \varphi \vec{e}_x + \cos \varphi \vec{e}_y \\ \vec{e}'_z &= \sin \theta \cos \varphi \vec{e}_x + \sin \theta \sin \varphi \vec{e}_y + \cos \theta \vec{e}_z \end{aligned} \quad (6.4)$$

Therefore Eq.(6.2) for the susceptibility in sample coordinates can be written as:

$$\begin{bmatrix} \kappa_{11} & \kappa_{12} & \kappa_{13} \\ \kappa_{12} & \kappa_{22} & \kappa_{23} \\ \kappa_{13} & \kappa_{23} & \kappa_{33} \end{bmatrix} = \begin{bmatrix} \cos \theta \cos \varphi & -\sin \varphi & \sin \theta \cos \varphi \\ \cos \theta \sin \varphi & \cos \varphi & \sin \theta \sin \varphi \\ -\sin \theta & 0 & \cos \theta \end{bmatrix} \begin{bmatrix} \kappa_1 & 0 & 0 \\ 0 & \kappa_2 & 0 \\ 0 & 0 & \kappa_3 \end{bmatrix} \begin{bmatrix} \cos \theta \cos \varphi & \cos \theta \sin \varphi & -\sin \theta \\ -\sin \varphi & \cos \varphi & 0 \\ \sin \theta \cos \varphi & \sin \theta \sin \varphi & \cos \theta \end{bmatrix} \quad (6.5)$$

From goniometry measurements the distribution $P(\theta, \varphi)$ is only available at discrete directions. Therefore, the integral expressed in Eq. (6.1) is approximated by a discrete sum over a finite number of measurements.

$$\kappa^{tot} = \frac{1}{2\pi} \sum_i \sum_j \kappa(\theta_i, \varphi_j) P(\theta_i, \varphi_j) A(\theta_i) \quad (6.6)$$

$A_i(\theta_i)$ is the area on the sphere covered by one measurement interval and depends on the angle θ with the relationship expressed by Eq. (5.6).

When more than one type of crystals are present in the rocks, the calculation is extended to all minerals with the texture measured:

$$\kappa_{polyphase} = \frac{1}{2\pi} \sum_{n=1}^N \sum_i \sum_j \kappa_n(\theta_i, \varphi_j) P_n(\theta_i, \varphi_j) A(\theta_i) V_n \quad (6.7)$$

where N is the total number of considered mineral fabrics and V_n is the volume fraction of mineral n with $\sum_{n=1}^N V_n \leq 1$.

Once the tensor of the polycrystal is calculated the parameters that define the shape and orientation of the synthetic AMS ellipsoid are computed from the principal values and vectors of the tensor.

6.3 Synthetic tests

A synthetic test with the extreme cases of fabric configuration has been done. The inputs of the test are hypothetical pole figures of the phyllosilicate basal planes and the magnetic single crystal properties. The values of single crystal AMS used in this model are calculated from measurements with a high field torque magnetometer. The paramagnetic anisotropy of the crystals has been separated from the ferromagnetic signal of impurities and used as the AMS of crystals (see chapter 4). Table 6.1 summarized the values of the anisotropy of magnetic susceptibility used in this work as well as a selection of the data existing in the literature.

In order to keep the test as simple as possible, the case of only two phyllosilicates has been analyzed. The crystals used were biotite, because with a high degree of

anisotropy compared to muscovite it is easier to visualize the obtained results, and chlorite, which has been identified in the samples by the X-ray diffraction scan (Figure 5.7) and EXD in SEM measurements (Figure 5.8).

Table 6.1: Single crystal properties used for the mathematical models of AMS. Data compiled from Table 4.6, Table 4.9 and Table 4.13. The second column shows the data taken from Borradaile and Werner (1994). Quartz has been considered isotropic, bulk susceptibility of quartz from (Hrouda, 1986). The bulk susceptibility is calculated as

$$\kappa_{bulk} = (2\bar{\kappa}_{basal} + \kappa_3) / 3$$

	this work			Borradaile and Werner (1994)		
	κ_{bulk}	$\bar{\kappa}_{basal}$	κ_3	κ_{bulk}	$\bar{\kappa}_{basal}$	κ_3
biotite	1.250×10^{-3}	1.437×10^{-3}	0.875×10^{-3}	1.159×10^{-3}	1.287×10^{-3}	0.903×10^{-3}
muscovite	2.890×10^{-4}	3.082×10^{-4}	2.506×10^{-4}	2.115×10^{-4}	2.248×10^{-4}	1.848×10^{-4}
chlorite	7.530×10^{-4}	8.076×10^{-4}	6.438×10^{-4}	6.050×10^{-4}	6.460×10^{-4}	5.230×10^{-4}
quartz	-13.3×10^{-6} (Hrouda, 1986)					

Firstly the probability density of a random orientation of phyllosilicates was simulated (Figure 6.2a). The probability density measured with the texture goniometer would be equal to 1 for the two phyllosilicates for any given direction in the hemisphere (Figure 6.2b) The fabric ellipsoid for the two phyllosilicates is isotropic. The eigenvalues of the phyllosilicate fabrics are defined as $t_1 = t_2 = t_3 = 1$ (with the normalization criteria $t_1 + t_2 + t_3 = 3$ established in section 5.4.2). The obtained value of the AMS is also an isotropic ellipsoid. Therefore, there is no anisotropy of the magnetic susceptibility for such a configuration (Figure 6.2c).

A second test was done with an S-fabric (Figure 6.2d). This fabric is characterized by a perfectly planar configuration of the phyllosilicates lying in a plane. The pole figure has only one very intense maximum perpendicular to the preferential plane (Figure 6.2e). The c-axes of all the phyllosilicates are oriented sub-parallel to the pole to cleavage. The fabric ellipsoid degenerates into a line with eigenvalues $t_3 = 3$, $t_2 = t_1 = 0$. As a consequence, the synthetic AMS is a perfectly oblate ellipsoid, whose anisotropy degree ranges between the single crystal values of the considered phyllosilicates (Figure 6.2f).

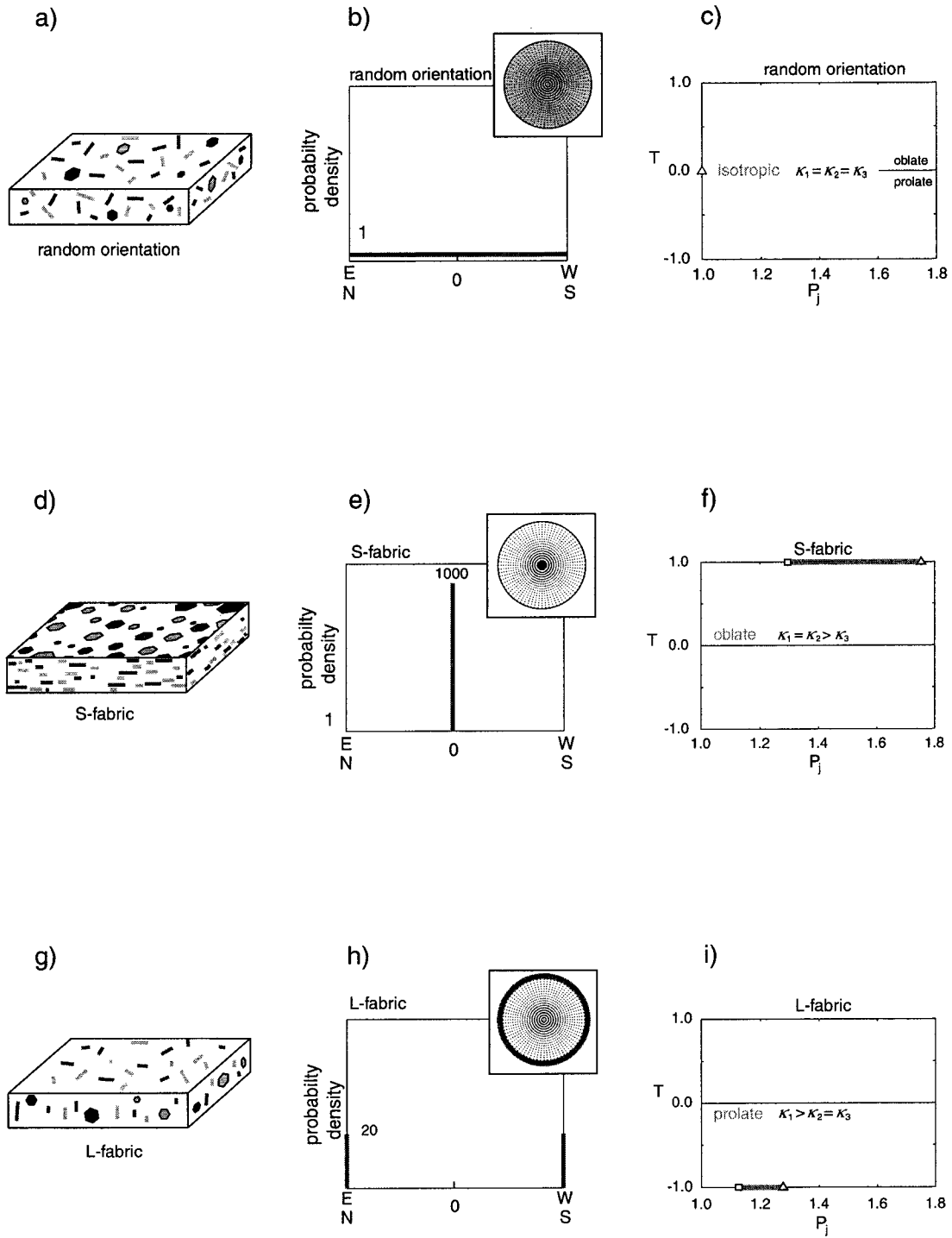


Figure 6.2: Schematic depiction of three extreme cases of fabric orientation, measured probability density and synthetic AMS in a Jelinek plot. In the Jelinek plot, the square represents the simulated AMS with 100% of chlorite in the samples and the triangle with 100% of biotite, in this and subsequent figures.

The final extreme case of fabric is the L-fabric. It is characterized by a distribution of the c-axes of phyllosilicates in a girdle around the equator of the pole figure. Such distribution of the c-axes produces a smaller value of the maximum intensity registered in the texture goniometer compared to the single maximum in the S-fabric. The fabric ellipsoid in this case contains an eigenvalue equal to zero for the center direction, because all the phyllosilicate c-axes are confined in the equator of the figure. The fabric ellipsoid in the case of L-fabric degenerates into a disk. The eigenvalues are therefore $t_3 = t_2 = 3/2$, $t_1 = 0$. This fabric is strongly linear and the simulated AMS produces a perfectly prolate ellipsoid (Figure 6.2i). The anisotropy degree is smaller than the one obtained in S-fabrics.

The range of anisotropy degrees that it is possible to generate with natural samples is strongly related to the type of phyllosilicate. Figure 6.3 shows the different areas of a Jelinek plot that can be reached by the synthetic values of the AMS, depending on the phyllosilicates used for the modeling. The path that follows the AMS generated from an S-fabric to an L-fabric is defined by the texture of the sample.

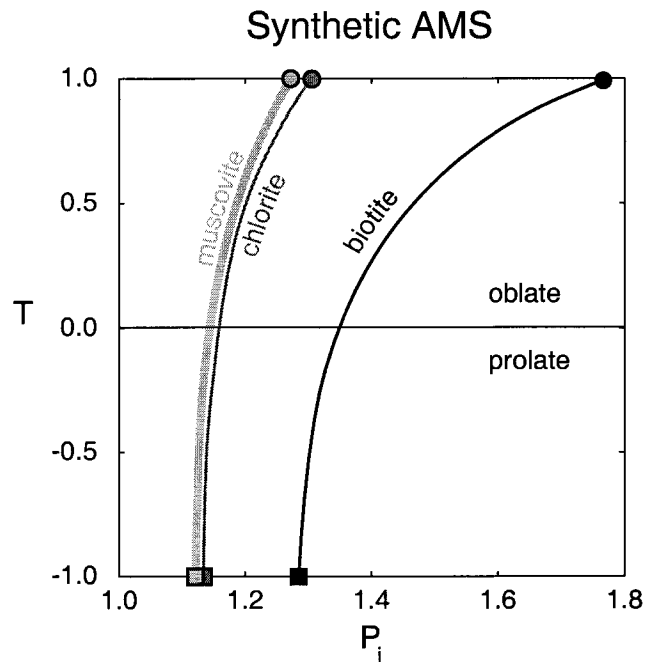


Figure 6.3: Range of anisotropy degrees and shapes of the AMS ellipsoid that can be generated with the proposed model. Circles correspond to the AMS of phyllosilicates with S-fabric and squares to L-fabric. Random fabrics plot at $P_j = 1$ and arbitrary T for all the minerals.

6.4 Input parameters

After identifying the main phyllosilicates present in the studied slates (Figure 5.4, Figure 5.7 and Figure 5.8), the single crystal properties determined by high field torque magnetometry (see chapter 4) were used as an input for the AMS modeling (Table 6.1). The uncertainty in the identification of the type of mica in X-ray diffraction makes a more complete analysis of the composition of the samples necessary. SEM images provide a semiquantitative estimation of the composition. The results of this estimation are summarized in Table 5.1. These percentages are used to assign a single synthetic value of the AMS in the slates, assuming the following compositional relationship:

$$\kappa_{\text{mod}} = 0.31 \times \kappa_{\text{quartz}} + 0.37 \times \kappa_{\text{mu}} + 0.03 \times \kappa_{\text{bio}} + 0.09 \times \kappa_{\text{chl}} \quad (6.8)$$

20% of the composition is not determined. This different oxides and sulfurs such as rutile, magnetite and pyrite and holes in the surface of the sample for SEM, which were pull out in the preparation process. The original grains in these locations could correspond to quartz grains, therefore the quartz content may be underestimated.

In order to provide boundaries to the mathematical simulation of magnetic anisotropy, the evaluated model was done considering 100% of chlorite to 100% of biotite in the samples. This procedure covers the entire range in which the model can be evaluated, since an exact composition of each sample is necessary to simulate a more precise model.

Once the nature of the phyllosilicates is known, it is necessary to justify the need of presenting new AMS values of phyllosilicates. The values that are available in the literature have a large scatter, and some samples show κ_3 subparallel to the basal plane (Borradaile and Werner, 1994). Using the degree of anisotropy available for biotite single crystals (Table 6.1; Borradaile and Werner, 1994) it is not possible to model the high degree of anisotropy found in some samples, even with the unlikely assumption of 100% biotite in the sample (Figure 6.4).

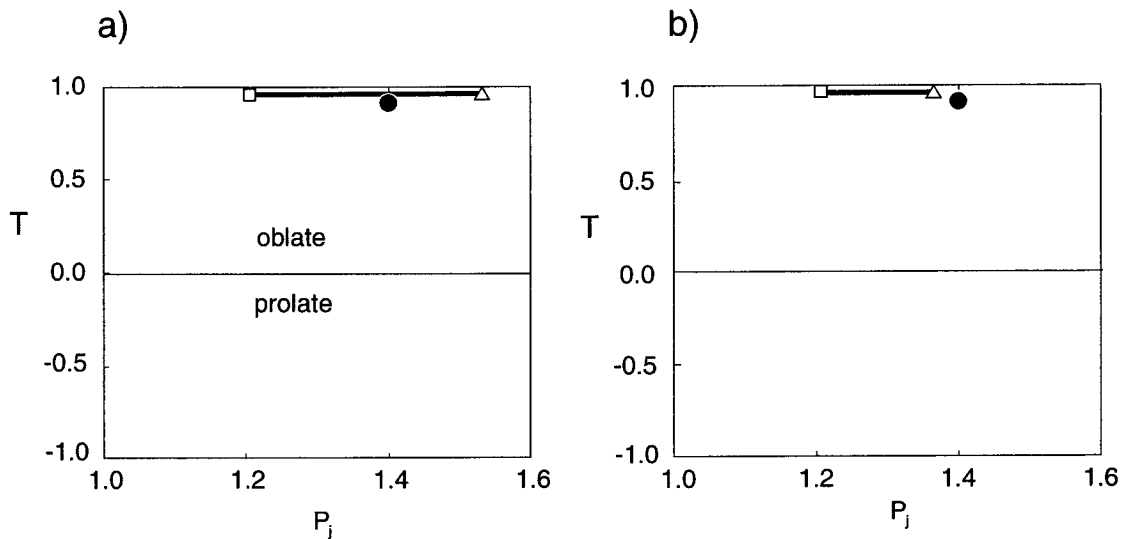


Figure 6.4: Comparison between the AMS simulation in a sample with well-developed slaty cleavage in site S09 using a) single crystal properties presented in this work and b) mean value of the single crystal properties from Borradaile and Werner (1994). Black dot represents the value measured with the KLY-2.

6.5 Simulation applied to slates of the Navia-Alto Sil slate belt

The obtained susceptibility tensor for the samples discussed below is summarised in Appendix E.

6.5.1 Slaty cleavage

Samples with slaty cleavage from the Navia-Alto Sil slate belt have been subdivided into two different sub-categories in the texture fabric analysis. The first sub-category comprises samples that have “compression texture”. They are characterized by a pole figure with nearly axial symmetry, implying no preferential orientation of the phyllosilicates within the cleavage plane. The AMS axes also reflect this absence of preferred orientation in the cleavage plane with maximum and intermediate AMS axes distributed in a girdle sub-parallel to the cleavage plane and with similar maximum and intermediate eigenvalues. Figure 6.5a shows a comparison between the measured AMS principal directions and the mathematical model for one of the sites. Maximum and intermediate axes of the AMS ellipsoid are not well

defined within the cleavage plane, but a very good correlation is found with the minimum susceptibility axes.

The results of the four analyzed samples are summarized in a Jelinek plot in Figure 6.5b. An excellent correspondence is found in the simulation of the shape of the AMS ellipsoid. The anisotropy degree is also well modeled for the assumed composition of slates.

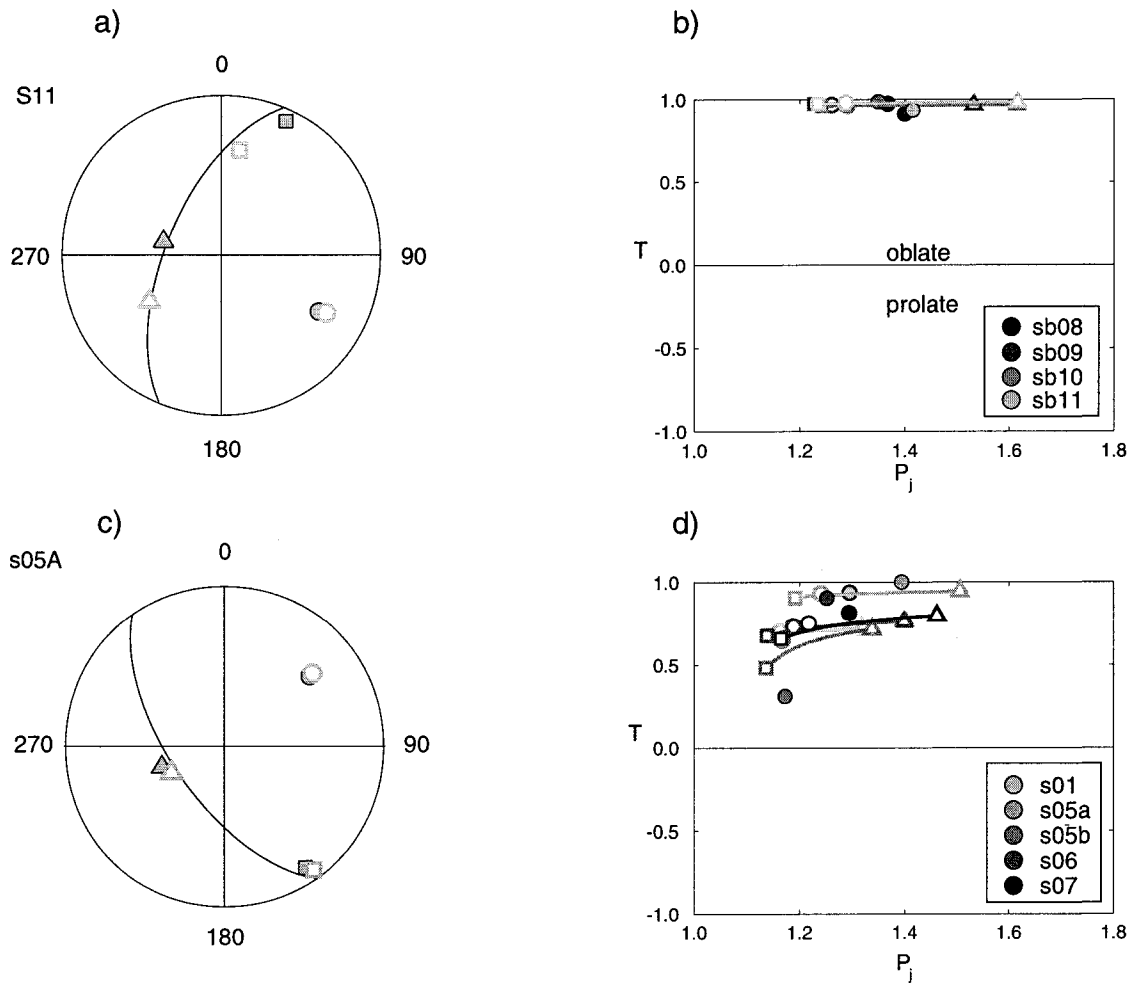


Figure 6.5: Comparison between AMS measurements and synthetic values of the AMS. In the diagrams (a,c) full symbols represent the principal directions of measurements and open symbols represent calculated directions in these and subsequent plots. Great circles represent the orientation of the cleavage plane. In the Jelinek plot full symbols are measurements and open symbols simulated values with the estimated composition. a) Principal AMS axes for one example of "compression textures", b) Jelinek plot for all modelled samples with "compression texture", c) principal AMS axes of one example of "elongated texture" and d) Jelinek plot for all modelled samples with "elongate textures".

The second sub-category includes samples from the southern part of the slate belt. The texture analysis reveals a preferential orientation within the cleavage plane, and is called an "elongate texture". All three axes agree well between measurements and simulation. The minimum direction of the phyllosilicates fabric was found sub-parallel to the magnetic lineation of the samples (Figure 6.5c). There is also a good agreement of the degree of anisotropy that the model reproduces. The shape of the AMS ellipsoid is more problematic. It is not possible to find a good correlation for samples that have $T < 0.6$ in the measured AMS (Figure 6.5d). This problem will be discussed below.

6.5.2 *Stretching lineation*

A stretching lineation within the cleavage plane is present in numerous sites along the Navia-Alto Sil slate belt, two of them have been selected to check the influence of a stretching lineation in the anisotropy of magnetic susceptibility. The pole figures are characterized by a medium intensity with respect to the one found in samples with slaty cleavage, and by elliptical distributions of the density contour lines. In some samples the pole figure can show a girdle distribution (site S04). The magnetic lineation direction was found sub-parallel to the minimum texture direction of the phyllosilicates.

Figure 6.6a shows the good agreement between the orientation of AMS axes and simulated values of the AMS for one of the sites. These results demonstrate that it is possible to generate a synthetic tensor with magnetic lineation from the mineral fabric.

The shape of the obtained ellipsoid, however, does not fit as well with the measured shape of the AMS ellipsoid assuming the composition estimated by means of SEM pictures analysis (Figure 6.6b). But it is possible to see that the model is able to generate a neutral ellipsoid from a single crystal AMS that is oblate, with an appropriate distribution of the phyllosilicates.

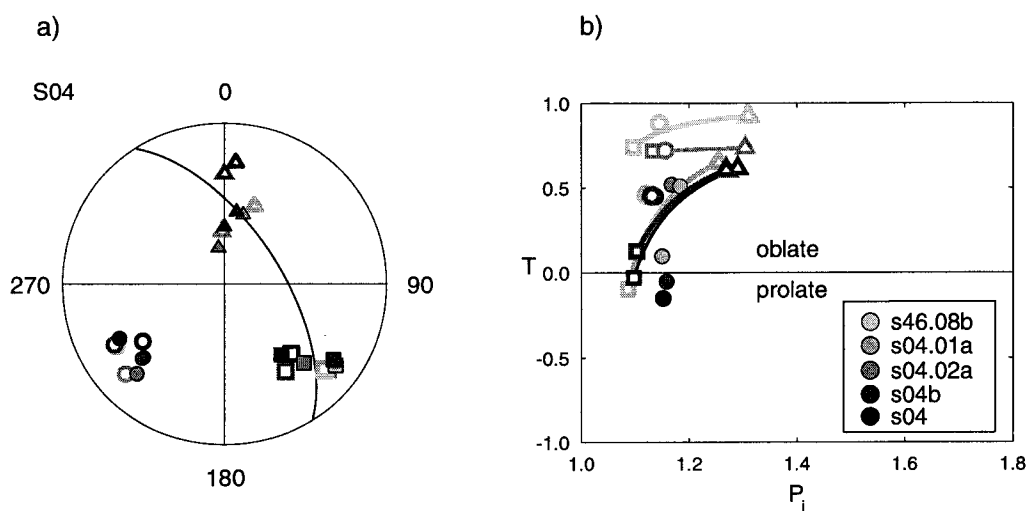


Figure 6.6: Comparison between AMS measurements and synthetic values of the AMS for sites with a well-defined cleavage plane and stretching lineation. AMS principal axes and the corresponding synthetic values for site a) S04 and b) Jelinek plot.

6.5.3 Crenulation cleavage

In samples with a crenulation cleavage overprinting the slaty cleavage, the magnetic lineation was found to be related to the overlapping of two planar fabrics. The maximum susceptibility axes are well grouped in a direction slightly offset with respect to the intersection of the slaty cleavage and crenulation cleavage. There is a good agreement between the orientation of principal axes of the AMS and phyllosilicate fabrics.

The orientation of the synthetic AMS ellipsoid (Figure 6.7a) matches with the measured direction of AMS, confirming the paramagnetic origin of the magnetic lineation. The agreement is also very good in the determination of the shape of the magnetic anisotropy ellipsoid and the anisotropy degree (Figure 6.7b).

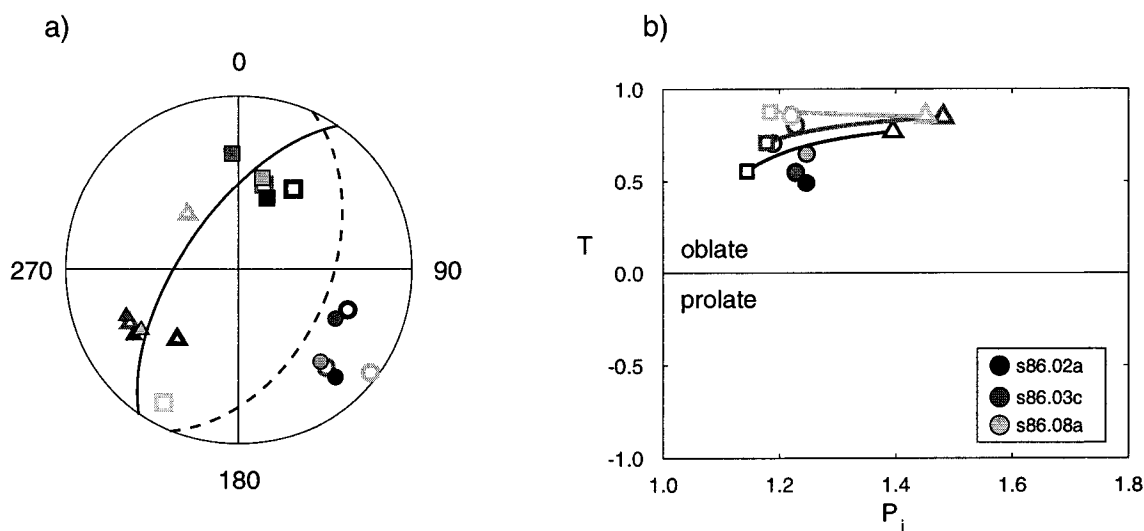


Figure 6.7: Comparison between AMS measurements and synthetic values for site S86 with a well-defined crenulation overprinting the slaty cleavage. Dashed line represents the crenulation cleavage plane and full line the slaty cleavage plane. a) AMS and synthetic AMS principal axes and b) Jelinek plot.

6.5.4 Kink bands

The study of the outcrop containing kink bands with different wavelengths focuses on the effect that the scale of structures has on the AMS. In the first set of samples, the kinks have a wavelength of about 5 mm. The pole figures of phyllosilicate c-axes orientations show two maxima corresponding to the two limbs of the kinks. The AMS minimum axes were found in the great circle that joins both maxima. The simulated AMS tensor shows well-grouped minimum susceptibility directions and reproduces the magnetic lineation measured (Figure 6.8a). The models produce AMS tensors at the lower end of the degree of anisotropy of the samples, although the shape of the ellipsoid tends to be more oblate than the real measurements (Figure 6.8b).

The samples from the second group have a wavelength of about 10 cm forming chevron kinks. The mathematical models show a good agreement of the κ_3 axes. But the general trend of the computed AMS tensor is more scattered (Figure 6.8c). The same result is found in the anisotropy degree and the shape of the AMS tensor presented in a Jelinek plot (Figure 6.8d). The phyllosilicates measured by texture goniometry cover a volume of $20 \times 20 \times 0.1 \text{ mm}^3$, while AMS principal axes represent a bulk property over a sample of 11.4 cm^3 . Therefore the mineral fabric may only reflect part of the texture that a whole sample carries.

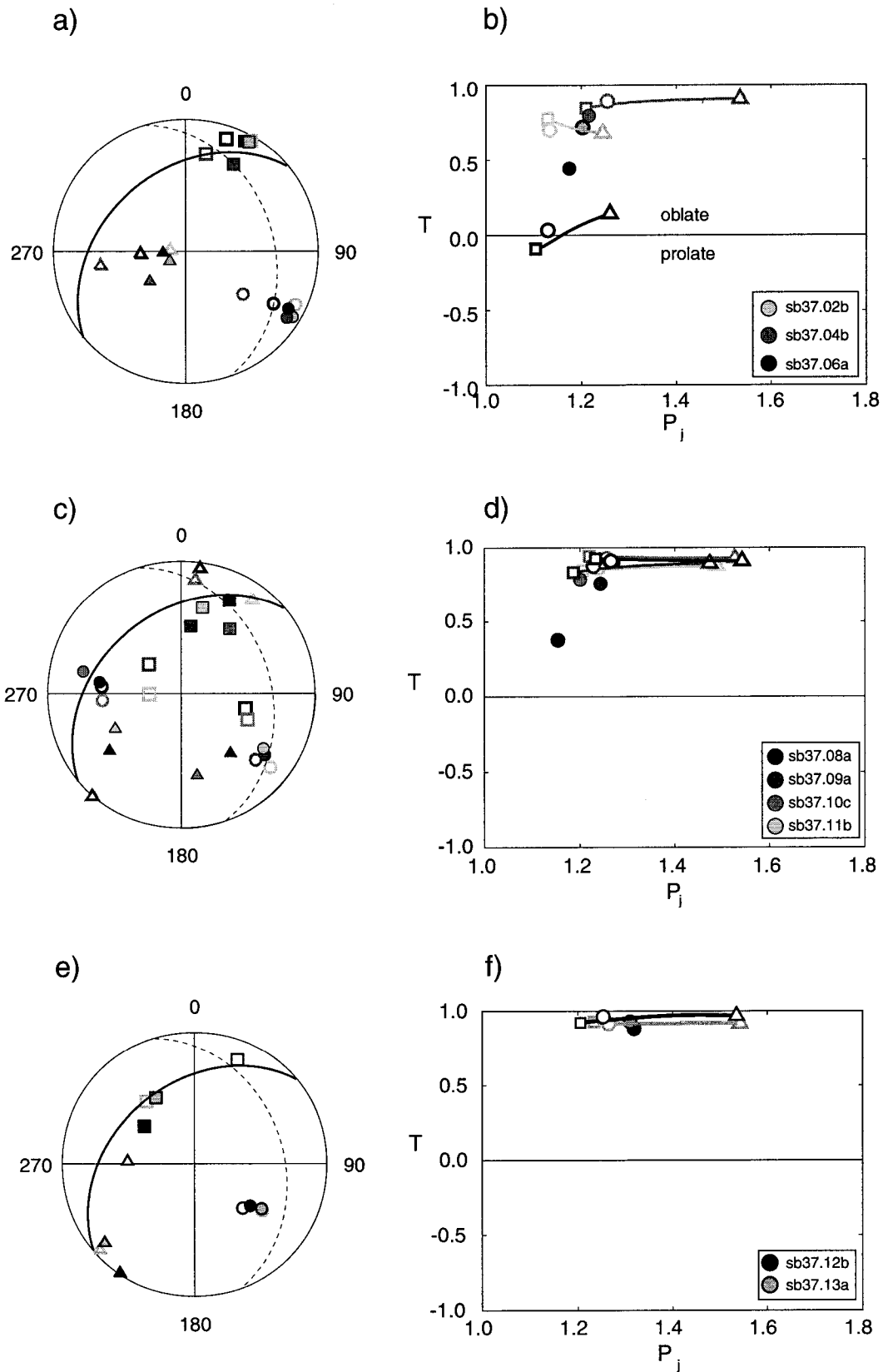


Figure 6.8: Comparison of measured and synthetic AMS parameters in kink bands (site S37). a) and b) Samples with 5mm wavelength (01 to 07) where only every second sample is shown for simplicity, c) and d) samples with 10cm wavelength (08 to 11) and e) and f) samples with slaty cleavage (12 and 13).

Samples from the third area along the outcrop can be considered as samples with a well-developed slaty cleavage. The minimum susceptibility axes are well grouped in both the measured and the synthetic tensor. Maximum and intermediate susceptibility axes lies in a girdle sub-parallel to the slaty cleavage plane (Figure 6.8d). The agreement in the definition of the shape and degree of anisotropy of the simulated tensor is also good (Figure 6.8e).

6.6 Bulk susceptibility

The value obtained for the bulk susceptibility with the presented method is based on the compositional estimation given in Eq. (6.8). The fraction of different minerals is evaluated with the analysis of SEM images. This is a semiquantitative method and the values are subject to changes along the belt. In the estimation, there is a high degree of undetermined minerals that can be quartz grains pull out in the polishing process, therefore the quartz content can be underestimated. The magnetic susceptibility of ferromagnetic minerals or oxides has not been considered. This is a possible reason why the estimated bulk does not exactly correspond with the measurements. Figure 6.9 illustrates the ranges of magnetic susceptibility in which the measured samples lie. For a further interpretation of the obtained bulk susceptibility a quantitative composition analysis of the sample is required.

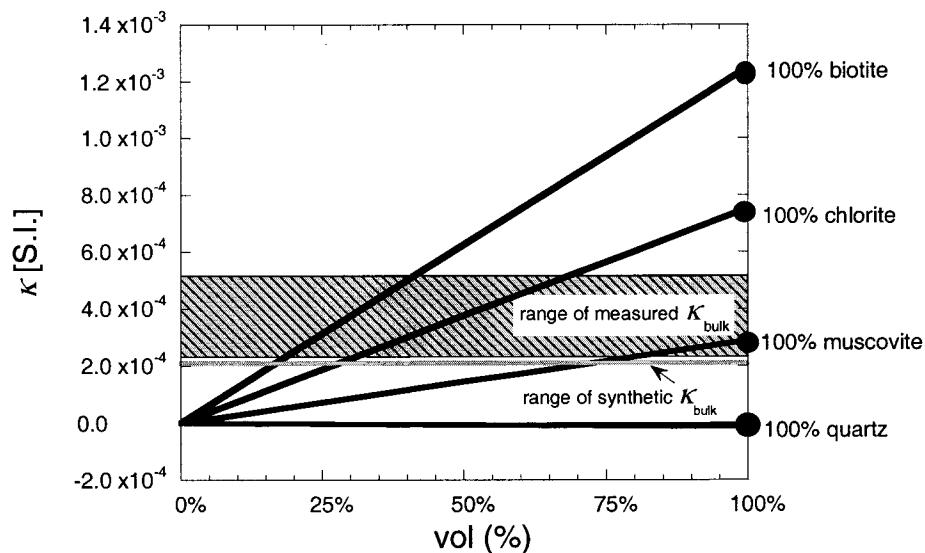


Figure 6.9: Relationship between the bulk susceptibility of the single crystals and the measured low-field bulk susceptibility of the samples.

Figure 6.9 also gives a boundary for the bulk susceptibility of the samples to be analyzed in terms of magnetic anisotropy. Samples with a bulk susceptibility above the higher limit are suspected to contain significant amounts of ferromagnetic minerals, which may contribute to the magnetic anisotropy.

6.7 Discussion and conclusions

The AMS in deformed polyphase slates has been successfully modeled based on the preferred orientation of phyllosilicates. The proposed method provides a good agreement between measurements and simulations for the orientation of the principal axes and the shape of the susceptibility ellipsoid. The model reproduces satisfactorily the presence of a magnetic lineation in samples in which overlapping deformation phases are present. This confirms the possibility of having a paramagnetic lineation in samples that are rich in phyllosilicates.

The principal directions of the AMS are well determined in samples with a well-defined cleavage. In samples with kink structures and crenulation cleavage the agreement between measured AMS and simulated directions is very good. The correlation has been found to be good also in presence of a stretching lineation in the cleavage plane. In the case of samples with "compression textures" the minimum susceptibility axes were well-modeled, but not intermediate and maximum axes, distributed in a girdle in the cleavage plane with very similar eigenvalues.

On the other hand, the shape and degree of anisotropy of the AMS ellipsoid was best modeled in samples with a well developed cleavage. The presence of a secondary plane, or two main planes in the orientation of the phyllosilicates (crenulation cleavage or kink structures), gives a weaker agreement of the simulated shape ellipsoid, with respect to the measurements. The presence of neutral AMS ellipsoids, at sites with stretching lineation, was also successfully modeled. It confirms the possibility of having a paramagnetic lineation as well as prolate AMS ellipsoids in samples with anisotropy carried by paramagnetic minerals with oblate single crystal susceptibility.

It is necessary, however, to examine carefully the dimension of the structures present in the samples. The preferred orientation measured by texture goniometry involves a volume of 40 mm^3 while the AMS is a bulk property that is averaged over

a volume of 11.4 cm^3 . For this reason, it is possible to model satisfactory the AMS principal directions in structures of several millimeters of wavelength, i.e., crenulation cleavage or millimeter kinks, or in cases of homogeneous deformation, i.e., slaty cleavage. The directions are more scattered in the samples where the preferred orientation of phyllosilicate in the analyzed surface may not be not representative of the orientation of minerals in the whole sample.

Finally, it is important to highlight that this is possibly the simplest simulation that can be done in polyphase samples, a more sophisticated model requires additional measurements about the composition of the samples and the texture of all the minerals.

Seite Leer /
Blank leaf

7. Summary and conclusions

Seite Leer /
Blank leaf

The main focus of this thesis was to investigate the contribution of different rock-forming minerals to the anisotropy of magnetic susceptibility in natural samples. Magnetic anisotropy arises from the preferential distribution of a magnetic property (e.g., susceptibility) within a rock. This is usually related to the preferential orientation of the mineral constituents. When the fabric is controlled by paramagnetic minerals the observed anisotropy is due to a combination of two effects: the intrinsic anisotropy of the paramagnetic minerals and their anisotropic distribution. Part of this doctoral research project involved defining the intrinsic anisotropy of the common phyllosilicates: biotite, muscovite and chlorite. In a further part, mineral fabrics were defined by texture goniometry on slates from the Navia-Alto Sil slate belt in northern Spain. The magnetic anisotropy of the slates is mostly controlled by paramagnetic phases. The origin of the magnetic fabric in the slates was then modeled using information on the orientation of the chlorite and mica. The combination of the intrinsic anisotropy of individual mineral component and their respective distributions contributes to a better understanding of the factors that are important in defining the magnetic anisotropy. This understanding is necessary so that magnetic fabrics can be used as indicators of deformation in rocks.

7.1 Separation of the paramagnetic and ferromagnetic components to the anisotropy of magnetic susceptibility

Phyllosilicates magnetic properties that are available in the literature show a large variability due to difficulties in isolating the signal of the crystal from that of ferromagnetic impurities. A mathematical method was developed that separates the two components of the magnetic anisotropy using measurements from a high-field torque magnetometer. The method has been found useful in samples where the ferromagnetic component saturates in the applied high fields. Measurement time is long and a compromise between the error in the measurements and their duration was obtained by using a total of four fields above the saturation of the ferromagnetic phases. The selection of the applied fields must be made with additional information about the rock-magnetic properties of the ferromagnetic minerals in the sample. Using fields below the saturation of the ferromagnetic phases may lead to an overestimation of the paramagnetic fraction.

Measurements with torque magnetometers only provide information about the deviatoric tensor that defines the anisotropy of magnetic susceptibility. Therefore it is necessary to have additional measurements that supply a value for the bulk susceptibility in order to compute the full magnetic anisotropy tensor for both the ferromagnetic and the paramagnetic fractions. The principal directions of the anisotropy of magnetic susceptibility (AMS) of both fractions, however, can be obtained directly. The measurement accuracy of this instrument was tested with samples with a known orientation of the magnetic susceptibility ellipsoid. The differences between maximum and minimum principal axes of magnetic susceptibility in three types of phyllosilicates have been evaluated with the high-field torque magnetometer and from the paramagnetic susceptibility calculated from hysteresis loops along known crystallographic directions. The differences in magnetic susceptibility with the two methods were very similar.

The separation of magnetic components has been successfully tested in three different rock types (granites, peridotites and serpentinites) from a highly deformed area in the Betic Cordillera in northern Spain. The three lithologies present three different magnetic behaviours, consisting of anisotropy dominated by the paramagnetic component in the granites, a mainly ferromagnetic fabric in the serpentinites and a ferromagnetic/paramagnetic mixed fabric in peridotites.

7.2 Results of the anisotropy of magnetic susceptibility in biotite, muscovite and chlorite

The separation method has been applied to three different phyllosilicate minerals (biotite, muscovite and chlorite) in order to determine their magnetic anisotropy parameters. The obtained values are better constrained than those reported in previous investigations.

- *Biotite*

The shape of the magnetic anisotropy ellipsoid of biotite has found to be almost perfectly oblate with a shape parameter $T = 0.9 \pm 0.2$. The magnetic anisotropy within the basal plane measured under room temperature conditions confirms this result. The crystallographic axes govern the principal directions of magnetic susceptibility with

the minimum axis normal to the basal plane (001). The degree of anisotropy, $P_j = 1.78 \pm 0.14$, is higher than previously reported values. This value was independently confirmed from determination of the paramagnetic susceptibility along the crystallographic axes from the high-field parts of hysteresis curves. The difference between the measured values and values in the literature indicates how ferromagnetic inclusions can affect the magnetic anisotropy. A detailed analysis of the magnetic remanence reveals that magnetite is the main ferromagnetic contaminant present in biotites, although its presence was not significant in the AMS.

- *Muscovite*

The principal directions of magnetic anisotropy of muscovite are determined by the crystallographic axes of the crystal. The lower value of the bulk susceptibility makes it more difficult to analyze any anisotropy in the basal plane, but the highly oblate shape of the AMS ellipsoid, with $T = 0.8 \pm 0.3$, suggests that the mineral cleavage plane can be considered isotropic with the considered error. The separation of the magnetic components was successful and no general fabric has been found in the orientation of the ferromagnetic fraction. The average degree of anisotropy for the nine specimens from three different crystals is $P_j = 1.28 \pm 0.11$. This value of P_j is slightly higher than values reported in the literature and T is much more oblate than previously reported values.

- *Chlorite*

The anisotropy of the paramagnetic fraction in chlorites was also controlled by the orientation of the crystallographic axes. The shape of the paramagnetic anisotropy ellipsoid was almost oblate with well-constrained values value of $T = 0.3 \pm 0.7$ (Borradaile and Werner, 1994). In the case of chlorite crystals, the separation method was very important because a larger number of samples contained a significant ferromagnetic fraction. The ferromagnetic fraction showed neither a common orientation relative to crystallographic axes nor a consistent shape of the ellipsoid. This suggests that the grain size and the orientation of the ferromagnetic phases is determined by the history of the crystal and not by its crystallography.

The minimum susceptibility axis is sub-parallel to the pole to the basal plane of the crystals for all the specimens. This is in contrast with the existing values, which have shown samples with minimum susceptibility axes in the basal plane.

7.3 Analysis of fabric in natural samples

The analysis of texture and magnetic fabrics in the selected natural samples shows the limitations and advantages of both methods and investigates the origin of magnetic anisotropy in samples controlled by paramagnetic minerals. Samples are Ordovician black roof slates from the Luarca formation, in Northern Spain.

Where the cleavage plane is well-defined, it is the main feature that controls both mineral texture, defined by chlorite and mica, and principal directions of the AMS ellipsoid. The maximum intensity of the pole figure and the minimum axes of the magnetic susceptibility ellipsoid are sub-parallel to the pole to cleavage. At the site in which the slaty cleavage has been perturbed by a crenulation cleavage, the AMS is a composite fabric due to the two limbs of the crenulation. A magnetic lineation has been found sub-parallel to the intersection between the two planes; this corresponds to the minimum direction of the phyllosilicates fabric. Similar behaviour has been observed in samples with kink structures, which show a magnetic lineation in the direction of intersection of the two limbs. Problems arise when the dimension of the kinks is larger than the area measured by texture goniometry, but smaller than a mean standard sample for AMS. In this case the texture goniometer only records the orientation of a single limb whereas the AMS averages over a larger volume that includes both limbs. A magnetic lineation of paramagnetic origin may arise along the intersection plane of the two limbs of the kinks or the intersection of the cleavage plane with the crenulation plane.

In their tectonic context, the results provide constraints on the formation of the Asturian Arc. The pole figures from samples in the northern part of the arc show a point maxima with axial symmetry within the cleavage plane. In the southern part the probability density of phyllosilicates has lower intensity and an elliptical shape. The presence of two different features of the pole figure in samples with well-developed cleavage implies that the origin of the Asturian Arc can not be oroclinal bending, as

has been postulated by Ries and Schackleton (1976) and Parés et al. (1996). The texture pattern has heterogeneity along the belt, thus excluding oroclinal bending.

7.4 Mathematical simulation of the AMS

The AMS has been successfully modeled in samples that have undergone different deformations. The models are able to simulate not only the shape and degree of anisotropy of the magnetic ellipsoid, but also the directions of the principal axes of the AMS ellipsoid. It must be noted that the AMS can only be simulated when the texture and magnetic fabrics are averaged over the same scale of structure. It has been possible to evaluate the range of anisotropy degree and shape of the magnetic ellipsoid in natural samples that are composed of mica and chlorite.

Although a unique solution is not possible, the modeling provides boundaries to the contributions of the two paramagnetic minerals to the total AMS.

7.5 Outlook

The success obtained in the separation of the paramagnetic and ferromagnetic components of the magnetic anisotropy makes high-field torque magnetometry the most suitable method for the analysis of single crystal properties. The study should be extended to other minerals in the mica series, but also to pyroxene, amphiboles, feldspars, carbonates and quartz. The physical principle on which the separation is based can also be applied to diamagnetic minerals and therefore a reliable value of the magnetic anisotropy of quartz or calcite could be determined.

The susceptibility and degree of anisotropy have been shown to be dependent on the Fe^{2+} and Fe^{3+} content in the biotite crystals. This dependency has implications for the correlation of the AMS with strain. Further investigation of other minerals is necessary to evaluate the broader implications of this observation.

The mathematical simulation of AMS presented in this thesis answers some questions about the origin of magnetic anisotropy in paramagnetic samples. It can be extended to samples with more than two mineral components, which could improve the modeling of the bulk susceptibility.

With electron back-scattered diffraction it is now possible to obtain lattice-preferred orientation of the main mineral constituents in a rock, including the ferromagnetic fraction. Further modeling on synthetic and natural samples with this information could deliver a complete model of the magnetic anisotropy in a rock, as long as the single mineral properties are also well-known. A complete understanding of how magnetic anisotropy arises would allow for a better evaluation of the limits and conditions for quantitative correlations between the AMS and finite strain.

Appendix

Seite Leer /
Blank leaf

APPENDIX A: Main formulas that relate the principal directions expressed in geographic coordinates with their expression in terms of declination and inclination:

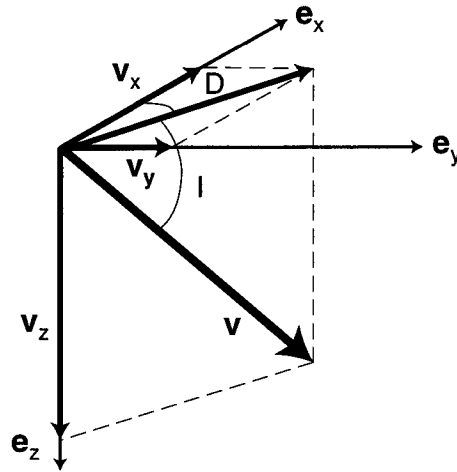


Fig. A: Relation between declination and inclination and the corresponding components in the coordinate system.

For a generic vector \mathbf{v} , the equation that relates the two notations is given by:

$$\begin{aligned} v_x &= \|\mathbf{v}\| \cos D \cos I \\ v_y &= \|\mathbf{v}\| \sin D \cos I \\ v_z &= \|\mathbf{v}\| \sin I \end{aligned} \quad (8.1)$$

In the case of the texture ellipsoid, the relation between the declination and inclination of the eigenvalues and the angles θ and φ in Eq. (5.3) is:

$$\begin{aligned} D &= \varphi \\ I &= 90 - \theta \end{aligned} \quad (8.2)$$

Appendix

APPENDIX B: Main AMS parameters for the selection of samples measured with texture goniometer.

The orientation of the principal axes is expressed in geographic coordinates; the same orientation is used in subsequent tables.

sample	κ^{LF} [S.I.]	κ_1^{AMS}	D_1^{AMS}	I_1^{AMS}	κ_2^{AMS}	D_2^{AMS}	I_2^{AMS}	κ_3^{AMS}	D_3^{AMS}	I_3^{AMS}	P_i^{AMS}	T^{AMS}
s01	3.887×10^{-4}	1.075	98.2	13.2	1.068	310.9	74.5	0.857	190.0	8.1	1.29	0.94
s04.01a	3.372×10^{-4}	1.068	126.3	16.4	1.003	14.1	52.0	0.929	227.5	33.2	1.15	0.10
s04.02a	4.841×10^{-4}	1.061	124.9	19.5	1.025	8.8	51.1	0.914	227.8	32.1	1.17	0.53
s04	3.080×10^{-4}	1.075	134.9	31.7	0.991	350.3	70.3	0.934	224.3	23.7	1.15	-0.15
s04b	3.747×10^{-4}	1.076	141.5	43.7	0.996	359.5	59.5	0.928	242.7	28.0	1.16	-0.05
s05a	2.960×10^{-4}	1.091	146.8	10.0	1.091	252.3	56.6	0.818	50.6	31.5	1.39	1.00
s05b	3.040×10^{-4}	1.070	137.9	31.9	1.014	287.1	54.1	0.915	38.5	14.8	1.17	0.31
s06	5.167×10^{-4}	1.064	306.3	32.7	1.064	180.0	42.6	0.872	57.9	30.0	1.26	1.00
s07	4.213×10^{-4}	1.072	226.7	65.3	1.053	2.6	18.4	0.875	98.0	16.1	1.25	0.82
s08	5.280×10^{-4}	1.088	10.6	27.2	1.084	225.1	58.0	0.828	108.8	15.5	1.37	0.97
s09	2.800×10^{-4}	1.099	308.2	58.4	1.085	213.9	2.6	0.816	122.4	31.4	1.40	0.91
s10	5.280×10^{-4}	1.083	27.6	45.9	1.081	225.7	42.7	0.835	127.1	9.2	1.35	0.99
s11	2.800×10^{-4}	1.100	26.0	7.3	1.089	283.7	59.4	0.811	120.2	29.6	1.41	0.94
s37.01a	3.058×10^{-4}	1.064	33.5	16.5	1.033	186.6	71.6	0.903	301.2	7.9	1.19	0.65
s37.02b	3.180×10^{-4}	1.064	30.6	9.0	1.039	245.3	79.1	0.897	121.5	6.1	1.20	0.72
s37.03a	3.910×10^{-4}	1.071	24.4	21.8	1.038	258.5	55.7	0.891	125.2	25.1	1.22	0.66
s37.04b	4.152×10^{-4}	1.069	28.4	26.1	1.029	232.4	61.9	0.902	123.3	9.9	1.19	0.55
s37.05a	3.691×10^{-4}	1.064	21.9	15.9	1.045	260.6	61.4	0.891	118.9	23.1	1.22	0.79
s37.06a	3.958×10^{-4}	1.067	27.9	6.3	1.020	271.7	76.0	0.913	119.3	12.5	1.17	0.42
s37.07d	2.313×10^{-4}	1.064	29.9	5.0	1.006	137.4	73.5	0.930	298.5	15.6	1.15	0.17
s37.08a	3.534×10^{-4}	1.060	27.0	22.5	1.017	139.8	43.2	0.924	277.9	38.4	1.15	0.39
s37.09a	3.913×10^{-4}	1.073	7.7	47.6	1.048	232.7	32.9	0.879	126.2	23.6	1.24	0.76
s37.10c	3.195×10^{-4}	1.062	36.4	39.4	1.041	169.0	39.5	0.898	282.8	26.0	1.20	0.77
s37.11b	3.459×10^{-4}	1.072	13.6	33.8	1.061	243.5	43.9	0.866	123.7	27.3	1.27	0.90
s37.12b	3.208×10^{-4}	1.084	306.9	50.9	1.069	215.0	1.5	0.847	123.8	39.0	1.32	0.89
s37.13a	3.281×10^{-4}	1.080	330.0	41.4	1.069	229.5	11.5	0.851	127.2	46.2	1.31	0.91
s46.08b	3.390×10^{-4}	1.067	307.4	0.3	1.025	38.0	61.4	0.907	217.2	28.5	1.18	0.51
s86.02a	3.850×10^{-4}	1.089	21.3	53.8	1.031	238.9	30.0	0.880	138.0	18.1	1.25	0.49
s86.03c	3.638×10^{-4}	1.080	14.2	44.2	1.032	248.6	30.9	0.888	138.4	30.0	1.23	0.54
s86.08a	3.918×10^{-4}	1.080	356.5	33.3	1.042	239.4	34.8	0.877	116.9	37.7	1.25	0.66

Appendix

APPENDIX C: Principal axes and orientation of the mica fabric ellipsoid determined from texture analysis.

sample	t_3^{mica}	D_3^{mica}	l_3^{mica}	t_2^{mica}	D_2^{mica}	l_2^{mica}	t_1^{mica}	D_1^{mica}	l_1^{mica}
s01	2.023	275.7	9.1	0.619	310.9	78.9	0.358	96.7	6.3
s04.01a	1.841	234.9	18.6	0.712	19.3	45.7	0.447	129.5	38.4
s04.02a	1.986	227.4	18.8	0.624	356.3	61.6	0.390	130.1	20.6
s04	1.939	240.0	29.3	0.697	2.9	50.2	0.364	135.4	24.3
s04b	1.886	234.6	18.2	0.716	17.4	52.7	0.399	133.0	31.3
s05a	2.490	50.8	6.7	0.293	246.4	59.9	0.217	144.6	29.2
s05b	2.072	38.3	14.0	0.604	259.7	67.6	0.324	132.8	17.2
s06	2.233	56.2	31.0	0.518	214.6	57.1	0.249	320.2	9.9
s07	2.384	228.3	63.8	0.438	359.4	18.0	0.178	95.5	18.5
s08	2.723	113.4	15.3	0.153	219.5	45.2	0.124	9.7	40.7
s09	2.548	115.6	30.0	0.249	212.5	11.9	0.203	321.6	57.3
s10	2.721	124.4	8.7	0.166	215.3	5.3	0.113	336.6	79.7
s11	2.723	118.6	25.3	0.153	233.1	41.2	0.124	6.7	38.3
s37.01a	2.262	115.9	9.0	0.490	257.5	78.5	0.248	24.8	7.0
s37.02b	1.817	120.9	10.1	0.708	287.9	79.6	0.475	30.5	2.2
s37.03a	2.715	126.5	45.4	0.177	223.0	6.4	0.108	319.2	43.9
s37.04b	2.553	129.1	44.3	0.289	255.8	31.5	0.158	5.8	29.2
s37.05a	2.375	115.5	29.8	0.385	265.9	56.6	0.240	17.5	13.7
s37.06a	1.792	121.7	27.6	0.956	270.6	58.6	0.252	24.2	13.5
s37.07d	2.133	118.0	33.6	0.684	278.3	54.8	0.183	21.7	9.4
s37.08a	2.568	274.6	40.3	0.281	6.7	2.4	0.151	99.6	49.6
s37.09a	2.417	131.6	26.5	0.359	223.4	3.5	0.224	320.5	63.2
s37.10c	2.536	264.3	41.1	0.282	5.8	12.9	0.182	109.6	46.1
s37.11b	2.450	129.0	14.9	0.356	36.2	10.6	0.194	271.9	71.5
s37.12b	2.554	124.4	37.7	0.245	30.3	5.2	0.201	293.6	51.9
s37.13a	2.569	132.6	49.6	0.275	227.5	4.2	0.156	321.0	40.2
s46.08b	2.007	213.9	27.0	0.529	41.3	62.7	0.464	305.4	3.0
s86.02a	2.224	127.4	3.6	0.516	221.6	49.1	0.260	34.4	40.6
s86.03c	2.433	137.6	25.6	0.383	243.6	29.8	0.184	14.4	48.7
s86.08a	2.363	109.9	33.7	0.409	322.8	51.5	0.228	211.2	16.3

Appendix

APPENDIX D: Principal axes and orientation of the chlorite fabric ellipsoid determined from texture analysis.

sample	t_3^{ch}	D_3^{ch}	l_3^{ch}	t_2^{ch}	D_2^{ch}	l_2^{ch}	t_1^{ch}	D_1^{ch}	l_1^{ch}
s01	2.009	188.0	7.0	0.637	6.5	83.0	0.354	98.0	0.2
s04.01a	1.555	235.0	38.4	1.044	20.4	45.9	0.401	130.1	18.0
s04.02a	1.967	228.6	18.2	0.633	359.8	63.4	0.400	132.3	18.6
s04a	1.635	240.5	33.0	1.022	358.4	48.2	0.343	134.8	22.7
s04b	1.700	219.7	36.8	0.954	11.6	49.6	0.346	118.9	14.1
s05a	2.362	49.9	29.8	0.371	237.8	60.0	0.267	141.8	3.5
s05b	1.967	37.2	12.8	0.744	285.0	59.0	0.289	134.0	27.7
s06	1.998	58.0	33.3	0.640	220.9	55.5	0.362	322.7	8.0
s07	2.169	97.3	20.2	0.590	359.5	20.4	0.241	228.1	60.7
s08	2.621	115.0	15.5	0.208	236.3	61.9	0.171	18.3	22.8
s09	2.579	115.9	29.3	0.228	206.8	1.7	0.193	300.0	60.6
s10	2.663	125.1	9.3	0.197	215.8	3.7	0.140	327.3	80.0
s11	2.621	120.4	25.5	0.208	253.4	55.1	0.171	19.2	22.2
s37.01a	2.171	296.9	2.4	0.558	193.4	80.1	0.271	27.3	9.6
s37.02b	1.949	121.2	6.8	0.613	250.8	79.4	0.438	30.2	8.0
s37.03a	2.681	128.1	44.8	0.160	232.4	14.0	0.159	335.2	41.8
s37.04b	2.470	129.6	42.2	0.359	277.5	43.1	0.171	23.8	16.7
s37.05a	2.299	116.0	27.5	0.469	284.9	62.0	0.232	23.6	4.6
s37.06a	1.657	119.2	7.6	1.053	241.5	75.9	0.290	27.6	11.8
s37.07d	1.957	118.7	30.5	0.835	284.8	58.7	0.208	25.0	6.1
s37.08a	2.615	275.8	40.1	0.242	14.9	10.7	0.143	117.0	48.0
s37.09a	2.323	132.0	27.2	0.431	37.6	8.5	0.246	291.7	61.2
s37.10c	2.536	266.1	39.8	0.268	11.6	17.5	0.196	120.0	45.2
s37.11b	2.448	130.9	15.4	0.368	36.4	15.9	0.184	262.6	67.6
s37.12b	2.448	125.3	38.6	0.322	4.6	32.6	0.230	248.6	34.4
s37.13a	2.620	133.6	49.0	0.238	232.4	7.6	0.142	328.8	40.0
s46.08b	1.723	215.0	29.2	0.717	47.6	60.2	0.560	308.1	5.5
s86.02a	2.029	130.7	7.3	0.689	226.9	40.4	0.282	32.4	48.7
s86.03c	2.262	140.0	26.2	0.527	248.8	33.2	0.211	20.2	45.3
s86.08a	2.311	111.9	32.7	0.411	292.3	57.3	0.278	202.1	0.2

Appendix

APPENDIX E: Principal axes and orientation of the synthetic AMS ellipsoid.

sample	κ^{mod} [S.I.]	κ_1^{mod}	D_1^{mod}	I_1^{mod}	κ_2^{mod}	D_2^{mod}	I_2^{mod}	κ_3^{mod}	D_3^{mod}	I_3^{mod}	P_j^{mod}	T^{mod}
s01	2.06×10^{-4}	1.053	96.3	6.9	1.031	319.4	80.5	0.916	187.0	6.5	1.16	0.70
s04.01a	2.07×10^{-4}	1.047	129.8	18.3	1.016	19.8	45.9	0.937	235.0	38.5	1.12	0.46
s04.02a	2.08×10^{-4}	1.050	130.7	20.1	1.031	357.1	62.0	0.919	227.7	18.6	1.16	0.72
s04a	2.06×10^{-4}	1.053	136.4	49.4	1.017	359.8	30.6	0.930	240.1	24.0	1.14	0.45
s04b	2.06×10^{-4}	1.050	145.2	55.2	1.017	5.0	23.9	0.932	241.2	23.6	1.13	0.46
s05a	2.03×10^{-4}	1.064	143.9	5.8	1.056	243.8	60.1	0.880	50.6	29.3	1.24	0.93
s05b	2.07×10^{-4}	1.056	133.8	18.4	1.030	263.3	65.0	0.914	38.2	16.3	1.17	0.65
s06	2.06×10^{-4}	1.059	236.6	31.5	1.037	216.2	56.8	0.903	60.8	9.4	1.19	0.73
s07	2.05×10^{-4}	1.066	227.8	63.1	1.043	359.2	18.7	0.891	95.9	18.8	1.22	0.75
s08	2.03×10^{-4}	1.071	12.4	35.7	1.069	223.0	50.1	0.860	113.7	15.3	1.29	0.98
s09	2.02×10^{-4}	1.066	318.1	58.2	1.063	211.4	10.1	0.871	115.7	29.8	1.26	0.97
s10	2.03×10^{-4}	1.073	333.9	79.9	1.068	215.4	4.9	0.859	124.6	8.8	1.29	0.96
s11	2.03×10^{-4}	1.071	10.5	33.8	1.069	237.8	45.4	0.860	118.9	25.3	1.29	0.98
s37.01a	2.08×10^{-4}	1.062	24.8	7.3	1.039	256.8	78.4	0.899	115.9	9.0	1.20	0.75
s37.02b	2.07×10^{-4}	1.044	30.5	3.3	1.026	281.1	80.3	0.930	121.0	9.2	1.13	0.70
s37.03a	2.08×10^{-4}	1.073	319.1	44.1	1.068	223.1	6.2	0.859	126.8	45.3	1.29	0.96
s37.04b	2.08×10^{-4}	1.069	11.5	25.7	1.057	261.8	35.1	0.874	129.2	43.9	1.25	0.89
s37.05a	2.08×10^{-4}	1.063	19.6	10.6	1.049	271.8	58.4	0.888	115.6	29.3	1.22	0.86
s37.06a	2.08×10^{-4}	1.061	25.2	13.2	1.000	269.0	62.0	0.939	120.7	24.1	1.13	0.03
s37.07d	2.08×10^{-4}	1.067	22.7	8.4	1.023	280.1	55.7	0.910	118.1	33.0	1.18	0.47
s37.08a	2.08×10^{-4}	1.070	102.8	49.5	1.060	8.2	3.9	0.869	274.9	40.2	1.27	0.91
s37.09a	2.08×10^{-4}	1.063	312.0	63.3	1.051	221.8	0.0	0.885	131.7	26.7	1.23	0.88
s37.10c	2.08×10^{-4}	1.067	111.4	46.2	1.060	6.8	13.6	0.873	264.9	40.7	1.26	0.93
s37.11b	2.08×10^{-4}	1.067	269.1	70.6	1.053	36.2	12.0	0.880	129.5	15.1	1.24	0.86
s37.12b	2.08×10^{-4}	1.065	22.0	15.6	1.061	274.0	47.9	0.874	124.6	37.9	1.25	0.96
s37.13a	2.08×10^{-4}	1.070	322.5	40.2	1.061	228.5	4.8	0.869	132.8	49.4	1.27	0.91
s46.08b	2.07×10^{-4}	1.042	306.2	4.1	1.035	44.1	62.2	0.923	214.1	27.4	1.15	0.88
s86.02a	2.08×10^{-4}	1.061	34.0	43.3	1.036	222.6	46.4	0.903	128.0	4.3	1.19	0.71
s86.03c	2.08×10^{-4}	1.067	16.2	47.6	1.048	245.0	31.0	0.886	138.1	25.7	1.23	0.80
s86.08a	2.08×10^{-4}	1.062	209.6	13.6	1.049	318.4	53.1	0.889	110.3	33.5	1.22	0.86

Seite Leer /
Blank leaf

REFERENCES

- Ballet, O. and Coey, J.M.D., 1982. Magnetic properties of sheet silicates; 2:1 layer minerals. *Phys. Chem. Minerals*, 8: 218-229.
- Ballet, O., Coey, J.M.D. and Burke, K.J., 1985. Magnetic properties of sheet Silicates; 2:1:1 layer minerals. *Phys. Chem. Minerals*, 12: 370-378.
- Banerjee, S.K., 1966. Exchange anisotropy in intergrown maghemite and hematite. *Geophys. J. R. Astr. Soc.*, 10: 449-450.
- Banerjee, S.K. and Moskowitz, B.M., 1985. Ferrimagnetic properties of magnetite. In: J.L. Kirschvink, D.S. Jones and B.F. Macfadden (Editors), *Magnetite Biomineralization and Magnetoreception in Organisms: A New Biomagnetism*. Plenum Press, New York, pp. 17-41.
- Banerjee, S.K. and O'Reilly, W., 1965. Exchange anisotropy in a single phase titanomagnetite. *Phys. Lett.*, 15: 25.
- Banerjee, S.K. and Stacey, F.D., 1967. The high-field torque-meter method of measuring magnetic anisotropy in rocks. In: D.W. Collinson, K.M. Creer and S.K. Runcorn (Editors), *Methods in Palaeomagnetism*. Elsevier, Amsterdam, New York, pp. 470-476.
- Bean, C.P. and Livingston, J.D., 1959. Superparamagnetism. *J. Appl. Phys.*, 30: 120S-129S.
- Beausoleil, N., Lavalley, Yelon, A., Ballet, O. and Coey, J.M.D., 1983. Magnetic properties of biotite micas. *J. Appl. Phys.*, 54(2): 906-915.
- Bergmüller, F., Bärlocher, C., Geyer, B., Grieder, M., Heller, F. and Zweifel, P., 1994. A torque magnetometer for measurements of the high-field anisotropy of rocks and crystals. *Meas. Sci. Technol.*, 5: 1466-1470.

- Bhathal, R.S., 1971. Magnetic anisotropy in rocks. *Earth-Sci. Rev.*, 7: 227-253.
- Bhathal, R.S. and Stacey, F.D., 1969. Field-induced anisotropy of magnetic susceptibility in rocks. *Pure Appl. Geophys.*, 76: 123-129.
- Borradaile, G., Mothersill, J., Tarling, D. and Alford, C., 1985/86. Sources of magnetic susceptibility in a slate. *Earth and Planetary Science Letters*, 76: 336-340.
- Borradaile, G.J., 1988. Magnetic susceptibility, petrofabrics and strain. *Tectonophysics*, 156: 1-20.
- Borradaile, G.J. and Henry, B., 1997. Tectonic applications of magnetic susceptibility and its anisotropy. *Earth-Sci. Rev.*, 42: 49-93.
- Borradaile, G.J., Keeler, W., Alford, C. and Sarvas, P., 1987. Anisotropy of magnetic susceptibility of some metamorphic minerals. *Phys. Earth Planet. Inter.*, 48: 161-166.
- Borradaile, G.J. and Werner, T., 1994. Magnetic anisotropy of some phyllosilicates. *Tectonophysics*, 235: 223-248.
- Bottoni, G., Candolfo, D., Cecchetti, A. and Masoli, F., 1999. Analysis of the magnetization switching using the rotational hysteresis integral. *J. Magn. Magn. Mater.*, 193(1-3): 329-31.
- Brindley, G.W. and Brown, G. (Editors), 1980. Crystal structures of clay minerals and their X-ray identification. Mineralogical Society, Monograph 5, London, 495 pp.
- Bunge, H.J., 1982. Texture analysis in Material Science: mathematical methods. Butterworths, London, 593 pp.
- Butler, R., 1992. Paleomagnetism. Blackwell Scientific, Cambridge, 319 pp.

- Casey, M., 1981. Numerical analysis of X-ray texture data: an implementation in FORTRAN allowing triclinic or axial specimen symmetry and most crystal symmetries. *Tectonophysics*, 78: 51-64.
- Cheaney, R.F., 1983. *Statistical methods in geology*. George Allen & Unwin, London, 169 pp.
- Chikazumi, S. and Charap, S.H., 1964. *Physics of Magnetism*. John Wiley & Sons, New York, 554 pp.
- Coey, J.M.D., Ballet, O., Moukarika, A. and Soubeyroux, J.L., 1981. Magnetic properties of sheet silicates; 1:1 layer minerals. *Phys. Chem. Minerals*, 7: 141-148.
- Collinson, D.W., Creer, K.M. and Runcorn, S.K. (Editors), 1967. *Methods in Palaeomagnetism*. Elsevier, Amsterdam, New York, 609 pp.
- Cowan, B.K. and O'Reilly, W., 1972. The effect of heat treatment on magnetic minerals in red sandstones, studied using the technique of rotational hysteresis. *Geophys. J. R. Astr. Soc.*, 29: 263-274.
- Day, R., O'Reilly, W. and Banerjee, S.K., 1970. Rotational hysteresis study of oxidized basalts. *J. Geophys. Res.*, 75: 375-386.
- Deer, W.A., Howie, R.A. and Zussman, J., 1975. *An Introduction to the Rock Forming Minerals*. Longman, London.
- Dekkers, M.J., 1988. Magnetic properties of natural pyrrhotite Part I: Behaviour of initial susceptibility and saturation-magnetization-related rock-magnetic parameters in a grain-size dependent framework. *Phys. Earth Planet. Inter.*, 52: 376-393.
- Dekkers, M.J., 1988. Some rock magnetic parameters for natural goethite, pyrrhotite, and fine-grained hematite. Ph. D. Dissertation Thesis, University of Utrecht.

- Dunlop, D.J., 1971. Magnetic properties of fine-particle hematite. *Ann. Géophys.*, 27: 269–293.
- Dunlop, D.J. and Özdemir, Ö., 1997. *Rock Magnetism*. Cambridge Univ. Press, Cambridge, 573 pp.
- Ellwood, B.B., 1978. Measurement of anisotropy of magnetic susceptibility: a comparison of the precision of torque and spinner magnetometer systems. *Journal of Physics E: Sci. Inst.*, 11: 71–75.
- Ellwood, B.B., 1978. Measurement of anisotropy of magnetic susceptibility: a comparison of the precision of torque and spinner magnetometer systems for basaltic specimens. *Journal of Physics E: Sci. Instr.*, 11: 71–75.
- Fletcher, E.J., de Sa, A., O'Reilly, W. and Banerjee, S.K., 1969. A digital vacuum torque magnetometer for the temperature range 300–1000 K. *Journal of Physics E: Sci. Inst.*, 2(ser. 2): 311–314.
- Fuller, M., 1963. Magnetic anisotropy and paleomagnetism. *J. Geophys. Res.*, 68: 293–309.
- Fuller, M.D., 1960. Anisotropy of susceptibility and the natural remanent magnetization of some Welsh slates. *Nature*, 186: 791–792.
- Graham, J.W., 1954. Magnetic susceptibility anisotropy, an unexploited petrofabric element. *Bulletin of the Geological Society of America*, 65: 1257–1258.
- Graham, J.W., 1966. Significance of magnetic anisotropy in Appalachian sedimentary rocks. In: J.S. Steinhardt and T.J. Smith (Editors), *The Earth Beneath the Continents*. American Geophysical Union, Geophysical Monograph Series, Washington, pp. 627–648.
- Hargraves, R.B. and Fischer, A.G., 1959. Remanent magnetism in Jurassic red limestones and radiolarites from the Alps. *Geophys. J. R. Astr. Soc.*, 2: 34–41.

- Henry, B. and Daly, L., 1983. From qualitative to quantitative magnetic anisotropy analysis: the prospect of finite strain calibration. *Tectonophysics*, 98: 327–336.
- Hirt, A.M., Evans, K.F. and Engelder, T., 1995. Correlation between magnetic anisotropy and fabric for Devonian shales on the Appalachian Plateau. *Tectonophysics*, 247: 121-132.
- Hirt, A.M., Julivert, M. and Soldevila, J., 2000. Magnetic fabric and deformation in the Navia-Alto Sil slate belt, Northwestern Spain. *Tectonophysics*, 320: 1-16.
- Hirt, A.M., Lowrie, W., Clendenen, W.S. and Kligfield, R., 1988. The correlation of magnetic anisotropy with strain in the Chelmsford Formation of the Sudbury Basin, Ontario. *Tectonophysics*, 145: 177-189.
- Hood, W.C. and Custer, R.L.P., 1967. Mass magnetic susceptibilities of some trioctahedral micas. *Am. Mineral.*, 52: 1643-1648.
- Hounslow, M.W., 1985. Magnetic fabric arising from paramagnetic phyllosilicate minerals in mudrocks. *J. Geol. Soc. London*, 142: 995–1006.
- Housen, B.A., Richter, C. and van der Pluijm, B.A., 1993. Composite magnetic anisotropy fabrics: experiments, numerical models, and implications for the quantification of rock fabrics. *Tectonophysics*, 220: 1–12.
- Housen, B.A. and van der Pluijm, B.A., 1990. Chlorite control of correlations between strain and anisotropy of magnetic susceptibility. *Phys. Earth Planet. Inter.*, 61: 315–323.
- Hrouda, F., 1979. The strain interpretation of magnetic anisotropy in rocks of the Nízky Jeseník Mountains (Czechoslovakia). *Sbor. Geol. Ved.*, 16: 27-62.
- Hrouda, F., 1982. Magnetic anisotropy of rocks and its application in geology and geophysics. *Geophys. Surv.*, 5: 37–82.

- Hrouda, F., 1986. The effect of quartz on the magnetic anisotropy of quartzite. *Stud. Geophys. Geod.*, 30(1): 39-45.
- Hrouda, F. and Jelinek, V., 1990. Resolution of ferrimagnetic and paramagnetic anisotropies in rocks, using combined low-field and high-field measurements. *Geophys. J. Inter.*, 103: 75-84.
- Hrouda, F., Pros, Z. and Wohlgemuth, J., 1993. Development of magnetic and elastic anisotropies in slates during progressive deformation. *Phys. Earth Planet. Inter.*, 77: 251-265.
- Hrouda, F. and Schulmann, K., 1990. Conversion of the magnetic susceptibility tensor into the orientation tensor in some rocks. *Phys. Earth Planet. Inter.*, 63: 71-77.
- Ihmlé, P.F., Hirt, A.M., Lowrie, W. and Dietrich, D., 1989. Inverse magnetic fabric in deformed limestones of the Morcles nappe, Switzerland. *Geophys. Res. Lett.*, 16: 1383-1386.
- Jackson, M.J., Gruber, W., Marvin, J.A. and Banerjee, S.K., 1988. Partial anhysteretic remanence and its anisotropy: applications and grainsize dependence. *Geophys. Res. Lett.*, 15: 440-443.
- Jelinek, V., 1978. Statistical processing of magnetic susceptibility measured on groups of specimens. *Stud. Geophys. Geod.*, 22: 50-62.
- Jelinek, V., 1981. Characterization of the magnetic fabric of rocks. *Tectonophysics*, 79: T63-T67.
- Jelinek, V., 1985. The physical principles of measuring magnetic anisotropy with the torque magnetometer. *Travaux de L'institut Geophysique de l'academie Tchecoslovaque des sciences*, 608: 177-198.
- Jelinek, V., 1988. Potential energy density tensor and magnetic anisotropy problems. *Phys. Earth Planet. Int.*, 51(361-364).

- Jiles, D., 1991. *Introduction to Magnetism and Magnetic Materials*. Chapman and Hall, London.
- Johns, M.K., Jackson, M.J. and Hudleston, P.J., 1992. Compositional control of magnetic anisotropy in the Thomson formation, east-central Minnesota. *Tectonophysics*, 210: 45–58.
- Julivert, M. and Soldevila, J., 1998. Small-scale structures formed during progressive shortening and subsequent collapse in the Navia-Alto Sil slate belt. *J. Struct. Geol.*, 20: 447-458.
- Kligfield, R., Lowrie, W. and Pfiffner, O.A., 1982. Magnetic properties of deformed oolitic limestones from the Swiss Alps: the correlation of magnetic anisotropy and strain. *Eclogae geologicae Helvetiae*, 75: 127-157.
- Kligfield, R., Owens, W.H. and Lowrie, W., 1981. Magnetic susceptibility anisotropy, strain, and progressive deformation in Permian sediments from the Maritime Alps (France). *Earth and Planetary Science Letters*, 55: 181–189.
- Lagroix, F. and Borradaile, G., 2000. Magnetic fabric interpretation complicated by inclusions in mafic silicates. *Tectonophysics*, 325: 207-225.
- Lalonde, A.E., Rancourt, D.G. and Ping, J.Y., 1998. Accuracy of ferric/ferrous determinations in micas: A comparison of Mössbauer spectroscopy and the Pratt and Wilson wet-chemical methods. *Hyperfine Interact.*, 117: 175-204.
- Lampert, S.A., 1996. *Paläomagnetische und gesteinsmagnetische Beiträge zur Lösung von stratigraphischen und tektonischen Problemen in den abruzzischen Apenninen und in SW-Sardinien*. Ph.D. Thesis, ETH-Zürich, 149 pp.
- Lowrie, W., 1989. Magnetic analysis of rock fabric. In: D.E. James (Editor), *The Encyclopaedia of Solid Earth Geophysics*. Van Nostrand Reinhold, New York, pp. 698-706.

- Lowrie, W., 1990. Identification of ferromagnetic minerals in a rock by coercivity and unblocking temperature properties. *Geophys. Res. Lett.*, 17: 159–162.
- Lowrie, W., 1997. *Fundamentals of Geophysics*. Cambridge Univ. Press, Cambridge.
- Lüneburg, C., 1995. Cleavage development and mineral anisotropies in siliciclastic sediments of SW Sardinia. Ph.D. Thesis, ETH-Zürich, 168 pp.
- Lüneburg, C.M., Lampert, S.A., Lebit, H.K., Hirt, A.M., Casey, M. and Lowrie, W., 1999. Magnetic anisotropy, rock fabrics and finite strain in deformed sediments of SW Sardinia (Italy). *Tectonophysics*, 307: 51-74.
- Martinez, J.F. and Rolet, J., 1988. Late Paleozoic metamorphism in the northwestern Iberian Peninsula Brittany and related areas in SW Europe. In: A.L. Harris and D.J. Fettes (Editors), *The Caledonian-Appalachian Orogen*. Geol. Soc. London, Spec. Publi., pp. 611-620.
- Martín-Hernández, F. and Hirt, A.M., 2001. Separation of ferrimagnetic and paramagnetic anisotropies using a high-field torsion magnetometer. *Tectonophysics*, 337: 209-221.
- Matte, P., 1986. Tectonics and plate tectonics model for the Variscan belt of Europe. *Tectonophysics*, 126: 329-374.
- McCabe, C., Jackson, M. and Ellwood, B.B., 1985. Magnetic anisotropy in the Trenton limestone: results of a new technique, anisotropy of anhysteretic susceptibility. *Geophys. Res. Lett.*, 12: 333-336.
- McCabe, C., Jackson, M.J. and Ellwood, B.B., 1985. Magnetic anisotropy in the Trenton limestone: results of a new technique, anisotropy of anhysteretic susceptibility. *Geophys. Res. Lett.*, 12: 333–336.
- Meiklejohn, W.H., 1962. Exchange Anisotropy (a review). *J. Appl. Phys.*, 33(3): 1328-1335.

- Murad, E., 1988. Properties and behavior of iron oxides as determined by Mössbauer spectroscopy. In: J.W. Stucki, B.A. Goodman and U. Schwertmann (Editors), *Iron in Soils and Clay Minerals*. Reidel Publishing, Dordrecht, pp. 309–350.
- Muxworthy, A.R., 1999. Low-temperature susceptibility and hysteresis of magnetite. *Earth and Planetary Science Letters*, 169(1-2): 51-8.
- Nagata, T., 1961. *Rock Magnetism*. Maruzen, Tokyo, 350 pp.
- Nagata, T. and Uyeda, S., 1959. Exchange interaction as a cause of reverse thermoremanent magnetism. *Nature*, 184: 890.
- Néel, L., 1949. Théorie du traînage magnétique des ferromagnétiques en grains fins avec applications aux terres cuites. *Ann. Géophys.*, 5: 99–136.
- Nishio, H., Takahashi, T., Taguchi, H., Kamiya, S. and Matsunaga, T., 1997. Magnetic characterization of bacterial magnetic particles. *Journal de Physique IV*, 7(C1): 663-6.
- O'Reilly, W., 1984. *Rock and Mineral Magnetism*. Blackie, Glasgow, 220 pp.
- Osete, M.L., Martín-Hernández, F., Osete, C., Villalaín, J.J., Nuñez, J.I., Martín-Atienza, B. and García-Dueñas, V., 1998. Estudio Paleomagnético de las Peridotitas del complejo ultrabásico de Ronda, 1ª Asamblea Hispano-Portuguesa de Geodesia y Geofísica, Aguadulce (Almeria).
- Owens, W.H., 1974. Mathematical model studies on factors affecting the magnetic anisotropy of deformed rocks. *Tectonophysics*, 24: 115–131.
- Owens, W.H. and Bamford, D., 1976. Magnetic, seismic and other anisotropic properties of rock fabric. *Phil. Trans. R. Soc. London*, A283: 55-68.

- Owens, W.H. and Rutter, E.H., 1978. The development of magnetic susceptibility anisotropy through crystallographic preferred orientation in a calcite rock. *Phys. Earth Planet. Inter.*, 16: 215–222.
- Özdemir, Ö. and Banerjee, S.K., 1984. High temperature stability of maghemite (γ - Fe_2O_3). *Geophys. Res. Lett.*, 11: 161–164.
- Ozdemir, O. and Dunlop, D.J., 1999. Low-temperature properties of a single crystal of magnetite oriented along principal magnetic axes. *Earth and Planetary Science Letters*, 165(2): 229-39.
- Parés, J.M., Van der Voo, R. and Stamatakos, J., 1996. Paleomagnetism of Permian and Triassic red beds of NW Spain and implications for the tectonic evolution of the Asturian-Cantabrian Arc. *Geophys. J. Int.*, 126: 893-901.
- Parma, J., 1988. An automated torque meter for rapid measurement of high field magnetic anisotropy of rocks. *Phys. Earth Planet. Inter.*, 51: 387-389.
- Parma, J., 1988. An automated torque meter for rapid measurement of high-field magnetic anisotropy of rocks. *Phys. Earth Planet. Inter.*, 51: 387–389.
- Parry, G.R., 1971. The magnetic anisotropy of some deformed rocks. Ph. D. Thesis, University of Birminham.
- Porath, H. and Raleigh, C.B., 1967. An origin of the triaxial basal-plane anisotropy in hematite crystals. *J. Appl. Phys.*, 38: 2401-2402.
- Ramsay, J.G. and Huber, M.I., 1983. The techniques of modern structural geology: Vol I: strain analysis. Academic Press, London, 307 pp.
- Ramsay, J.G. and Huber, M.I., 1987. The techniques of modern structural geology: Vol II: Folds and fractures. Academic Press, London, 392 pp.

- Rancourt, D.G., 1998. Mössbauer spectroscopy in clay science. *Hyperfine Interact.*, 117(3-38).
- Rees, A.I., 1961. The effect of water currents on the magnetic remanence and anisotropy of susceptibility of some sediments. *Geophys. J. R. Astr. Soc.*, 5: 235–251.
- Richter, C. and van der Pluijm, B.A., 1994. Separation of paramagnetic and ferrimagnetic susceptibilities using low temperature magnetic susceptibilities and comparison with high field methods. *Phys. Earth Planet. Int.*, 82: 111–121.
- Ries, A.C. and Schackleton, R.M., 1976. Patterns of strain variation in arcuate fold belts. *Phil. Trans. R. Soc. Lond. A.*, 283: 281–288.
- Robion, P., Averbuch, O. and Sintubin, M., 1999. Fabric development and metamorphic evolution of lower Palaeozoic slaty rocks from the Rocroi massif (French-Belgian Ardennes): new constraints from magnetic fabrics, phyllosilicate preferred orientation and illite crystallinity data. *Tectonophysics*, 309: 257–273.
- Rochette, P., 1987. Magnetic susceptibility of the rock matrix related to magnetic fabric studies. *J. Struct. Geol.*, 9: 1015–1020.
- Rochette, P. and Fillion, G., 1988. Identification of multicomponent anisotropies in rocks using various field and temperature values in a cryogenic magnetometer. *Phys. Earth Planet. Int.*, 51: 379–386.
- Rochette, P., Jackson, M. and Aubourg, C., 1992. Rock magnetism and the interpretation of anisotropy of magnetic susceptibility. *Reviews of Geophysics*, 30: 209–226.

- Sagnotti, L. and Winkler, A., 1999. Rock magnetism and palaeomagnetism of greigite-bearing mudstones in the Italian peninsula. *Earth and Planetary Science Letters*, 165(1): 67-80.
- Sano, M., Araki, S., Ohta, M., Noguchi, K., Morita, H. and Matsuzaki, M., 1998. Exchange coupling and GMR properties in ion beam sputtered hematite spin-valves. *IEEE Trans. Magn.*, 34(2, pt.1): 372-4.
- Sato, K., Yamada, M. and Hirone, T., 1964. Magnetocrystalline Anisotropy of Pyrrhotite. *J. Phys. Soc. Jpn.*, 19(9): 1592-1595.
- Siegesmund, S. and Becker, K.J., 2000. Emplacement of the Ardara pluton (Ireland): new constraints from magnetic fabrics, rock fabrics and age dating. *Int. J. Earth Sci.*, 89: 307-327.
- Siegesmund, S., Ullemeyer, K. and Dahms, M., 1995. Control of magnetic rock fabrics by mica preferred orientation: a quantitative approach. *J. Struct. Geol.*, 17(11): 1601-1613.
- Sintubin, M., 1994. Texture types in shales and slates. In: H.J. Bunge, S. Siegesmund, W. Skrotzki and K. Weber (Editors), *Textures of Geological Materials*. DGM Informationsgesellschaft Verlag, pp. 221-229.
- Squires, G.L., 1991. *Practical physics*. McGraw-Hill, London, 204 pp.
- Stacey, F.D., 1960. Magnetic anisotropy of igneous rock. *J. Geophys. Res.*, 65: 2429-2442.
- Stacey, F.D., 1963. The physical theory of rock magnetism. *Adv. Phys.*, 12: 45-133.
- Stephenson, A., 1994. Distribution anisotropy: two simple models for magnetic lineation and foliation. *Phys. Earth Planet. Inter.*, 82: 49-53.

- Sun, W., Hudleston, P.J. and Jackson, M.J., 1995. Magnetic and petrofabric studies in the multiply deformed Thomson formation, east-central Minnesota. *Tectonophysics*, 249: 109-124.
- Syono, Y., 1960. Magnetic susceptibility of some rock forming silicate minerals such as amphiboles, biotites, cordierites and garnets. *J. Geomagn. Geoelectr.*, 11: 85-93.
- Tarling, D.H. and Hrouda, F., 1993. *The Magnetic Anisotropy of Rocks*. Chapman & Hall, London, 217 pp.
- Ullemeyer, K., Braun, G., Kuhl, J.H., Olesen, N.Ø. and Siegesmund, S., 2000. Texture analysis of a muscovite-bearing quartzite: a comparison of some currently used techniques. *J. Struct. Geol.*, 22(1541-1557).
- Uyeda, S., Fuller, M.D., Belshé, J.C. and Girdler, R.W., 1963. Anisotropy of magnetic susceptibility of rocks and minerals. *J. Geophys. Res.*, 68: 279-291.
- Verwey, E.J., 1939. Electronic conduction of magnetite (Fe_3O_4) and its transition point at low temperature. *Nature*, 144: 327-328.
- Wenk, H.R. (Editor), 1985. *Preferred orientation in deformed metals and rocks: an introduction to modern texture analysis*. Academic Press, London, 610 pp.
- Zapletal, K., 1990. Low-field susceptibility anisotropy of some biotite crystals. *Phys. Earth Planet. Inter.*, 63: 85-97.

Seite Leer /
Blank leaf

CURRICULUM VITAE

Born in Madrid, Spain on June 15th 1974

- 1980-1988 Primary and Secondary School in Madrid, Spain
- 1988-1992 High School in Madrid, Spain
- 1992-1997 Study of Physics at the Universidad Complutense de Madrid, Spain
- 1997 Degree in Physics, specialization in Geophysics
- 1997-1998 Research in the Laboratory of Paleomagnetism, Universidad Complutense de Madrid, Spain
- 1998-2002 Assistant Research work at the Institute of Geophysics, Swiss Federal Institute of Technology of Zurich, Switzerland
- 2002 PhD thesis:
“Determination of fundamental magnetic anisotropy parameters in rock-forming minerals and their contributions to the magnetic fabric of rocks”
Referentes: Dr. A.M. Hirt, Prof. Dr. W. Lowrie, Dr. K. Kunze, Dr. M.C. Lüneburg